Orbital Dynamics Analysis and Scale Model Testing of Galloping Transmission Lines

Anand Gopala Krishnan

A Thesis

In

The Department

Of

Mechanical and Industrial Engineering

Presented in Partial Fulfillment of the Requirements

For the Degree of Master of Applied Science at

Concordia University

Montreal, Quebec

Canada

November 2006

Your file Votre référence
ISBN: 978-0-494-34595-5
Our file Notre référence
ISBN: 978-0-494-34595-5

ABSTRACT

Orbital Dynamics Analysis and Scale Model Testing of Galloping Transmission Lines

Anand Gopala Krishnan

The Overhead Electrical Transmission Lines, used for carrying high voltage electrical power, are held by huge steel towers with large spans. The cables of transmission lines are subjected to three different types of wind-induced vibrations, namely, galloping, aeolian and wake-induced vibrations. During winter, in some cold climates ice is deposited on the cable, making the cross section of the cable asymmetric. When wind blows across the ice accumulated cables, they start vibrating with large amplitudes and at low frequencies. In the present work, such galloping vibrations are analyzed. Neglecting the flexural rigidity and axial rigidity of the wire, two-dimensional equations of motion of the wire are formulated. The effect of torsion of cable is neglected. Fourth-order Runge - Kutta method has been employed to solve the governing equations and to obtain the orbital motions of the transmission line cable. The analytical model includes parameters such as ice inclination angle, angle of incidence of wind on the cable, sag length, angle subtended by the relative wind velocity to horizontal and aerodynamic force coefficients. The effects of these parameters on the orbital motions of the cable are investigated.

Validation of analytical studies is carried out by tests on scale models of the actual cable. The models are analyzed and the eigen values and eigen vectors are found out. Experimental investigation is carried on both the actual cable and the scaled model in the wind tunnel and orbital motions are measured. The test results are compared with the numerical simulations and discussed. The galloping motions were essentially orbital in nature. The test results validated the analytical investigations on the galloping phenomena.

Dedicated to my parents

ACKNOWLEDGEMENTS

I am sincerely thankful to my supervisor Dr. Rama B. Bhat for his enthusiastic guidance and continuous support during the course of this work. His help, stimulating suggestions and encouragement have always helped me throughout in this research and in writing of this thesis.

I am grateful to many people in the department who have assisted me in the course of this work. Among them, Dr. C. Rajalingam, Part-Time Faculty, for his initial guidance of this thesis, Mr. Danny Juras and Mr. Brad Luckhart, technical support staff, for their helpful assistance during the experimental set-up and testing of the cables in the wind tunnel.

The help and useful discussions during the course of this work are gratefully acknowledged from my student colleagues and friends. Some of them include Mr. Rakesh Kalyanaraman, Mr. Vaibhav Rawat, Mr. Sagar Kadam and Mr. Shankar Varma.

Finally, I thank my parents, Mr. A. S. Gopalakrishnan and Mrs. Hema Gopalakrishnan and my brother Raman for their untiring patience and continuous moral support throughout the research period, reminding me of my priorities and keeping things in perspective.

TABLE OF CONTENTS

CHAPTER 2: MODELING OF TRANSMISSION LINES

CHAPTER 3: SIMULATION RESULTS

LIST OF FIGURES

LIST OF TABLES

ABBREVATIONS

ACSR	Aluminium Conductor Steel Reinforced	-

LIST OF SYMBOLS

Notation	Description	Units
A_i	Cross sectional area of the ice	m^2
A_m	Cross sectional area of the wire	m^2
c	Wave velocity	m/s
C.G.	Centre of gravity of the rod	-
C_D	Co-efficient of drag force	-
C_L	Co-efficient of lift force	-
C_M	Co-efficient of moment force	-
D_i	Diameter of the ice section	m
D_m	Diameter of the cable	m
E	Young's modulus of the cable	N/m^2
F	Net aerodynamic force	N
F_D	Drag force	N
F_L	Lift force	N
f_p, f_m	Functions of prototype and model	-
F_X, F_Y	X and Y direction component of aerodynamic force	N

g	Acceleration due to gravity	m/s^2
G	Spatial Co-ordinate	-
h(t)	Horizontal tension component	N
I	Moment of inertia of the rod	$kg-m^4$
k_1 k_2, k_3, k_4	Stiffness of the springs in vertical and horizontal directions	N
K_1, K_2, K_3, K_4	Equivalent stiffness of the springs	N
l	Length of the cable	M
L_e	Extended length of the cable	m
M	Mass of the rod	kg
n	Number of modes	-
S	Curvilinear Co-ordinate	-
T	Tension in the cable	N
t	Time	s
U	Velocity of the wind	m/s
U_{OX}, U_{OY}	Horizontal and vertical components of wind velocity	m/s
U_r	Resultant velocity of the wind	m/s
W	Time Co-ordinate	-
x, x_1, x_2	Displacement in X direction	m

$\dot{x}, \dot{y}$	Velocity of the conductor in X and Y directions	m / sec
y, y_1, y_2	Displacement in Y direction	m
α	Angle of inclination of the lift and drag forces with the axis	deg
β	Angle of inclination of the wind with horizontal	deg
δ	Angle of inclination of the model with horizontal in Y - direction	deg
θ	Angle of attack	deg
λ	Irvine independent parameter	-
π	pi number	-
ρ_a	Density of the air	kg / m^3
ρ_i	Density of the ice	kg / m^3
ρ_m	Density of the wire material	kg / m^3
φ	Angle of inclination of the tension force with the horizontal	deg
ω	Frequency	rad/s
ω_{NX}, ω_{NY}	Natural frequencies in X and Y directions	rad/s
Φ	Angle of inclination of the model with horizontal in X - direction	Deg
Δ	Scale factor	-

CHAPTER 1

INTRODUCTION

1.1 General

Cables find a wide range of applications in various engineering structures. Cables are very efficient structural elements and are widely used in suspension bridges, cable-stayed bridges, guy wires, transmission lines and other flexible structures. These cables have very low inherent damping characteristics and hence are prone to vibrations. The most interesting property of the cables is their ability to withstand large axial tension.

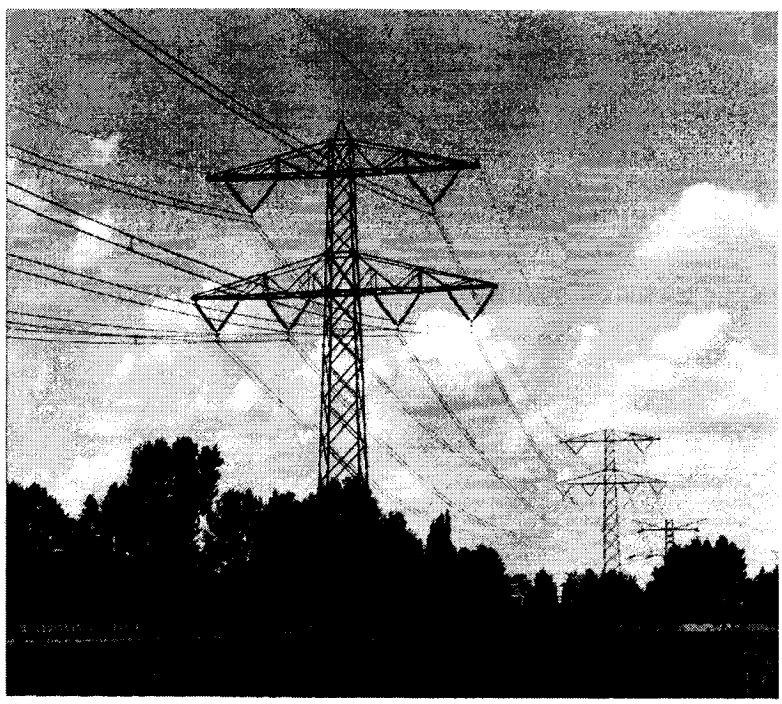

Fig 1.1: Transmission lines [1]

The cables used in Overhead Electrical Transmission lines are several kilometers long and are supported by huge steel structures or towers in rows with large spans. These cables are used to transfer the high voltage electrical power from one place to another. The cables are connected to the towers by movable strings or isolators which causes coupling of dynamical motions between the neighboring spans. The transmission line is highly flexible and is continuously exposed to wind forces.

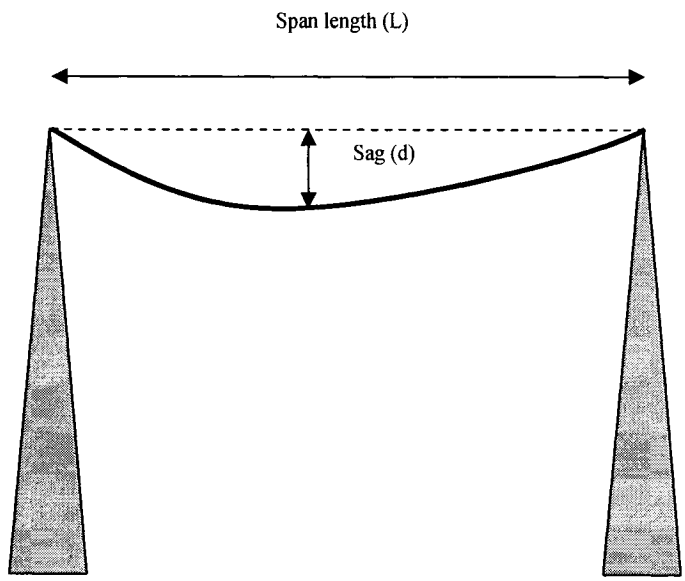

Fig 1.2: Schematic sketch of transmission line cable suspended between two towers

1.2 Types of wind induced vibrations

Among all the forces that cause motion of transmission line cable, wind along with rain and earthquake plays a major role. When the cables are exposed to wind, they are subjected to aerodynamic forces, namely, the lift and the drag. The force which acts along the direction of the wind is known as drag and the force which is perpendicular to the direction of wind flow is lift [2]. The lift and drag depend on the velocity of the wind. For different velocities of the wind, the lift and drag vary and hence cause different types of cable motions. The cable motion is generally classified into three types [3]:

a) Galloping

b) Aeolian vibrations

c) Wake induced vibrations

1.2.1 Galloping

Galloping of transmission lines is a low frequency, large amplitude, wind-induced vibration of both single and bundle overhead transmission lines, with a single or a few standing waves per span [3]. It is common in colder climates with hovering sub zero temperature and is never observed in warm climates. Ice formation around the conductors facilitates such galloping motions [4]. When moderately strong and steady cross winds blow over conductor with asymmetric cross

sections because of ice accumulation, galloping vibrations occur. Frequencies depend on the type of line construction and the oscillation modes excited. When galloping occurs, the strings and towers are subjected to high dynamic stress is leading to mechanical damage, such as loosening and ejection of tower bolts, wear on landing bolts, ovalling of bolt holes and distortion of tower swivels and associated hardware.

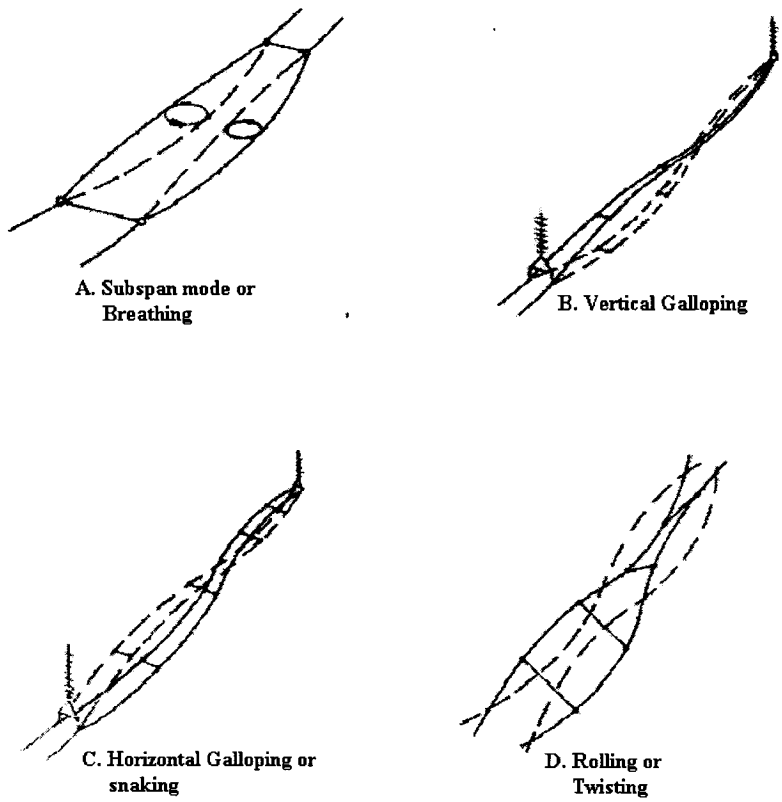

Fig. 1.3: (B-C) Galloping, (A-D) Wake induced vibrations [5]

1.2.2 Aeolian vibrations

Aeolian vibrations are high frequency and low amplitude vibrations caused by wind at low velocities. Observation shows that these vibrations occur within a range of velocities from 1m/sec to 7m/sec [3]. The basic cause of these types of vibrations is regular shedding of vortices from the conductor when the wind blows at right angle to the line. Aeolian vibrations are caused by alternating wind forces which arise from a pressure difference associated with formation of vortices behind the conductor [6]. The most common damage resulting from aeolian vibrations is the fatigue of line components such as armor rods, dampers, insulators etc.

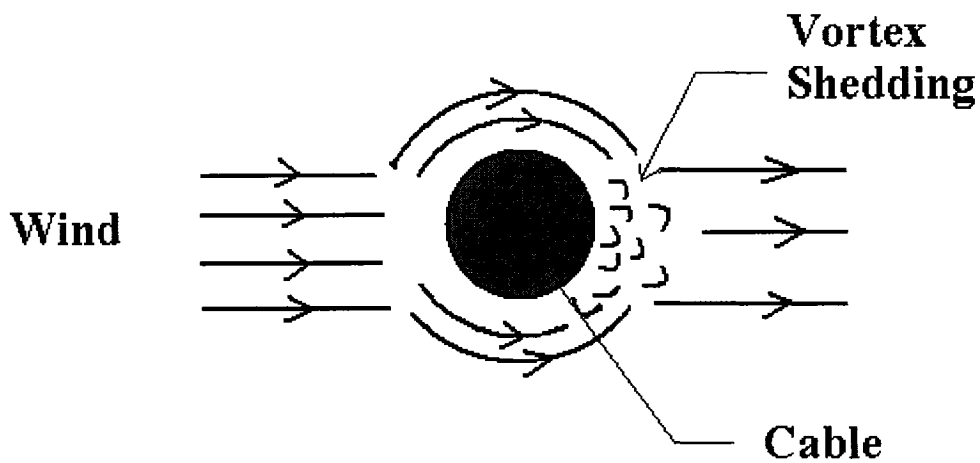

Fig. 1.4: Aeolian vibrations

1.2.3 Wake induced vibrations

These vibrations are more common in bundled conductors and encompass several types of motions in the conductor bundles. The motion is most often observed when the conductor is dry and bare but however it may occur with an iced conductor or when there is rain [3, 7]. These vibrations occur when the conductor is exposed to moderate to strong cross winds and arises from the shielding effect of the windward sub conductor to the leeward sub conductor [7]. The wake proceeding downwind from a stationary windward sub conductor can impose variable sets of forces on the leeward sub conductor. Depending on the magnitude and phase relationship of these forces, the motion of leeward sub conductor can be suppressed or they may cause it to move in an elliptical or irregular orbit. This movement of leeward sub conductor is transferred to the wind ward sub conductor through conductor spacers and other hardware devices [7]. Depending upon the phase and magnitude of windward sub conductor, the motion gets further complicated.

Common damages caused by these types of vibrations are fatigue of spacers or other accessories, failure or crushing of the conductor strands due to clashing, rapid wear in suspension hardware etc.

1.3 Ice accretion on transmission lines

The ice accretion or icing is the process of ice growth on a surface exposed to the atmosphere. The rate of growth of ice depends on the atmospheric moisture content, or the presence of icing particles, together with the airflow and thermal conditions local to the surface [8]. Moisture or the icing particles may exist as super cooled water droplets, such as in freezing fog and freezing rain, or as ice crystals agglomerated in the form of snowflakes. Icing particles carried by the wind may adhere to the conductor and ice grows out into the wind. This causes an eccentric ice load on the windward side of a conductor and causes the conductor to rotate during the accretion process; rotation of the conductor depends on the conductor torsional stiffness and on the aerodynamic torque exerted by the wind [8].

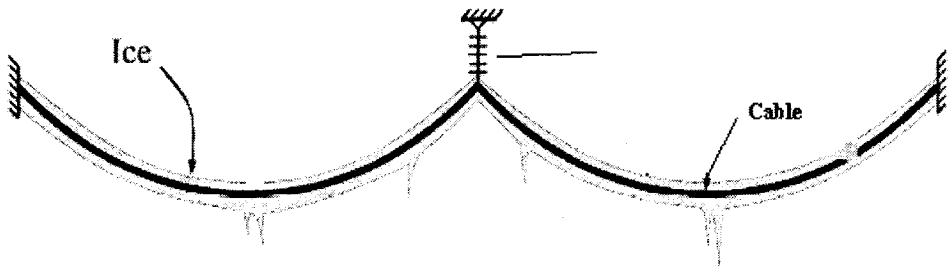

Fig 1.5: Ice accreted transmission line cable [9]

There are basically four types of deposits that may accumulate on a surface. They are [8, Appendix I]:

a. Rime

b. Glaze

c. Frost

d. Wet Snow

Ice accretion due to freezing fog, freezing rain or wet snow produces two types of problems:

- A wind induced instability known as galloping, associated with aerodynamically unstable ice profiles, typically few centimeters in thickness.
- Extreme ice and wind-on-ice loads on conductors and towers.

1.4 Survey of work done

Transmission lines in colder and windy regions are subjected to aerodynamic forces and are prone to vibrations. Many studies have been carried out on the phenomenon and control of such vibrations of transmission line cables. Survey was done on galloping, aeolian, ice-accretions on transmission lines and mitigation of these vibrations.

1.4.1 Galloping vibrations

J. P. Den Hartog [10] had first modeled the galloping phenomenon in transmission lines. He presented the mathematical description of galloping mechanism which is essentially similar to the classical aerodynamic instability. He considered only the aerodynamic properties of the ice profile into account. He proposed that the sustained vibrations happen only when the negative slope of the lift coefficient versus the wind's relative angle of attack exceeds the drag coefficient. He had excluded the mechanical properties of the system and the conductor torsion.

J. Wang and J. L. Lilien [11] presented a full multi span three degree of freedom iced transmission line model. They proposed that the model was applicable for describing the galloping phenomenon of both single and bundle lines, for performing static and dynamic analysis and predicting the galloping behavior of iced transmission lines, as well as for performing checks against field experience. The comprehensive mathematical model forms a foundation for performing structural analysis for investigations of anti-galloping devices. They proposed that the anti-galloping devices which combine detuning and torsion damping will be able to solve the flutter galloping problem. The study also included some original recommendations for design which could alleviate galloping and changes galloping consequences at the design stage by the appropriate design changes of suspension assembly.

T. Ohkuma, J. Kagami, H. Nakauchi, T. Kikuchi, K. Takeda, and H. Marukawa [12, 13] studied the factors that cause transmission line galloping and determined response evaluation indices of galloping in turbulent flows. This was done using three dimensional analytical methods considering large deformation. The analysis was based on four-bundle transmission lines. They proposed that the occurrence of galloping in the smooth flow is limited by the combination of the parameters such as the initial angle of wind attack, the initial icing angle and the wind speed. The galloping takes place mainly in one or two of the lowest in-plane, out-of-plane and torsional modes in free vibration subject to dead load as well as static wind force. However, the galloping always occurs with torsional vibrations. The predominant frequency components of galloping in turbulent flows are amplified and controlled by the turbulence intensity. Vibration frequency components unrelated to galloping increase linearly with rise in turbulence intensity.

S. W. Rienstra [1] studied the weakly nonlinear, freely vibrating motion of a system of coupled spans of suspended overhead transmission lines. He showed that the natural vibration is the gravity mode, which is free from tension in the first harmonic. Particular attention was given to an intermodal resonance, which was useful for galloping control.

The behaviour of transmission lines cables in severe boundary layer winds was studied by A. M. Loredo-Souza and A. G. Davenport [14-15]. They examined the effect of scale of turbulence on the response of a line-like structure (cable model) through wind tunnel tests and compared the wind tunnel tests with

theoretical predictions made through the statistical method using influence lines. They developed a new modeling approach to conductor systems using a distorted horizontal length scale (span wise) to accommodate them in wind tunnel. The experimental results showed the importance of turbulence in the dynamic response and the role of aerodynamic damping in the dynamic behavior of the cables.

O. Chabart and J. L. Lilien [16] performed testing on electrical lines in a wind tunnel. According to them, the presence of ice accretion on transmission lines has the effect of modifying the conductor's cross-sectional shape such that it becomes aerodynamically and/or aeroelastically unstable. A typical eccentric ice shape was reproduced on a classical stranded overhead line conductor and quasi-static aerodynamic coefficients were measured. The same sample was then suspended with springs in the wind tunnel in order to obtain a system as close as possible to an overhead line and galloping motions for appropriate angles of attack. The authors proposed that these measurements can be used for numerical model validation and for efficiency evaluation of some anti-galloping devices.

M. A. Baenziger, W. D. James, B. Wouters and L. Li [17] presented a procedure for determining the forces on insulators and cross arms due to the large amplitude vibration of ice-loaded conductors. Two approaches were taken to determine dynamic forces acting on support structures during galloping. The analytical approach developed a simplified formulation for the increase in vertical and horizontal components of line tension as a function of transmission line system parameters. Experimental measurements in a wind tunnel using a flexible

line model were used to verify the analytical model and to investigate the aerodynamic factors contributing to galloping. The dynamic forces obtained from analytical models were compared with the measured values of an instrumented transmission during real ice storms.

L. A. Pipes [18] performed theoretical analysis on vibration of conductors provided with dampers and proposed some new methods of eliminating or reducing conductor vibrations. J. S. Caroll [19] conducted vibration tests on 5 different types of transmission line conductors in wind tunnel and presented the results. The frequencies and amplitudes of vibration for various wind velocities were measured, power required to vibrate the conductor in still air and amount of energy taken from wind by the vibrating conductor were reported.

E. A. Johnson, R. E. Christenson and B. F. Spencer Jr. [20] focused on mitigation of cable vibrations, in order to minimize damage during service. Transversely attached passive dampers were implemented to dampen the cable vibrations. However, it was shown that only minimal damping could be added if the damper attachment point is close to the end of the cable. For long cables, passive dampers may provide insufficient supplemental damping to eliminate vibration problems. The authors proposed that smart semi active damping can provide significantly superior results for a cable modeled as a taut string. The work considers the effect of cable sag, inclination and axial flexibility to the cable model. A new control-oriented model was developed for cables with sag. Passive, active and smart (semi active) dampers were incorporated into the model and

cable response was found to be reduced by semi active dampers for a wide range of cable sag and damper locations.

A. Jha [21] performed the dynamic testing of structures using the scale models. Using the similitude theory, he developed similar conditions or the scaling laws for dynamic testing of scaled structures. These laws provide relationship between the prototype and its small scale model and can be used in determining the response of the prototype by performing dynamic testing on inexpensive model completely. These scaled models have been extensively used in wind tunnel testing of large structures such as automobiles, buildings and aircrafts. Sometimes the scale models are difficult to be made and this leads to relaxations or distortions from exact simulation of the prototype. The study also elaborated the complete and partial similarities in his work.

H. M. Irvine [22] in his CABLE STRUCTURES had presented the static and dynamic analysis of cables used in overhead transmission lines and bridges. He developed mathematical model for different types of cables which helped in understanding their behaviour under various loads and also developed an expression for the cable sag which has been used in various works.

R. M. Corless and G. V. Parkinson [9, 23] proposed an improved solution of the semi-empirical model based on 'Hartlen-Curie' model [24] and quasi-steady model of Parkinson and Smith [25, 26]. They used the method of multiple scales [27] with appropriate asymptotic embedding and gave an explicit analytical solution for the equilibrium of the Hartlen-Curie model, calculated using

'Grobner bases' [24]. The solution exhibited phase jump when there was change in wind speeds.

B. W. Van Oudheusden [28] investigated the galloping oscillation with a single rotational degree of freedom for a prismatic beam with rectangular cross section. He proposed that for this particular geometric configuration, the effect of the unsteady dynamic forces can be taken as a combination of aerodynamic stiffness and damping terms, with the latter being the most relevant for the instability behaviour. A theoretical prediction of both these effects was made for this type of galloping behaviour, based on a quasi-steady aerodynamic approach. Comparison was made with experimental results obtained in wind tunnel and this revealed significant shortcoming of the quasi-steady approach in predicting damping effect, but for the stiffness effect, the agreement was much better.

F. S. Hover and M. S. Triantafyllou [29] proposed that lightly-damped cylinders in free vibrations 4.75 D behind stationary cylinders of same size are capable of large-sale galloping, helping fill-in a gap between similar tests at larger spacing ratios, and the case of dually compliant cylinders. The frequency lock-in begins at nearly the same free-stream reduced velocity as a single cylinder, while a large phase change in the lift force occurs at higher reduced velocities, which can be extrapolated from the single cylinder lock-in point. Force spectra indicate that shedding from the upstream cylinder is completely unaffected by motions of the trailing cylinder. Furthermore, the motion-coupled peaks suggested that only one lift force cycle and one or two drag force cycles occur per oscillation, the latter depending on the offset.

W. J. Kim and N. C. Perkins [30] investigated resonant responses of suspended elastic cables driven by a steady current. Phenomenological fluid forces models for alternate vortex-shedding were coupled with the nonlinear partial differential equations of cable motions. They also examined the decoupled cross-flow and in-line vortex-induced vibrations using linearized and nonlinear cable models. The basic characteristics of vortex-induced vibrations were predicted by the linearized cable model and the non-linear cable model captures the hysteresis which was observed in the experiments. The author proposed that the coupled cross-flow and in-line motions originated from two coupling mechanisms: structural nonlinearities and coupled lift/drag. Attention was focused on worst case resonant response where the natural frequencies for the cable modes in the cross-flow and in-line directions are in the same 1:2 ratio as the excitation frequencies associated with lift and drag. The inclusion of cable structural nonlinearities alone lead to coupled responses that differ qualitatively (i.e. in number and stability of periodic motions) when compared to those of the decoupled model. The coupled lift/drag produces non-planar motions of the cable cross-section that exhibit similar characteristics to those which were measured in spring supported cylinders.

A. Cigada, G. Diana, M. Falco, F. Fossati and A. Manenti [31] presented the state of art of the research on wind-induced vibrations of cylinders with circular section or multiple arrangements. They mainly investigated the problem of wake-induced vibrations of closely spaced cylinders and presented a mathematical model to simulate this phenomenon. Wind Tunnel tests were also

performed. P. Hagedorn, N. Mitra and T. Hadulla [32] studied the phenomenon of vortex-excited vibrations in bundled conductors and presented a mathematical model for them. A new modified energy-balance method along with singular perturbation method was used to determine the bending strains at critical points. This gives an estimate for the maximum strain levels in a conductor, which can be useful in the design of transmission lines and for the optimization of the corresponding damping devices.

Y. Eguchi, N, Kikuchi, K. Kawabata, T. Yukino and Y. Ishikubo [33] developed a new type of electric wire for overhead transmission lines to reduce the drag force under a typhoon condition. Using water experiment they studied the drag reduction mechanism, which allowed the time scale of the experiment to expand about 100 times larger than that of an actual phenomenon in air under Re number similitude. The aerodynamic characteristics regarding the mean drag coefficient were also extensively studied in wind tunnel experiments, including the effects of wind velocity, wind incident angle, surface roughness and turbulence intensity.

M. Roshan and G. McClure [34] simulated the dynamic effects of ice shedding on overhead transmission lines using a numerical model. Using nonlinear finite element analysis software (ADINA) he developed a model which was used to calculate the static and dynamic analysis of ice-shedding on a two-span line section. A total of 21 ice-shedding scenarios were studied with variables including: ice thickness, span length, difference in elevation between end and suspension points, number of spans per line section, presence of unequal spans

and partial ice-shedding on sub spans. The effects of each of these parameters were discussed.

J. L. V. Brito and J. D. Riera [35] proposed that the action of wind on the vibrating bodies causes modification in the flow conditions giving rise to aerodynamic forces which depends principally on the velocities and displacement of the body in action. These forces are responsible for producing dynamic instability of structures. The author had formulated the problem considering prismatic section under two-dimensional flow conditions using linearised equations in structural analysis. Three degrees of freedom of the body were taken into account considering rotation; up and down and fore and aft motions and a new method for obtaining appropriate coefficients experimentally for arbitrary prismatic sections were also discussed. This was employed to obtain the aerodynamic coefficients of H-shaped beam.

G. McClure and M. Lapointe [36, 37] summarized a macroscopic modeling approach to line dynamic analysis where emphasis was put on capturing the features of the propagation of shock loads such as those induced by the sudden failure of components or sudden ice-shedding effects on the conductors. The approach was illustrated with a case study of a line section having suffered two tower failures due to conductor breakages during an ice storm.

G. Diana, S. Bruni, F. Cheli, F. Fossati and A. Manenti [38, 39] and E.I. Baranov, A.A Zevin [40] came up with a dynamic design of transmission line structures. Their study concerned with safe and correct design of towers, damping devices, insulator suspension and tension sets. N. Kikuchi, Y. Matsuzaki, T.

Yukino and H. Ishida [41, 42] studied the aerodynamic characteristics of grooved round transmission wires in wind tunnel under the conditions of heavy rainfall and wind. They set up a watering grid upwind in the wind tunnel's test section, which simulated a number of rainfalls: 0, 2, 4, 8, 10, 16, 25 and 40 mm per 10 min. These rainfalls were rationalized, based on domestic weather observation data: 10 min cumulative amounts of rain and 10 min mean wind speeds of time frame.

N. Barbieri, O. Honorato de Souza Jr. and R. Barbieri [43 - 45] performed dynamic analysis of electrical transmission lines using finite element analysis. The results were compared with the experimental data obtained in an automated testing system for overhead line cables. Different sample lengths were used and the forced responses were obtained through an impulsive excitation. R. I. Harris and M. Kasperski [46, 47] discussed the specifications of the design wind loads based on wind tunnel experiments.

1.4.2 Aeolian vibrations

As mentioned earlier, aeolian vibrations are caused due to regular shedding of vortices from the conductor when the wind flows over them. The computation of the fluid forces on a structure is one of the important tasks in the design of the structure. It is also one of the most difficult tasks as it involves the complexity of the interaction of waves with the structure [48]. The problem of a cylindrical body oscillating in the fluid has received a great deal of attention. R. E. D Bishop and

A. Y. Hassan [49] were the first to investigate the effect of body oscillation on vortex shedding. Later G. H. Koopmann [50], O.M. Griffin [51], P. W. Bearman and I. G. Currie [52] and T. Sarpkaya [53] studied the problem of a cylinder oscillating laterally (cross-flow) in a free stream of wind. E. Guilmineau and P. Queutey [48] also investigated the vortex-shedding from an oscillating circular cylinder by numerical solutions of the two-dimensional unsteady Navier-Stokes equations. They used a physically consistent method for the reconstruction of velocity fluxes which arises from discrete equations for the mass and momentum balances.

A. Leblond and C. Hardy [54, 55] presented a probabilistic model for predicting Aeolian vibration response of single overhead transmission line conductors. They used two different approaches to assess safe design tensions. One was based on the conductor fatigue endurance limit and the other was on linear fatigue damage accumulation associated with each vibration cycle which leads to a certain predicted fatigue life of the conductor.

J. Vecchiarelli, I. G. Currie and D. G. Havard [56, 57] had derived a numerical scheme which was based on empirical models developed to represent the vortex-induced lift force from the wind as well as the forces of dissipation associated with the conductor self-damping and external damper. The scheme also predicted that in overhead transmission line cables with a Stockbridge damper attached near a conductor span end, a traveling wave continually propagates towards that span

end during steady-state aeolian conductor vibration. They also proposed that, with no dampers attached to a conductor, steady-state aeolian conductor vibration is essentially in the form of a standing wave.

M. Kraus and P. Hagedorn [58] estimated the wind power inputs in an actual transmission line from the measurements obtained by the field tests in a completely automated test station. When the data of wind power inputs were compared with the results of the wind tunnel data, it corroborated the method used for the calculation of aeolian vibrations in transmission lines.

S. Houari, M. Rahli and A. Massoum [6] studied the aeolian vibrations of transmission line conductors. They developed a mathematical model for the cable as well as forces acting on the cables. The model was based on a modal approach concerning the schematization of the cable. This method had the advantages relating to time domain and at the same time to reduce the computing times compared to finite elements models [59, 60].

G. Diana, F. Cheli, F. Fossati and A. Manenti [61] investigated the dynamic behaviour of the cable under vortex shedding excitation using an analytical approach under turbulence conditions. The conductor was schematized by finite element method. The time history of the velocity field was computed at any nodal point of the schematization and the vortex shedding effects were reproduced by means of equivalent non linear oscillators. Wind tunnel tests on the cables for

aeolian vibrations were performed and studied by D.U. Noiseux, S. Houle and R. Beauchemin [62] under turbulent conditions.

1.4.3 Ice accretion on transmission line cable

The study of ice and wet-snow accretion on transmission line structures exposed to the atmosphere is of great interest since wind load acting on the transmission lines may lead to excessive dynamic response that may result in failure of the structure. Considerable work has been done on the snow-ice accretion on cables. Y. Sakamoto [63] studied and presented the mechanism of snow accretion on wires. He reviewed the fundamentals of the meteorological conditions under which snow accretes on wires and heat balance of snow accretion on cables. Wind tunnel tests aimed at examining the dependence of various parameters on the characteristics of accreted snow on wires were introduced and limitations of such tests were also discussed. Attempts to establish snow-load design on power lines, with some results of observations under natural conditions were discussed.

L. Makkonen and M. M. Oleskiw [64] described techniques for simulating atmospheric rime icing [Appendix –I] in small scale. The method was useful in estimating ice loads on complex structures for which theoretical icing modeling was difficult. The technique proposed in this work can be used to detect the effect of changes in structural design due to ice loads. L. Makkonen [65] also discussed ice accretion on structures with an emphasis on estimating ice loads and solving operational icing problems. He presented basic principles of modeling of icing

caused by freezing precipitation, cloud droplets and wet snow, as well as simulation of icicle growth.

P. McComber and A. Paradis [66, 67] developed a new approach for the analysis of cable galloping phenomenon by including the effect of torsional vibration on lift force in a quasi-static analysis. It adds to the lift force generated by the change in angle of attack, created by the cable rotation. Lift forces measured for steady-state rotation of a two-dimensional cylinder were used to relate lift to rotational speeds in the galloping model. The torsional vibration instability conditions were satisfied even for thin ice accretions, for wide range of angles. Since a rotational motion once created is sufficient to generate lift forces independently of the eccentricity of the ice shape, the approach given in this paper showed that it is possible to simulate galloping for thin ice accretion with the assumption of the 'vortex lock-in effect'.

S. Krishnasamy and S. Kulendran [68, 69] proposed a comprehensive procedure to determine the appropriate combination of annual extreme wind and ice values for calculating 'wind-on-ice loads' on transmission line conductors. G. Poots [8, 70] investigated the phenomenon and physical aspects of ice and snow accretion on cable structures. He discussed theoretical icing models currently employed to describe accretion of ice and snow on structures.

1.4.4 Mitigation of cable vibrations

There exist many possibilities to protect overhead transmission line cables against fatigue due to wind induced vibrations. The most commonly used method is the addition of external damping devices to existing conductors. Among several other damper types, the Stockbridge damper has proved to be one of the most efficient devices.

The damper was invented by G. H. Stockbridge in 1924 [71]. Since then, the damper has undergone a series of modifications. A recent design has been developed as a result of extensive research work carried out in the late 1960s and 1970s [72-77]. A Stockbridge damper consists of two weights attached to the end of stranded cables, which are known as messenger wires [57]. The messenger wires usually consist of 7 strands of steel and are able to dissipate energy by the same mechanism that a conductor can, that is, through strand slippage and material damping. A Stockbridge damper is shown in the figure 1.5.

H. Verma [5] investigated the mitigation of cable vibration using STOCKBRIDGE damper [71-77]. His work was mainly aimed at modeling the statical hysteresis which has been done by means of 'MASING model' [78] using number of parallel spaced 'JENKIN elements' [79]. A 'JENKIN element' consists of one linear spring and one 'Coulomb' friction element [79] attached in parallel. The messenger cable is a continuous system and damping takes place throughout its length. This model was then incorporated in the STOCKBRIDGE damper to

obtain a series of nonlinear ordinary differential equations. He also used this damper model in actual single conductor transmission line and computed its vibrations in order to study the effectiveness of the damper. In order to obtain the transmission line vibrations, the whole span of transmission line together with Stockbridge damper had been considered. Energy balance principles were used to determine the vibration amplitudes.

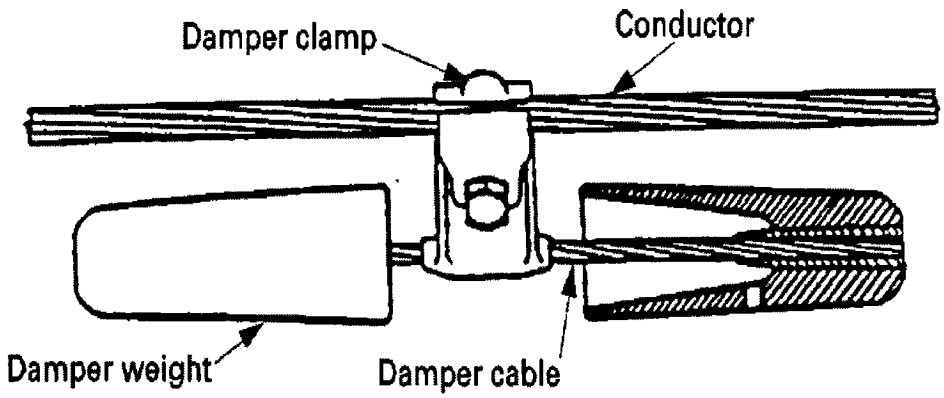

Fig 1.6: A Stockbridge-type damper with cross-sectional view of a damper weight [71]

M. Markiewicz [71] presented a method and a computational model for the evaluation of the optimum dynamic characteristics of Stockbridge damper to be mounted near the tension insulator assemblies. It also shows how the efficiency of a standard damper used in such spans may be improved by its proper location on a

cable. G. Diana, A. Cigada, M. Belloli and M. Vanali [80, 81] performed experiments on modified dynamometric Stockbridge damper clamped to a laboratory test span. The aim of the experiments was to get the force and the torque exerted between the cable and the damper on a span. This approach is useful in obtaining the mechanical impedance of the damper under real working conditions, with the possibility to separate the contribution of the torque and of the force out of the global losses, and these results were later also compared with those obtained on a shaker where only the vertical motion is imposed, with no rocking.

1.5 Objectives and scope of thesis

The survey of the work done showed that extensive study was done on single and bundled transmission lines, and analytical models were developed considering the transverse motions along vertical, horizontal directions and torsion of the cable. There is a mention of transmission line orbital motion based on experimental observations, however, analytical studies on the orbital dynamics of transmission lines are not found. Hence, the present work considers single conductor wire model and the orbital dynamics of a small segment of the cable under galloping condition. A single stranded BERSFORT type of cable between any two sub-spans is considered for analysis. Galloping occurs only when the cross section of the wire is irregular in shape. Hence an arbitrary ice shape based on O. Chabart's work [16] is chosen and equations of motion are derived for the cable. The coefficients of aerodynamic forces are taken from the experimental investigation

carried out by Chabart's work. The factors considered responsible for transmission line galloping are angle of attack of the wind on conductor, shape and type of ice accretion on cable, ice inclination angle and wind velocity.

Experimental investigations on actual and scaled model of the cable are carried out in a wind tunnel and orbital motions of the same are studied for different angles of attack, wind velocities and ice inclination angles.

1.6 Organization of thesis

In chapter 1, an introduction to wind induced vibrations and a brief description of overhead electric transmission line nomenclature is given. Different types of ice accretion on cables are also explained. A complete literature review is provided, which gives an insight into the research done for analyzing the factors responsible for galloping vibrations. It also provides the motivation and scope of the thesis undertaken.

In chapter 2, a basic two dimensional mathematical model of a small segment of transmission line cable is considered and the equations of motion for the transverse vibration of the segment are derived considering the effect of cable sag and aerodynamic forces on it.

In chapter 3, simulation results are presented and discussed. A parametric study of the orbital motions of the transmission line cables are carried out by solving the equations of motion and factors affecting the galloping vibrations are discussed.

Chapter 4 discusses the scale modeling technique and using the same the models to be tested in the wind tunnel are obtained. The principle of co-ordinate coupling is employed to perform model analysis on the cable models.

Chapter 5 discusses the experimental investigations on the transmission line model. This chapter also discusses the results obtained from the experiments on the transmission line model in a wind tunnel and a comparison of the results is done with those obtained in the chapter 3.

Chapter 6 presents conclusion of the work undertaken and recommendations for the future work.

CHAPTER 2

MODELLING OF TRANSMISSION LINES

2.1 Introduction to self-excited vibrations

Consider a mass-spring-damper system as shown in figure 2.1.a. When the system is given a small displacement in downward direction and released, it vibrates freely with constant amplitude if the damping is zero. With finite damping, the amplitudes are never constant but gradually decrease with time. These vibrations which occur in the absence of external excitations are known as free vibrations. Figure 2.1.b and 2.1.c show the graphical representation of undamped free vibrations and damped free vibrations, respectively.

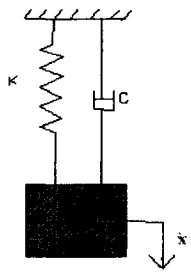

Fig 2.1.a: Mass-spring-damper system

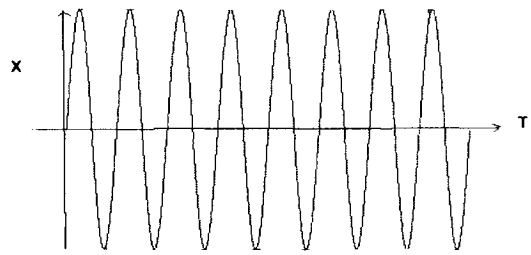

Fig 2.1.b: Undamped free vibrations (c = 0)

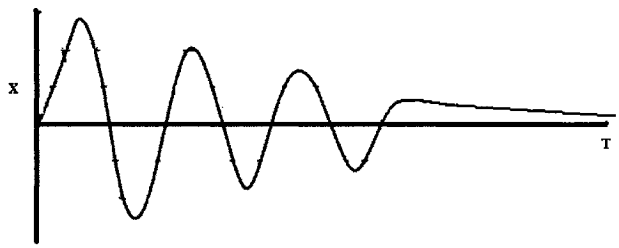

Fig 2.1.c: Free damped vibrations

A self-excited vibration may be seen as a free vibration with negative damping. Usually in free vibration, positive damping produces a force proportional to the velocity of vibration and is directed opposite to it. But in case of negative damping, the force is proportional to the velocity and acts in the same direction. Thus instead of diminishing the amplitudes of free vibration, they tend to increase it. Figure 2.2 shows a graphical representation of self excited Vibrations.

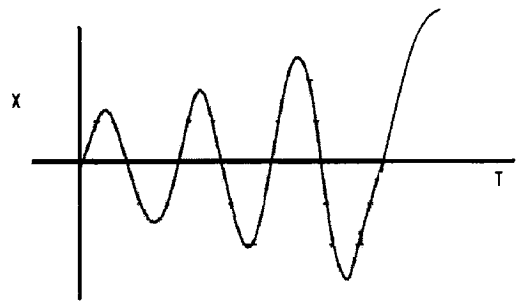

Fig 2.2: Self excited vibrations

The difference between a self-excited vibration and forced vibration is that in self excited vibration the alternating force that sustains the motion is created or controlled by the motion itself; when the motion stops, the alternating force disappears. In forced vibration the sustaining alternating force exists independent of the motion and persists even when the vibratory motion is stopped [4].

A transmission line vibration is a typical example of self-excited vibration. When wind blows over the conductor, the force generated by wind creates negative damping (also known as pseudo damping) which instead of diminishing the amplitude increases it.

2.2 Den Hartog's principle of galloping

When wind flows over a circular cross section as shown in Figure 2.3.a below, aerodynamic excitations are induced on it. These forces acting on the section can be resolved into two components. The force which acts in the direction of the wind is called the drag (F_D) while the one which acts perpendicular to the direction of the flow is lift (F_L) [2].

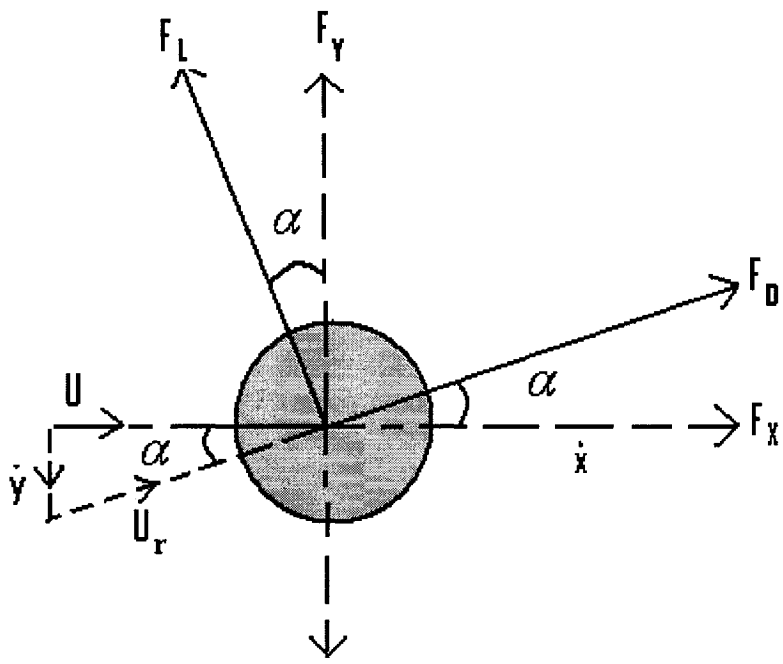

Fig. 2.3.a: Free body diagram of the cable under the action of wind

The Figure 2.3.b shows the relative velocity diagram wherein the relative velocity of wind with respect to the conductor can be found out.

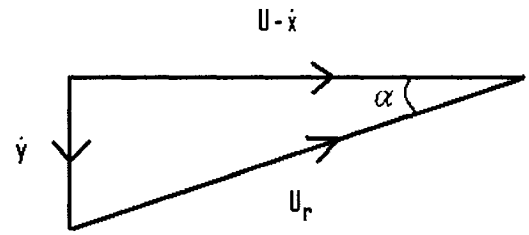

Fig 2.3.b: Relative velocity diagram

Den Hartog analyzed the galloping phenomenon in transmission line cable. He resolved the aerodynamic force acting on the ice accumulated conductor when wind flows over it into lift and drag forces. F_L, F_D is the lift and drag forces on the cable, U_r the relative wind velocity on the cable and $\dot{y}$ is the relative motion of the cable with respect to the wind.

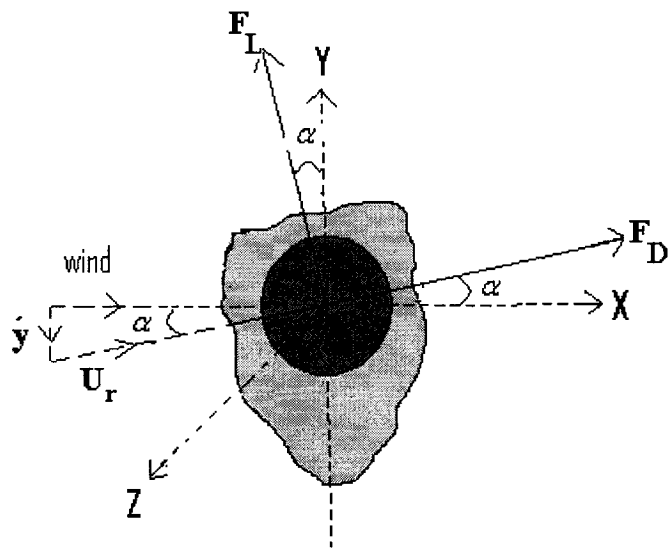

Fig 2.3.c: Cross section of the ice accreted cable

The total force in the vertical direction was expressed as:

$$F = L\cos\alpha + D\sin\alpha \qquad \text{- (2.1)}$$

Den Hartog studied the variation of this vertical force with the variation in α or in $\tan^{-1}\left(\frac{\dot{y}}{U}\right)$. He proposed that if F had a large value and $\frac{dF}{d\alpha}$ is zero it means that the part of the weight of the line would not be carried by the towers but by the wind directly. Any vibration or galloping of the line would not change the wind-carried weight so that the vibration would not be affected. If $\frac{dF}{d\alpha}$ was negative, then the upward wind force would increase for negative α and decrease for positive α. This is the case of encouraging alternating force. The criterion for dynamic stability was given as

$$\frac{dF}{d\alpha} < 0 \qquad \text{(Unstable)} \qquad \text{- (2.2)}$$

$$\frac{dF}{d\alpha} > 0 \qquad \text{(Stable)} \qquad \text{- (2.3)}$$

Alternatively the system is unstable when

$$\frac{dL}{d\alpha} + D < 0 \qquad \text{- (2.4)}$$

where $\sin\alpha \approx \alpha$ for small α. Thus according to him, a section is dynamically unstable if the negative slope of the lift curve is greater than the ordinate of the drag curve.

2.3 Introduction to continuous model

The mass-spring-damper system shown in the figure 2.1.a is a discrete system model wherein the equation of motion of the system can be found out easily by applying the Newton's laws of motion to the system. The overhead electric transmission line has stranded cables which run for several kilometers and are supported by huge steel towers placed at frequent intervals. The cables between any two towers are considered for analysis and are modeled as vibrating strings suspended between two supports. The present work is based on following assumptions:

- The wire is a flat sag cable and it vibrates initially with small velocities in X and Y planes, respectively.
- The profile of the sagging cable is parabolic and flexural rigidity is ignored.
- The moment force of cable about its own axis is neglected; hence the torsional vibration is excluded.
- All downward forces and motions are considered positive.

Factors such as cable sag, ice inclination angle, wind velocity and its inclination are considered for deriving the equations of motion.

2.4 Vibration of transmission line [Strings]

As mentioned earlier, the transmission lines are modeled as vibrating strings fixed at two ends. The figure 2.4 below shows a small segment of a string of density ρ_m per unit length, stretched under tension T. Assuming the lateral deflection y to be small, the change in tension with deflection is negligible and can be ignored.

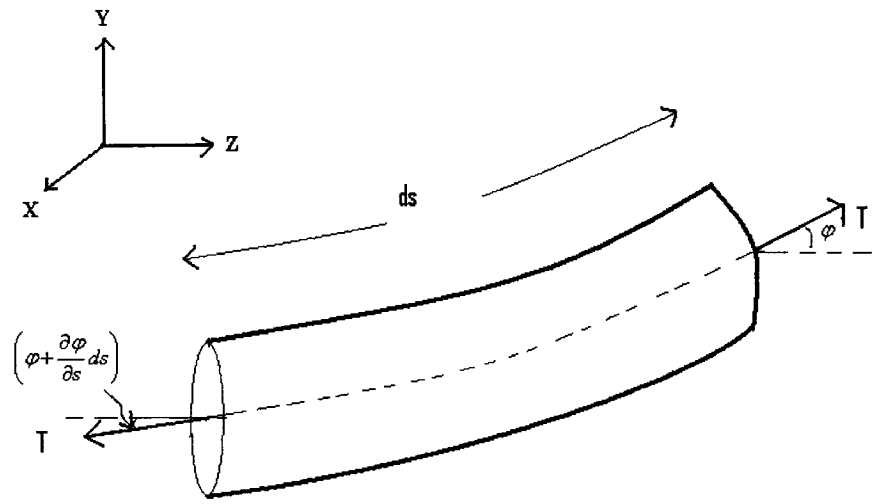

Fig 2.4: Segment of the cable

From Newton's laws of motion, the inertia force in downward direction is balanced by the upward component of tension.

Thus, considering motions in Y direction we have

$$\rho_m A_m (ds)\frac{\partial^2 y}{\partial t^2} = T\sin\left(\varphi + \frac{\partial \varphi}{\partial s} ds\right) - T\sin\varphi \qquad \text{- (2.5)}$$

where 'y' is the displacement in Y direction and 'φ' is the angle between the tension force and the horizontal and S is the curvilinear coordinate parallel to X and Y plane. Since φ is small, we have $\sin\varphi = \varphi$ and $\sin\left(\varphi + \frac{\partial \varphi}{\partial s} ds\right) = \left(\varphi + \frac{\partial \varphi}{\partial s} ds\right)$. Thus the equation (2.5) reduces to

$$\rho_m A_m (ds)\frac{\partial^2 y}{\partial t^2} = T\left(\varphi + \frac{\partial \varphi}{\partial s} ds\right) - T\varphi \qquad \text{- (2.6)}$$

The equation (2.6) reduces to

$$\rho_m A_m (ds)\frac{\partial^2 y}{\partial t^2} = T\left(\frac{\partial \varphi}{\partial s} ds\right) \qquad \text{- (2.7)}$$

From figure 2.4, the slope of the wire is given by $\varphi = \frac{\partial y}{\partial s}$. Thus substituting φ in equation (2.7) we have

$$\rho_m A_m \frac{\partial^2 y}{\partial t^2} - T\frac{\partial^2 y}{\partial s^2} = 0 \qquad \text{- (2.8)}$$

The equation (2.8) gives the governing differential equation of motion or wave equation of a string in Y-direction under free vibration condition. Similarly the equation of motion of the string in X- direction can be written as

$$\rho_m A_m \frac{\partial^2 x}{\partial t^2} - T\frac{\partial^2 x}{\partial s^2} = 0 \qquad \text{- (2.9)}$$

The above equations show that the system executes synchronous motions, which are defined as a motion in which every point performs the same type of motions in time [83]. These motions are characterized by the fact that, the ratio of displacement corresponding to two different points of the strings is constant in the whole time span. Mathematically synchronous motions can be separated in the spatial and time variables and hence displacement of a particular point at any time instant has the form

$$y(s,t) = G_Y(s)W(t) \qquad \text{- (2.10)}$$

and $$x(s,t) = G_X(s)W(t) \qquad \text{- (2.11)}$$

where G(s) is the spatial part and W (t) is the time dependent part of motions.

Substituting (2.10) in (2.8), we obtain

$$\left(\frac{1}{W}\right)\left(\frac{\rho_m A_m}{T}\right)\frac{\partial^2 W}{\partial t^2} = \frac{1}{G_Y}\frac{\partial^2 W}{\partial s^2} \qquad \text{- (2.12)}$$

The left side of the above equation is independent of s and the right is independent of t, thus it follows that each side must be a constant. Let this constant be $-(\omega/c)^2$ where $c = \sqrt{\frac{T}{\rho_m A_m}}$. The constant c is also known as velocity of wave propagation in the string. Thus we obtain two ordinary differential equations:

$$\frac{d^2 G_Y}{ds^2} + \left(\frac{\omega}{c}\right)^2 G_Y = 0 \qquad \text{- (2.13)}$$

$$\frac{d^2 W}{dt^2} + \omega^2 W = 0 \qquad \text{- (2.14)}$$

The general solutions of the above two differential equations are

$$G_Y = A\sin\frac{\omega}{c}s + B\cos\frac{\omega}{c}s \qquad \text{- (2.15)}$$

$$W = C\sin\omega t + D\cos\omega t \qquad \text{- (2.16)}$$

Substituting the boundary condition $y(0,t) = y(l,t) = 0$ of a string fixed at two points, yields

$$y = (C\sin\omega t + D\cos\omega t)\sin\frac{\omega}{c}s \qquad \text{- (2.17)}$$

and $\sin\frac{\omega l}{c} = 0$. Thus the natural frequency of the string in Y direction can be expressed as

$$\omega_{NY} = \frac{n\pi}{l}\sqrt{\frac{T}{\rho_m A_m}}; n = 1,2,3... \qquad \text{- (2.18)}$$

Similarly the equation (2.9) can be solved and the natural frequency in X direction is obtained as

$$\omega_{NX} = \frac{n\pi}{l}\sqrt{\frac{T}{\rho_m A_m}}; n = 1,2,3... \qquad \text{- (2.19)}$$

Thus the equations (2.8) and (2.9) represent the equations of motion of the transmission line conductor under free-vibration conditions with no external excitation and structural damping. The general solution of the equations (2.8) and (2.9) can be written as:

$$x(s,t) = \sum_{n=1}^{\infty}\left(A_n \sin\omega_n t + B_n \cos\omega_n t\right)\sin\frac{(n\pi)s}{l} \qquad \text{- (2.20)}$$

$$y(s,t) = \sum_{n=1}^{\infty}\left(C_n \sin\omega_n t + D_n \cos\omega_n t\right)\sin\frac{(n\pi)s}{l} \qquad \text{- (2.21)}$$

where A_n, B_n, C_n, D_n are arbitrary constants that can be obtained by substituting the initial conditions, $x(s,0), \dot{x}(s,0)$ and $y(s,0), \dot{y}(s,0)$ into the equations (2.20) and (2.21).

2.5 Response of transmission line cable under the action of wind alone

In the earlier section, transmission line conductor was modeled as vibrating string and the equations of motion were obtained for free vibration condition with no external excitations and structural damping. In this section, transmission line conductor under the action of wind and no ice load condition is considered.

As mentioned earlier, galloping is a phenomenon which usually occurs when wind blows over ice coated conductors. Figure 2.3.a showed a cross-section of the conductor in X-Y plane with wind blowing over the conductor. The segment of the conductor can be considered as a small cylinder placed in the direction of the wind flow. The conductor is assumed to make small displacements in X and Y directions. When wind blows over a cylinder, aerodynamic excitations are induced on it. These forces acting on the cylinder can be resolved into two components. The force which acts in the direction of the wind is called the drag while the one which acts perpendicular to the direction of the flow is lift [2].

The lift and drag forces can be expressed as follows [2]:

$$F_D = \frac{1}{2}\rho_a A_m U_r^2 C_D(\theta, U_r) \qquad \text{- (2.22)}$$

$$F_L = \frac{1}{2}\rho_a A_m U_r^2 C_L(\theta, U_r) \qquad \text{- (2.23)}$$

The figure 2.3.b showed the relative velocity diagram and hence relative velocity of wind with respect to the conductor can be found out as follows:

$$U_r^2 = \left(U - \dot{x}\right)^2 + \left(\dot{y}\right)^2 \qquad \text{- (2.24)}$$

$$\approx U^2 - 2U\dot{x} \text{ (Neglecting higher powers in } \dot{x} \text{ and } \dot{y}\text{)} \qquad \text{- (2.25)}$$

and α , the angle made by the relative wind velocity with horizontal, is

$$\tan\alpha = \frac{\dot{y}}{U - \dot{x}} \approx \frac{\dot{y}}{U} \text{ (} \dot{x} \text{ is neglected as it is much smaller than U)}$$

- (2.26)

The equations of transmission line conductor under the action of wind alone and no ice load is obtained by modifying the equations of vibrating strings (2.8) and (2.9) as follows.

$$\rho_m A_m \frac{\partial^2 x}{\partial t^2} - T\frac{\partial^2 x}{\partial s^2} = F_X \qquad \text{- (2.27)}$$

$$\rho_m A_m \frac{\partial^2 y}{\partial t^2} - T\frac{\partial^2 y}{\partial s^2} = F_Y \qquad \text{- (2.28)}$$

where F_X, F_Y are total forces in X and Y directions, respectively. From Fig 2.3.a, we have

$$F_X = F_D \cos\alpha - F_L \sin\alpha \qquad \text{- (2.29)}$$

$$F_Y = F_D \sin\alpha + F_L \cos\alpha \qquad \text{- (2.30)}$$

Since α is small, (2.29) and (2.30) can be written as

$$F_X = F_D - F_L\alpha \qquad \text{- (2.31)}$$

and $$F_Y = F_D\alpha + F_L \qquad \text{- (2.32)}$$

Substituting the expressions for F_D, F_L, U, α in F_X and F_Y, we have

$$F_X = \frac{1}{2}\rho_a A_m\left(U^2 - 2U\dot{x}\right)C_D - \frac{1}{2}\rho_a A_m\left(U^2 - 2U\dot{x}\right)C_L\left(\frac{\dot{y}}{U}\right) \qquad \text{- (2.33)}$$

Rearranging the above equation, we have

$$F_X = \frac{1}{2}\rho_a A_m C_D U^2 - \rho_a A_m U C_D \dot{x} - \frac{1}{2}\rho_a A_m U C_L \dot{y} + \rho_a A_m C_L \dot{x}\dot{y}$$

$$\Rightarrow F_X = \frac{1}{2} c_{XX} U - c_{XX} \dot{x} - \frac{1}{2} c_{XY} \dot{y} + \frac{c_{XY}}{U} \dot{x}\dot{y} \qquad \text{- (2.34)}$$

where $c_{XX} = \rho_a A_m U C_D$ and $c_{XY} = \rho_a A_m U C_L$

Similarly F_Y can be expressed as

$$F_Y = \frac{1}{2} \rho_a A_m C_L U^2 - \rho_a A_m U C_L \dot{x} + \frac{1}{2} \rho_a A_m U C_D \dot{y} - \rho_a A_m C_D \dot{x}\dot{y}$$

$$\Rightarrow F_Y = \frac{1}{2} c_{YX} U - c_{YX} \dot{x} + \frac{1}{2} c_{YY} \dot{y} - \frac{c_{YY}}{U} \dot{x}\dot{y} \qquad \text{- (2.35)}$$

where $c_{YX} = \rho_a A_m U C_L$ and $c_{YY} = \rho_a A_m U C_D$

Thus the equations of motion of transmission line conductor under the action of wind and no ice load are

$$\rho_m A_m \frac{\partial^2 x}{\partial t^2} - T \frac{\partial^2 x}{\partial s^2} = \frac{1}{2} c_{XX} U - c_{XX} \dot{x} - \frac{1}{2} c_{XY} \dot{y} + \frac{c_{XY}}{U} \dot{x}\dot{y} \qquad \text{- (2.36)}$$

$$\rho_m A_m \frac{\partial^2 y}{\partial t^2} - T \frac{\partial^2 y}{\partial s^2} = \frac{1}{2} c_{YX} U - c_{YX} \dot{x} + \frac{1}{2} c_{YY} \dot{y} - \frac{c_{YY}}{U} \dot{x}\dot{y} \qquad \text{- (2.37)}$$

The frequency of excitation or the forcing frequency is obtained from Strouhal number, given by

$$S = \frac{\omega D}{U} \qquad \text{- (2.38)}$$

where S is known as Strouhal number and is usually 0.18 to 0.22 for vibrating cylinders. D is the diameter of the conductor and U is the velocity of wind [5].

Runge - Kutta method is employed to solve the equations (2.36) and (2.37) in MATLAB and the responses of transmission line conductor in X and Y directions versus time and whirling motions are obtained. The simulation run is made for 3 seconds for a wind velocity of 5 m/s. The frequency of excitation obtained from Strouhal number for this particular wind speed is 30 radians per second or 4.8 Hz whereas the natural frequency in X and Y direction obtained from the equations (2.36) and (2.37) was 38 radian per second or 6.05 Hz.

When wind flows over a circular or a cylindrical section, there exists no lift force which means that the co-efficient of lift force (C_L) is zero [2]. However, when the cable has a non-cylindrical cross section due to ice accretions, there will be lift. For numerical computations, the co-efficient of lift force (C_L) when wind flows over the cylindrical surface is taken to be 0.65. The co-efficient of drag (C_D) is 1.

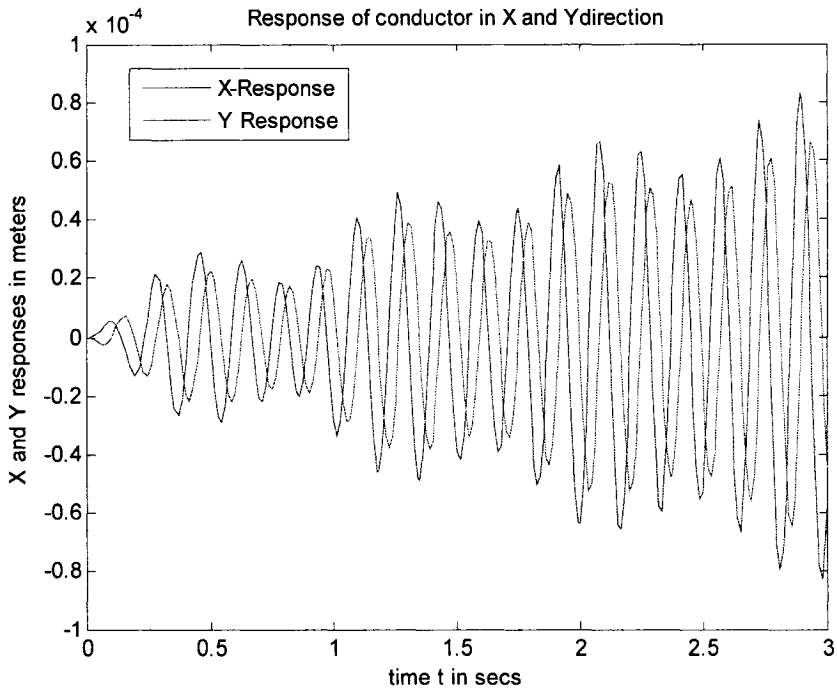

Fig 2.5: Responses of conductor in X and Y directions over time 't'

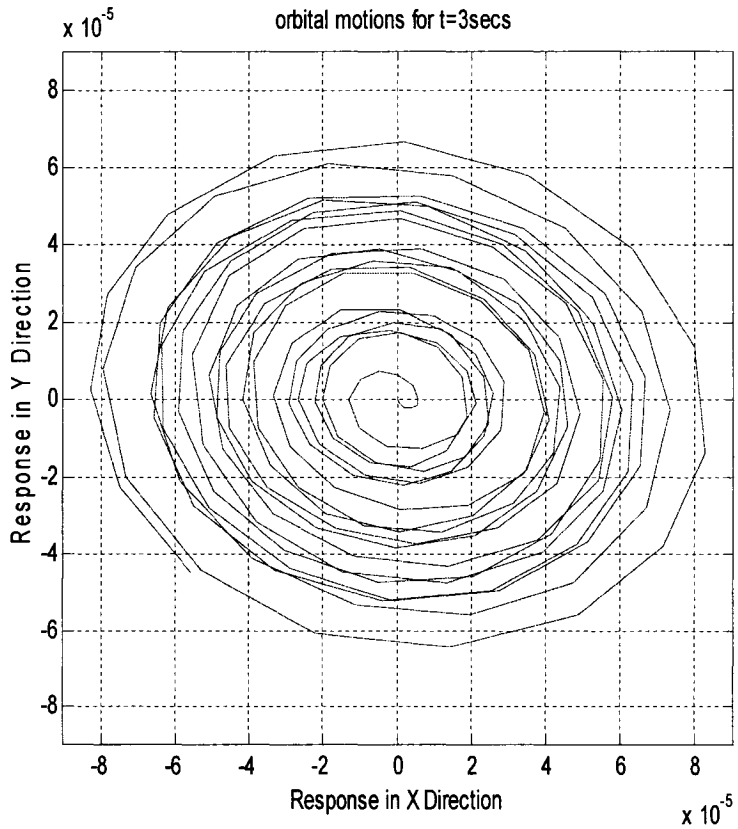

Fig 2.6: Orbital motions of conductor at 5 m/s. C_D =1 and C_L = 0.65; X-Y responses in meters

The figure 2.5 shows the X and Y direction displacement over time in three seconds. From the figure, it is clear that the transmission line conductor exhibits self excited vibrations. The amplitude starts at zero and keeps increasing over a given period of time. The maximum amplitude reached in 3 seconds is 0.2 mm. Similarly the response in Y-direction is shown in the same figure. The maximum amplitude in Y direction was 0.1 mm.

The figure 2.6 shows the orbital or whirling motions of the transmission line conductor for a period of 3 seconds. For a wind speed of 5 m/s, the shape of the orbit obtained is elliptical. If the co-efficient of lift force C_L was assumed to be 1, then the orbit obtained would be circular as shown in figure 2.8. But this never happens in transmission line galloping. Major axis is never on Y-axis as long as the cross-section of the cable is circular. In the later section, the flow of wind over ice accumulated cables would be studied, where the shape of the orbit is elliptical with major axis on X and Y axes depending upon the angle of wind incidence on the cables.

Figure 2.7 shows the orbital motions of the transmission line conductor at a wind speed of 5 m/s and $C_L = C_D = 1$

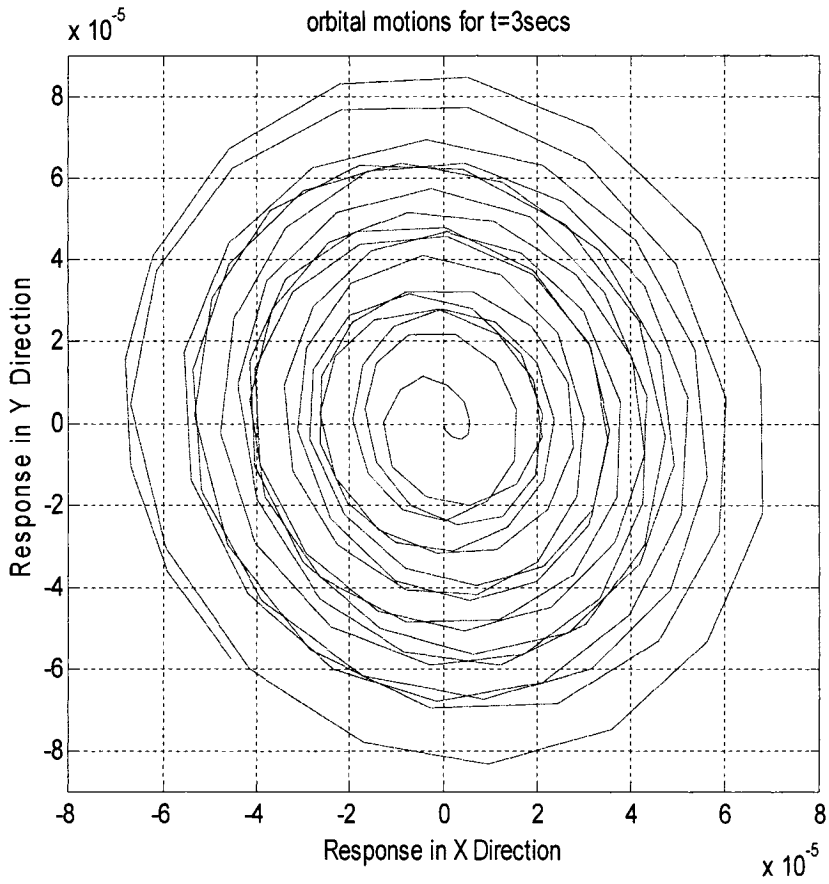

Fig 2.7: Orbital motions of conductor at 5 m/s. C_D =1 and C_L = 1; X-Y responses in meters

At a wind speed of approximately 6.2 m/s, resonance occurs in both X and Y directions. As mentioned earlier, the maximum amplitude of X is twice that of Y, since the co-efficient of drag (C_D = 1) is higher than the co-efficient of lift (C_L = 0.65).

The figure 2.8 shows the orbital motions of transmission line conductor at resonance. The shape of the orbit is elliptical with major axis on X –axis.

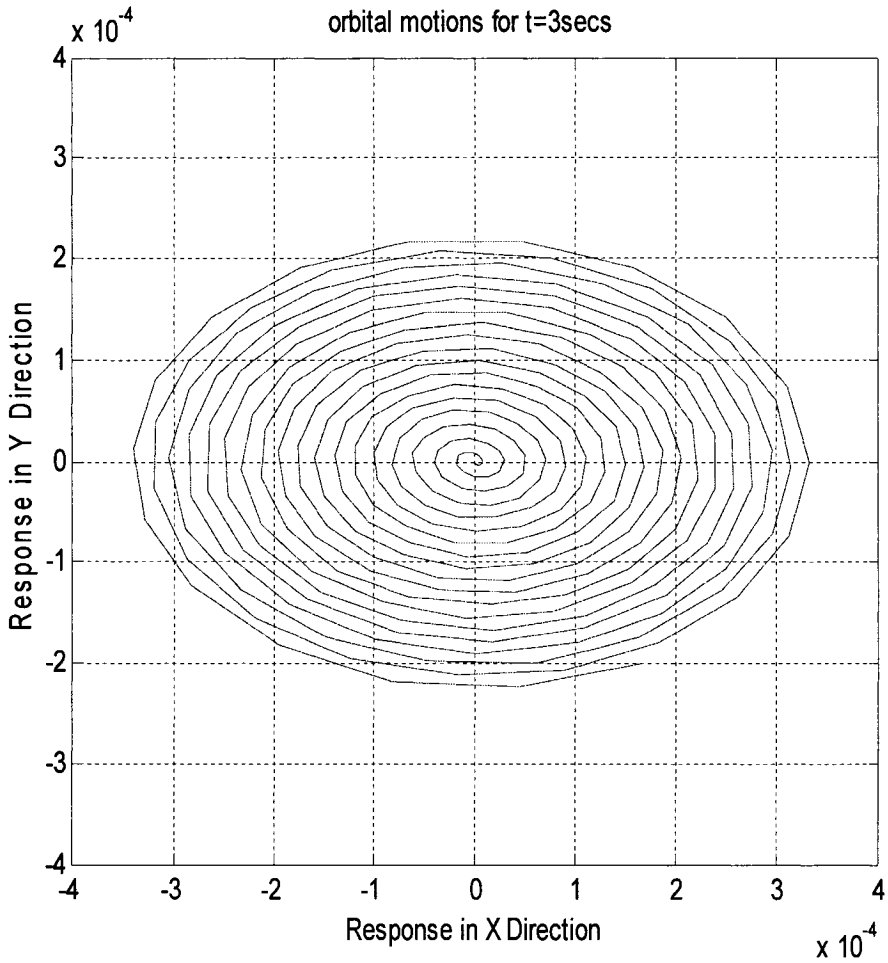

Fig 2.8: Orbital motions of conductor at 6.2 m/s. C_D =1 and C_L = 0.65; X-Y responses in meters

2.6 Phenomenon of sagging in transmission line

Probably no other structure other than transmission line cables has its mass in highly flexible form. The cables used for transferring heavy voltage electric currents are usually stranded in nature and are made up of Aluminium and Steel. The cable used for the present analysis is Bersfort 42/7 ACSR [Aluminium Conductor Steel Re-inforced] type of cable used in Hydro-Quebec research laboratories. The number indicates that the inner core of the cable is made up of 7 steel wires surrounded by 42 aluminium wires. The cable of the transmission line deflects under its own weight and the bending length of the cable is known as sag. As mentioned earlier, the profile of the sagging cable is assumed to be parabolic. The ratio of the sag to span length is a very useful data for the analysis. In the present work, sag to span ratio is taken as 1:8. Static analysis is performed on the cables and an expression for deflection 'y' is found in terms of the position co-ordinate's'. This expression is used in 'Irvine independent parameter (λ)' [22], explained in section 2.6.2 when dynamic analysis on cables is performed and hence equation of motion of the cable is obtained taking sagging into consideration.

2.6.1 Static analysis

A sagging cable between any two towers is considered and the free-body diagram of a segment of the line is shown below in figure 2.9.

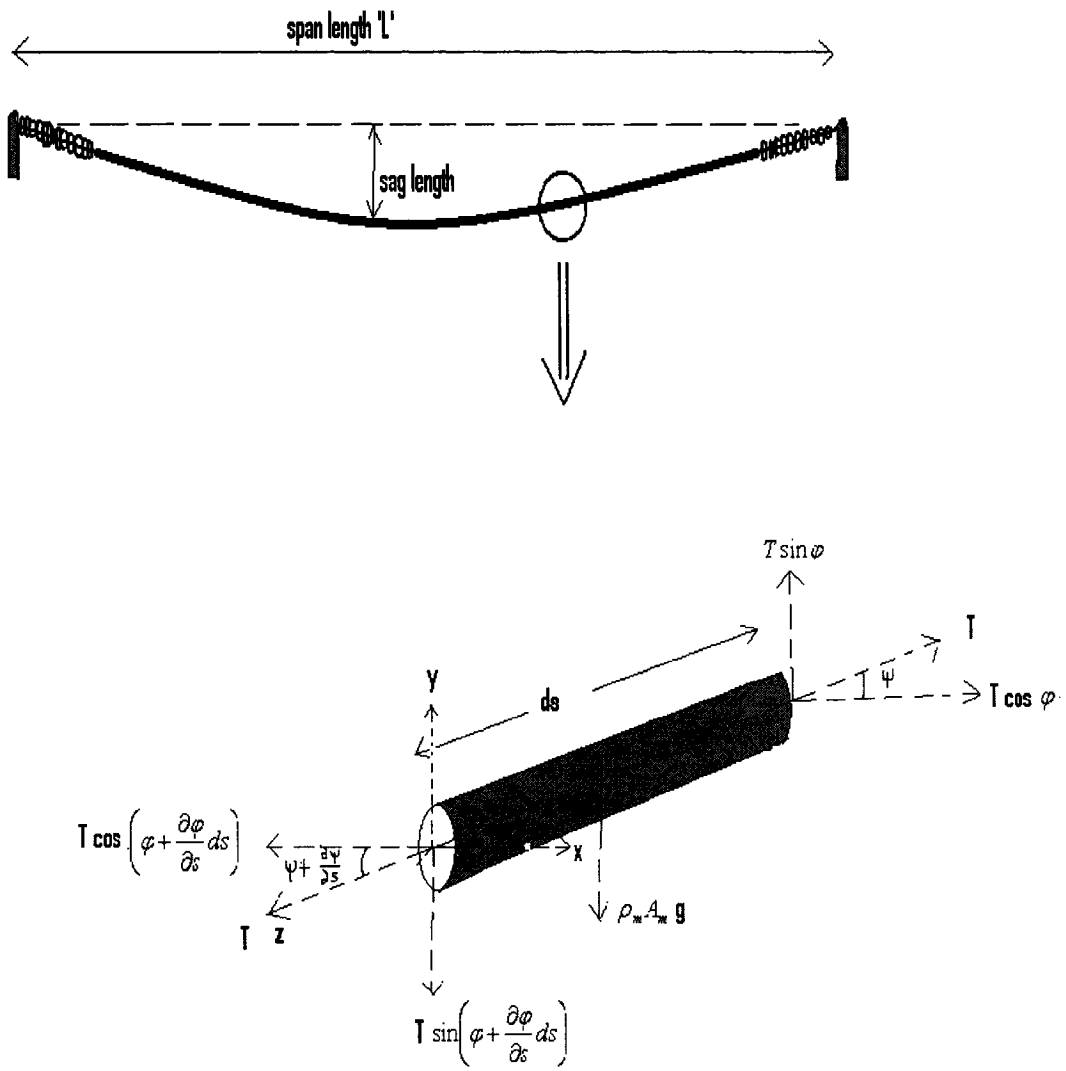

Fig 2.9: Free body diagram of the conductor showing the forces acting on it under static condition

The figure 2.9 above shows the forces acting on a small segment of the cable. Under equilibrium conditions, the weight of the cable is balanced by the differential vertical components of tension force. Thus from figure 2.10, we have

$$\rho_m A_m g(ds) + T\sin\left(\varphi + \frac{\partial\varphi}{\partial s}ds\right) - T\sin\varphi = 0 \qquad \text{- (2.39)}$$

The equation (2.39) can be written as

$$\rho_m A_m g(ds) = -T\sin\left(\varphi + \frac{\partial\varphi}{\partial s}ds\right) + T\sin\varphi \qquad \text{- (2.40)}$$

where φ is the angle between the tension force and the horizontal. Since φ is small, we have $\sin\varphi = \varphi$ and $\sin\left(\varphi + \frac{\partial\varphi}{\partial s}ds\right) = \left(\varphi + \frac{\partial\varphi}{\partial s}ds\right)$. Also from figure 2.9, φ is the slope of the segment and thus can be expressed as $\varphi = \frac{\partial y}{\partial s}$. The equation (2.40) can be written as

$$\rho_m A_m g = -T\frac{\partial^2 y}{\partial s^2} \qquad \text{- (2.41)}$$

The equation (2.41) is rearranged and integrated twice on both sides with respect to's'. Thus (2.41) yields

$$T\int\int\frac{\partial^2 y}{\partial s^2}ds = -\iint(\rho_m A_m g)ds \qquad \text{- (2.42)}$$

$$\Rightarrow Ty = \frac{-\rho_m A_m g s^2}{2} + C_1 s + C_2 \qquad \text{- (2.43)}$$

The constants C_1 and C_2 in (2.43) can be found by applying the boundary conditions y = 0; s = 0 and y = 0; s = l. Thus

$$C_1 = \frac{\rho_m A_m g l}{2}; C_2 = 0 \qquad \text{- (2.44)}$$

Substituting (2.44) in (2.43), the deflection of cable 'y' in terms of position co-ordinate 's' is obtained as follows:

$$y = \frac{\rho_m A_m g}{2T} s(l - s) \qquad \text{- (2.45)}$$

The equation (2.45) is used in the dynamic analysis to obtain the equations of motions of the cable under sagging condition.

2.6.2 Dynamic analysis

Dynamic analysis is performed on the transmission line cable and the effect of sagging is studied. It is assumed that sagging affects motion only in vertical direction and hence the equation of motion in x- direction remains unaffected. According to H. M. Irvine [22] the equation of motion in Y – direction is obtained as follows:

Applying Newton's laws of motions to a small segment of the cable, we have

$$\rho_m A_m (ds)\frac{\partial^2 y}{\partial t^2} = T\sin\left(\varphi + \frac{\partial \varphi}{\partial s} ds\right) - T\sin\varphi + \rho_m A_m g(ds) + h(t)ds \qquad \text{- (2.46)}$$

where h (t) is additional tension generated by the cable in motion. The term h (t) is given by [22]

$$h(t) = \lambda^2 \int_0^L y(s,t)ds \qquad \text{- (2.47)}$$

The term λ^2 is known as the Irvine independent parameter [22] and is given by

$$\lambda^2 = \left(\frac{\rho_m A_m g l}{T}\right)^2 \frac{EA_m l}{L_e} \qquad \text{- (2.48)}$$

where L_e is the stretched length of the cable. From static analysis we have

$$y(s,t) = \frac{\rho_m A_m g}{2T} s(l-s) \qquad \text{- (2.49)}$$

2.7 Ice accretion on the transmission lines

Snow and Ice accretions on overhead cables are serious problems, yet no recognized physical models have been established. In the present work, the shape of the ice is taken from the previous work done by O. Chabart and J.L. Lilien [16]. The shape of the ice accretion on transmission line by Chabart and Lilien is shown in the figure 2.10. They used wooden mould to represent ice on transmission line and performed experiments in the wind tunnel to obtain the various values of co-efficient of drag, lift and moment forces under different angles of attack. These values are used in the present analysis to compute the lift and drag forces acting on the cable and hence whirling motions at different wind speeds and angles of attack are found.

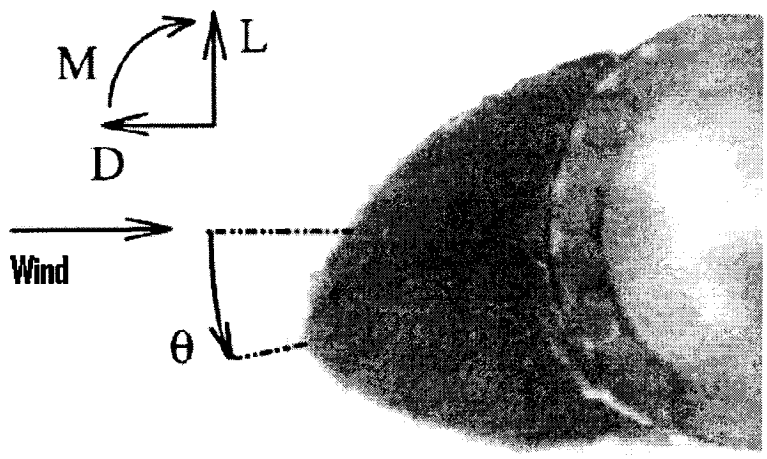

Fig 2.10: Cross-section of the conductor showing the ice accumulation with an angle of attack of θ taken from O.Chabart's work [16].

The figure 2.11 below shows the values of co-efficient of drag (C_D), lift (C_L) and moment (C_M) forces under different angles of attack [16]. It is assumed that these values remain unchanged for different wind speeds.

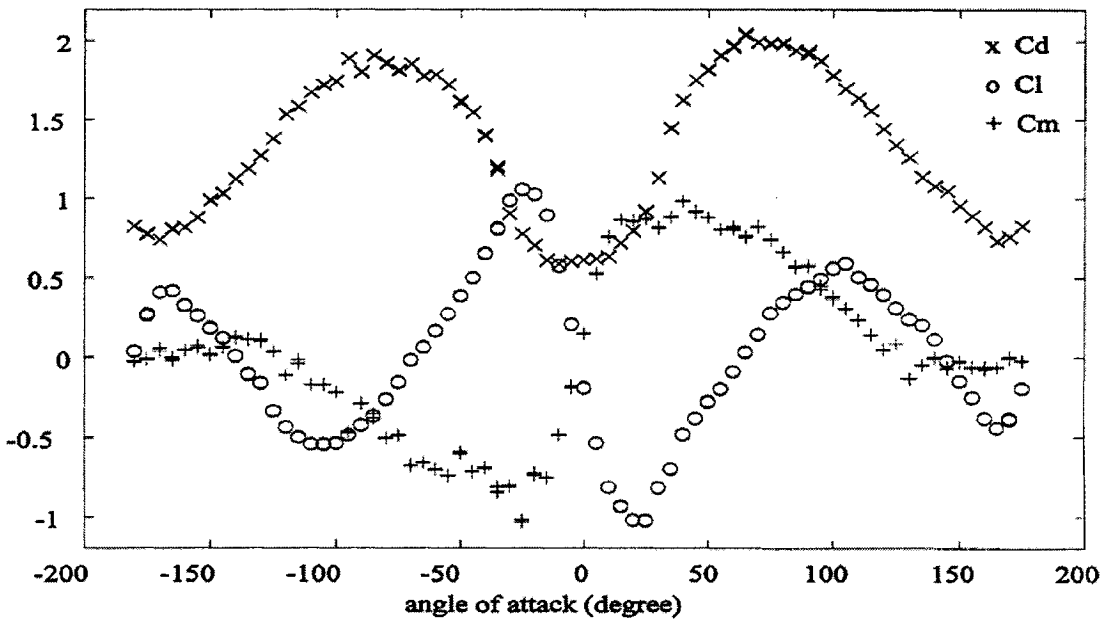

Fig 2.11: Values of the C_D, C_L, and C_M at various angles of attack θ [16]

2.7.1 Angle of attack

In the analysis, the angle of attack is taken to be the angle between the line joining the centre of the conductor and centre of gravity of ice with the direction of the actual wind flow. The figure 2.12 shows different angles of attack for a particular wind speed.

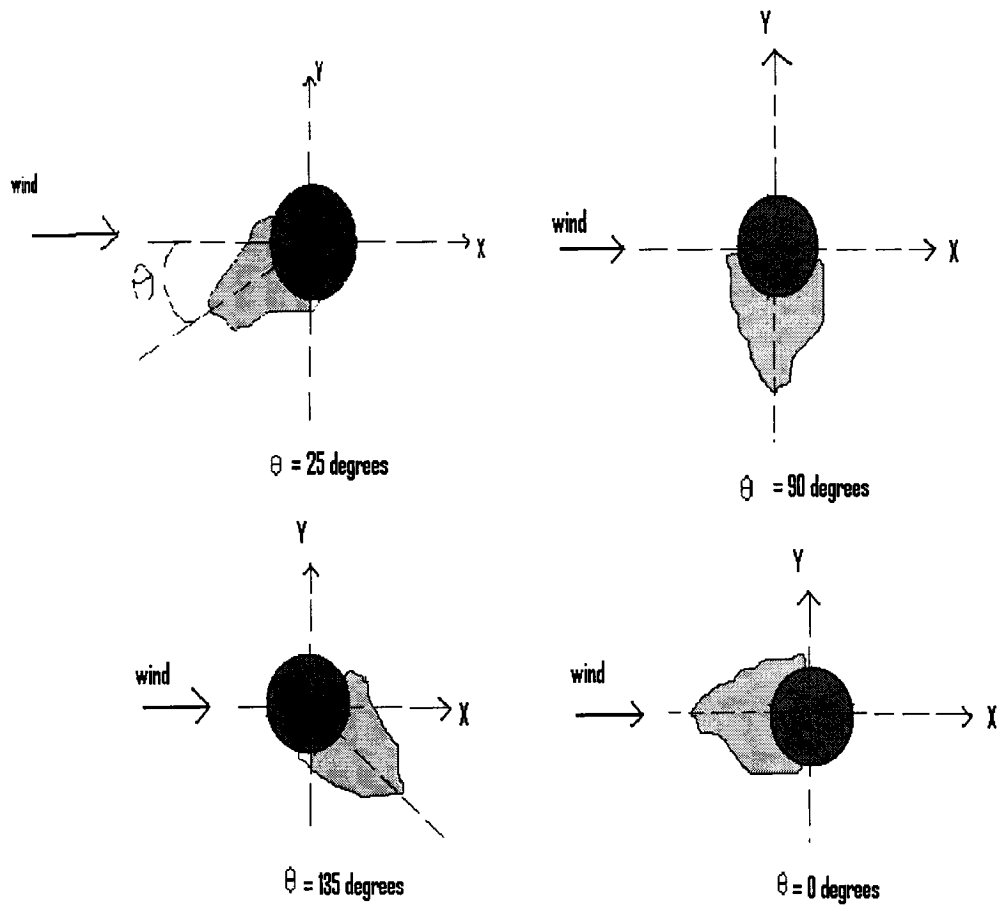

Fig 2.12: Shapes of ice accreted conductor cable under various angles of attack.

2.8 Aerodynamic excitations considering ice loads

In the section 2.4 above, response of transmission line under the action of wind alone was studied. In this section response of the transmission line cable with wind and ice is considered for analysis. Figure 2.13.a below shows the cross-section of the transmission line cable accreted with conical shaped ice and is perpendicular to the direction of the wind flow.

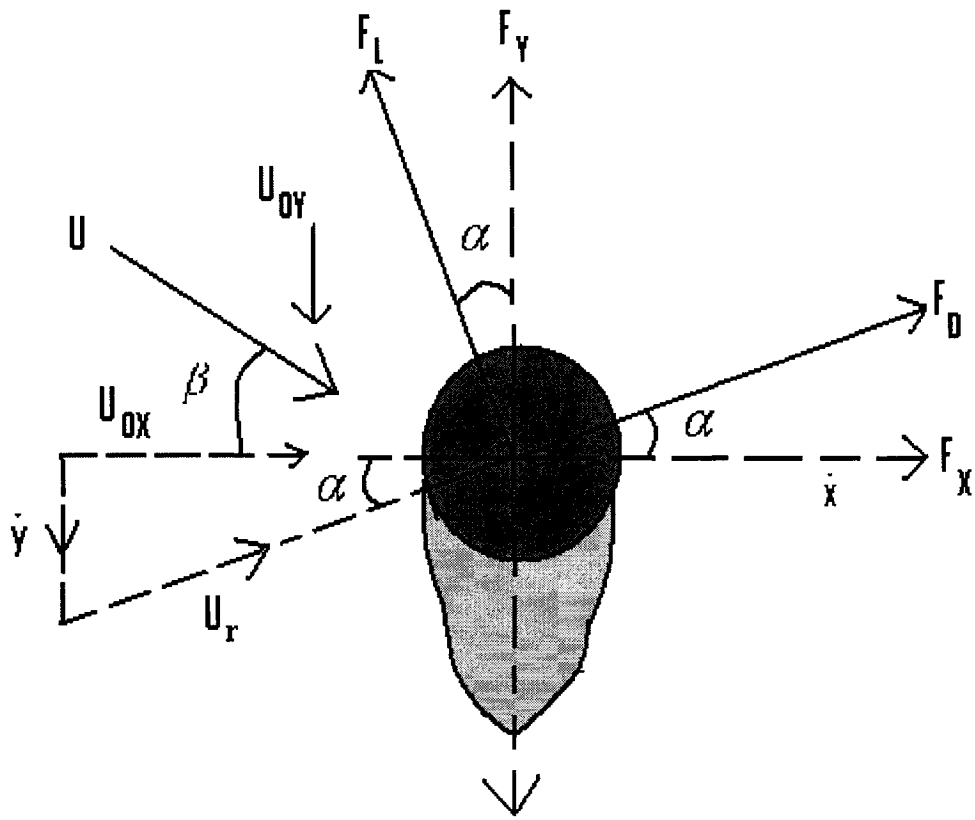

Fig 2.13 a.: Free body diagram of the ice accreted conductor under the action of the wind.

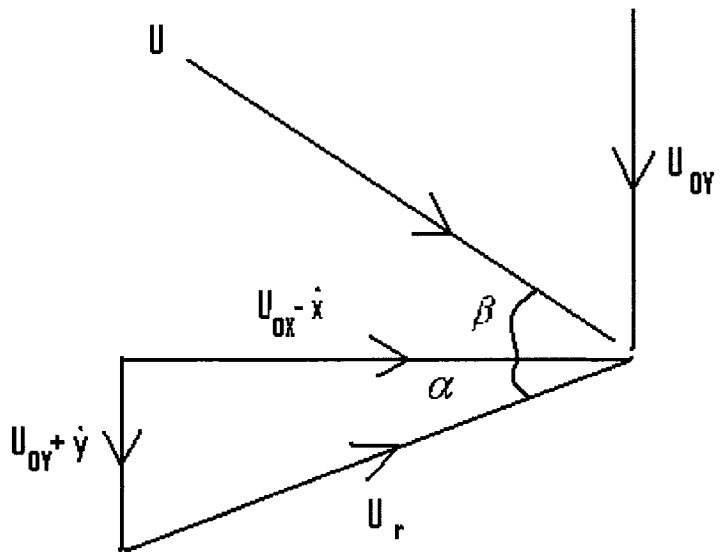

Fig 2.13 b.: Relative velocity diagram

It is assumed that the wire vibrates with small velocities in X and Y directions, respectively. Thus from the figure 2.13.b, the relative velocity between the wire and wind can be found as follows:

$$U_r^2 = \left(U_{ox} - \dot{x}\right)^2 + \left(U_{oy} + \dot{y}\right)^2 \qquad \text{- (2.50)}$$

where U_{ox} and U_{oy} are the horizontal and vertical component of the wind velocities. If the wind flows with a velocity 'U' m/s at an angle 'β' to the horizontal, then the horizontal and vertical components are given as

$$U_{ox} = U\cos\beta, \text{ and} \qquad \text{- (2.51)}$$

$$U_{oy} = U\sin\beta \qquad \text{- (2.52)}$$

Thus substituting 2.51 and 2.52 in 2.50, the relative velocity can be written as

$$U_r^2 = U_{ox}^2 - 2U_{ox}\dot{x} + 2U_{oy}\dot{y} + U_{oy}^2 \text{ [Neglecting the higher powers of x and y]}$$

$$= U^2 - 2U_{ox}\dot{x} + 2U_{oy}\dot{y}, \ [U_{ox}^2 + U_{oy}^2 = U^2] \qquad \text{- (2.53)}$$

From fig 2.13.b, α is small and is given as

$$\tan\alpha = \frac{U_{oy} + \dot{y}}{U_{ox} - \dot{x}} \approx \frac{U_{oy} + \dot{y}}{U_{ox}}$$

where 'α' is the angle between the relative wind velocity U_r with the horizontal.

The drag and lift forces are given by [2]

$$F_D = \frac{1}{2}\rho_a A_m U_r^2 C_D(\theta, U_r) \qquad \text{- (2.54)}$$

$$F_L = \frac{1}{2}\rho_a A_m U_r^2 C_L(\theta, U_r) \qquad \text{- (2.55)}$$

From fig 2.13.a, the total horizontal and vertical component of the forces can be obtained as follows:

$$F_x = F_D \cos\alpha - F_L \sin\alpha \quad \text{- (2.56)}$$

$$F_y = F_D \sin\alpha + F_L \cos\alpha \quad \text{- (2.57)}$$

Substituting the values of α, F_D and F_L in (2.56) and (2.57), F_x and F_y can be found out as follows

$$F_y = F_D \sin\alpha + F_L \cos\alpha \approx F_D\alpha + F_L \quad \text{- (2.58)}$$

$$= \frac{1}{2}\rho_a A U_r^2 [C_D\alpha + C_L] \quad \text{- (2.59)}$$

$$F_y = \frac{1}{2}\rho_a A\left(U^2 - 2U_{ox}\dot{x} + 2U_{oy}\dot{y}\right)\left[C_D\left(\frac{U_{oy}+\dot{y}}{U_{ox}}\right) + C_L\right] \quad \text{- (2.60)}$$

Simplifying the above equation we have

$$F_y = \frac{1}{2}\rho_a A\left[U^2\left(\frac{C_D U_{oy}}{U_{ox}} + C_L\right) + \dot{y}\left(\frac{U^2 C_D}{U_{ox}} + \frac{2U_{oy}^2 C_D}{U_{ox}} + 2U_{oy}C_L\right) - 2\dot{x}\left(C_D U_{oy} + C_L U_{ox}\right) - 2\dot{x}\dot{y}C_D\right] \quad \text{- (2.61)}$$

Thus $F_y = \frac{1}{2}\rho_a A U^2 C_{Y1} + C_{Y2}\,\dot{y} - 2\dot{x}C_{Y3} - \rho_a A\,\dot{x}\,\dot{y}\,C_D$ - (2.62)

where $C_{Y1} = \left(\frac{C_D U_{oy}}{U_{ox}} + C_L\right)$

$$C_{Y2} = \frac{1}{2}\rho_a A\left(\frac{U^2 C_D}{U_{ox}} + \frac{2U_{oy}^2 C_D}{U_{ox}} + 2U_{oy}C_L\right)$$

$$C_{Y3} = \frac{1}{2}\rho_a A\left(U_{oy}C_D + U_{ox}C_L\right)$$

Similarly horizontal force can be obtained as follows

$$F_X = \frac{1}{2}\rho_a A\left[U^2\left(C_D - \frac{C_L U_{oy}}{U_{ox}}\right) + \dot{y}\left(2U_{oy}C_D - \frac{U^2 C_L}{U_{ox}} - \frac{2U_{oy}^2 C_L}{U_{ox}}\right) + 2\dot{x}\left(-C_D U_{ox} + C_L U_{oy}\right) + 2\dot{x}\,\dot{y}\,C_L\right]$$

- (2.63)

Simplifying 2.63, we have

$$F_X = \frac{1}{2}\rho_a A U^2 C_{X1} + C_{X2}\,\dot{y} + 2\dot{x}C_{X3} - \rho_a A\,\dot{x}\,\dot{y}\,C_L$$ - (2.64)

where $C_{X1} = \left(C_D - \frac{C_L U_{oy}}{U_{ox}}\right)$,

$$C_{X2} = \frac{1}{2}\rho_a A\left(2U_{oy}C_D - \frac{U^2 C_L}{U_{ox}} - \frac{2U_{oy}^2 C_L}{U_{ox}}\right)$$

$$C_{X3} = \frac{1}{2}\rho_a A\left(-U_{ox}C_D + U_{oy}C_L\right)$$

2.9 Equations of motion of transmission lines with ice and wind loads

The equations of motion of transmission lines considering sagging, wind and ice loads can be formulated as follows:

In X-direction

$$\rho_m A_m \frac{\partial^2 x}{\partial t^2} - T\frac{\partial^2 x}{\partial s^2} = F_x \qquad \text{- (2.65)}$$

In Y-direction

$$\rho_m A_m (ds)\frac{\partial^2 y}{\partial t^2} - T\frac{\partial^2 y}{\partial s^2} - \rho_m A_m g - h(t) = F_Y \qquad \text{- (2.66)}$$

Substituting the values of F_x and F_y in (2.65) and (2.66), the equations of motions are

$$\rho_m A_m \frac{\partial^2 x}{\partial t^2} - T\frac{\partial^2 x}{\partial s^2} = \frac{1}{2}\rho_a A U^2 C_{X1} + C_{X2}\dot{y} + 2\dot{x}C_{X3} - \rho_a A \dot{x}\dot{y}C_L$$

- (2.67)

$$\rho_m A_m (ds)\frac{\partial^2 y}{\partial t^2} - T\frac{\partial^2 y}{\partial s^2} - \rho_m A_m g - h(t) = \frac{1}{2}\rho_a A U^2 C_{Y1} + C_{Y2}\dot{y} - 2\dot{x}C_{Y3} - \rho_a A \dot{x}\dot{y}C_D$$

- (2.68)

Rearranging the above equations (2.67) and (2.68), we have the equations of motions as

$$\rho_m A_m \frac{\partial^2 x}{\partial t^2} - C_{X2}\dot{y} - 2\dot{x}C_{X3} + \rho_a A \dot{x}\dot{y}C_L - T\frac{\partial^2 x}{\partial s^2} = \frac{1}{2}\rho_a A U^2 C_{X1}$$

- (2.69)

$$\rho_m A_m \frac{\partial^2 y}{\partial t^2} - C_{Y2}\dot{y} + 2\dot{x}C_{Y3} + \rho_a A \dot{x}\dot{y}C_D - T\frac{\partial^2 y}{\partial s^2} - \rho_m A_m g - h(t) = \frac{1}{2}\rho_a A U^2 C_{Y1}$$

- (2.70)

2.10 Summary

This chapter starts with a brief introduction to self excited vibrations and Den-Hartog's principle of galloping. The equations of motion of the transmission line cable were derived with and without considering the sagging of the cable, aerodynamic excitations and ice load. The factors responsible for transmission line galloping and the shape of the ice were included. The equations of motion of the transmission line were solved using Runge – Kutta method in MATLAB and the simulation results analyzing various factors are studied in chapter 3.

CHAPTER 3

SIMULATION RESULTS

3.1 General

In the previous chapter, the equations of motion of transmission line cables were derived with and without considering the sagging, subjected to wind and ice load. The analysis was performed on BERSFORT 42/7 ACSR cable. It is an Aluminium Conductor Steel Reinforced cable with the inner core consisting of seven steel wires surrounded by 42 stranded Aluminium wires. The stranded property of the cable makes the cable tensionally rigid. The figure 3.1 below shows a sample piece of BERSFORT cable obtained from HYDRO-QUEBEC Research Laboratories and table 3.1 gives the properties of the cable.

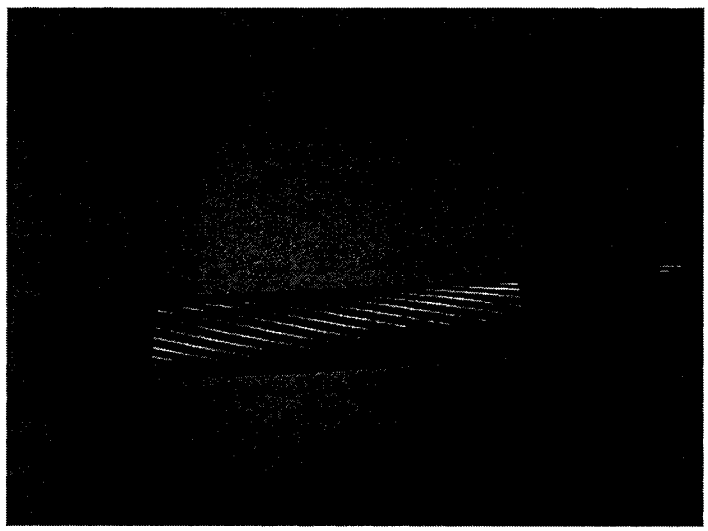

Fig 3.1: Transmission line cable

The properties of the cable used for simulation is listed below in the table 3.1

Cable type	42/7 ACSR BERSFORT
Length of the span (l)	142 m
Diameter of the conductor (D_m)	35.56 mm
Density of ice (ρ_i)	917 Kg/m^3
Density of air (ρ_a)	1.25 Kg/m^3
Mass per unit length of the conductor	2.375 kg/m
Area of the conductor (A_m)	747 mm^4
Area of the ice section (A_i)	58 mm^4

Table 3.1: Properties of the transmission line cable

The natural frequencies of the cable on solving the equations 2.69 and 2.70 for free vibration condition are given in the table 3.2 below.

Natural Frequency in X direction	39.35 rad/s
Natural Frequency in Y-direction	39.19 rad/s

Table 3.2: Natural frequencies of the cable under free vibration condition

3.2 Factors influencing orbital motions of the transmission line cable

The equations of motion of the transmission line cable derived from the previous chapter 2.69 and 2.70 are as follows:

In X-direction

$$\rho_m A_m \frac{\partial^2 x}{\partial t^2} - C_{X2}\,\dot{y} - 2\dot{x}C_{X3} + \rho_a A\,\dot{x}\,\dot{y}\,C_L - T\frac{\partial^2 x}{\partial s^2} = \frac{1}{2}\rho_a A U^2 C_{X1} \qquad \text{- (3.1)}$$

In Y-direction

$$\rho_m A_m \frac{\partial^2 y}{\partial t^2} - C_{Y2}\,\dot{y} + 2\dot{x}C_{Y3} + \rho_a A\,\dot{x}\,\dot{y}\,C_D - T\frac{\partial^2 y}{\partial s^2} - \rho_m A_m g - h(t) = \frac{1}{2}\rho_a A U^2 C_{Y1}$$

- (3.2)

Fourth order Runge - Kutta method is employed to solve the equations in MATLAB and thus orbital motions are obtained. The orbital motions of the transmission line cable depend on the following three parameters:

- Wind velocity 'U'
- Angle of attack 'θ'
- Angle of incidence of wind on wire 'β'

By varying the above parameters, the orbital motions of the transmission lines are obtained. For a particular angle of attack of the ice accreted cable, two different angles of wind incidence on the cable are studied and for each angle of wind incidence four different speeds are employed to analyze the orbits. The natural frequencies in X and Y directions are $\omega_{nX} = 39.35$ rad/sec and $\omega_{nY} = 39.19$ rad/sec.

3.2.1 Lissajous figures

This is the family of curves which are described by a point whose motion is the resultant of two simple harmonic motions in perpendicular directions [84]. In general the motions have different periods and amplitudes and a great variety of patterns result. If the periods are equal we obtain various kinds of ellipses; if one period is twice the other, we obtain various quartics, with the lemniscates of Bernoulli and the repeated arc of parabola as a special case. In the present work, these figures are termed as orbital motions.

3.3 Orbital motions of transmission line when the angle of attack $\theta = 0°$

As mentioned earlier, the angle of attack is the angle between the lines joining the centre of the cable to the center of gravity of the ice to the horizontal. Figure 3.2 below shows the cross sectional view of the cable accreted with ice when the

angle of attack is zero. The co-efficient of drag and lift forces for a particular angle of attack can be obtained from the figure 2.12 of the previous chapter.

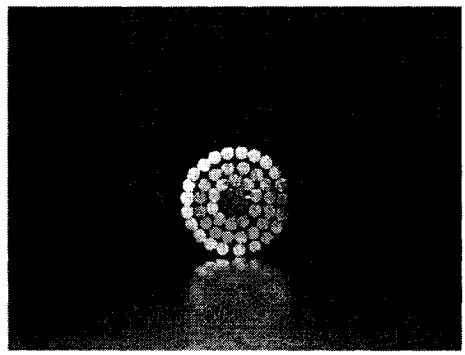

Fig 3.2: Cross section of cable with ice model at $\theta = 0°$

3.3.1 When the angle of incidence of wind $\beta = 0°$

The figure 3.3.a shows the schematic sketch of the conductor and ice model when the angle of attack is zero and angle of incidence of the wind on conductor is also zero. For every angle of incidence of wind β, orbital motions are found by varying the wind speed U from 5 m/s to 15 m/s.

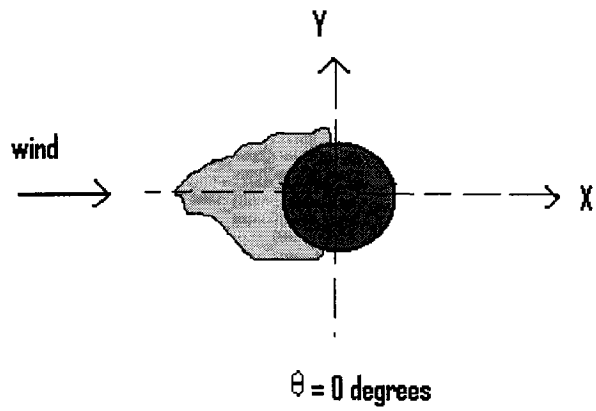

Fig 3.3.a: Sketch of conductor-ice model at $\theta = 0°$ and $\beta = 0°$

3.3.1.1 At wind speed U = 5 m/s

The responses in X and Y directions versus time 't' are shown in figure 3.3.b. The figure 3.3.c shows the corresponding Lissajous figure or the orbital motions of conductor-ice model when the wind flows over the conductor at 5 m/s. The simulation was initially made to run for 5 seconds.

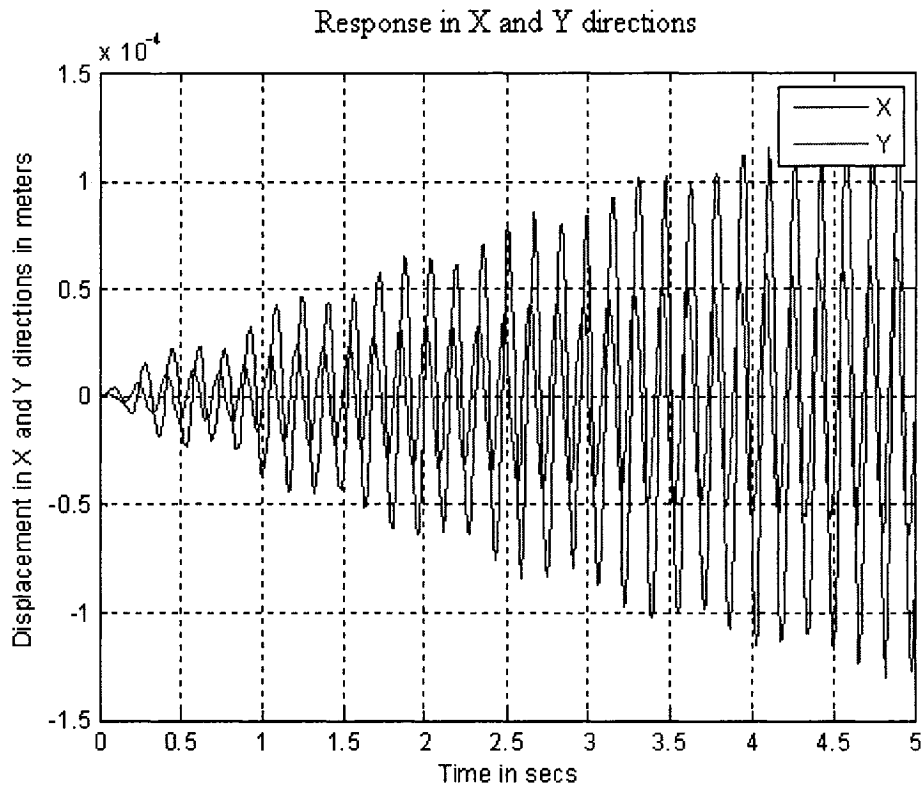

Fig 3.3.b: Responses in X and Y directions versus time't'

The Lissajous figure shows the resultant of the responses as ellipse with major axes on X. The figure was divided into four quadrants namely I, II, III and IV. During the first 5 seconds of the simulation, we see that the orientations of the orbits are in the quadrants II and III. As the time increases, the amplitudes in X and Y directions increase and thus we obtain ellipse with increased radius of rotation as shown in figure 3.3.d.

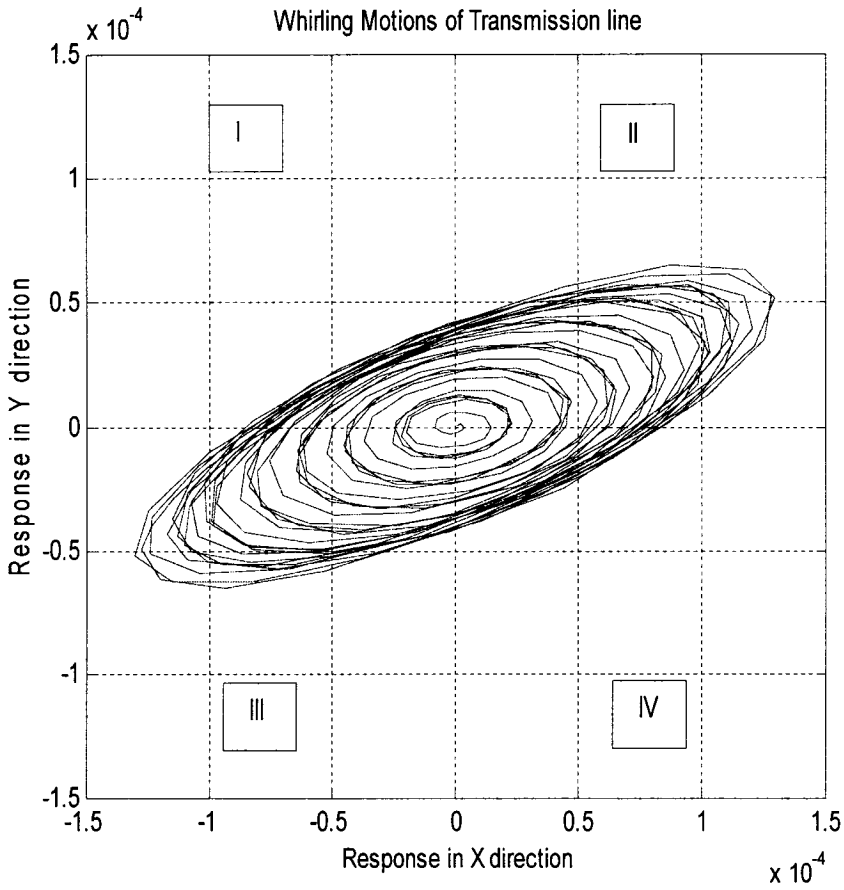

Fig 3.3.c: Whirl motions at U=5m/s; $\beta = 0°$; $\theta = 0°$; t = 5 seconds; X – Y responses in meters

When the simulation time was increased to 15 seconds, the Lissajous figure obtained is shown below in figure 3.3.d. The figure shows orbital orientations in the quadrants II and III with increase in the radius of rotation and orbits.

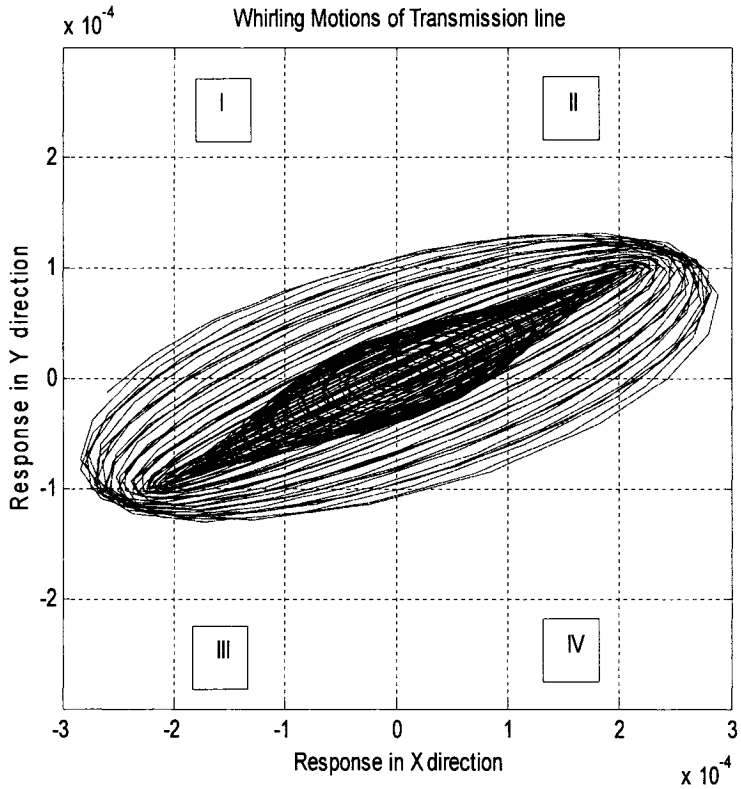

Fig 3.3.d: Whirl motions at U = 5m/s; $\beta = 0°$; $\theta = 0°$; t = 15 seconds; X – Y responses in meters

When the simulation time was increased to 25 seconds, the Lissajous figure obtained is shown below in figure 3.3.e. In the figure 3.3.e, the orientation of the orbits has changed from the quadrants II and III to I and IV. This shows that as the simulation time increases, the aerodynamic instability keeps increasing with orientation of the orbits changing between the planes.

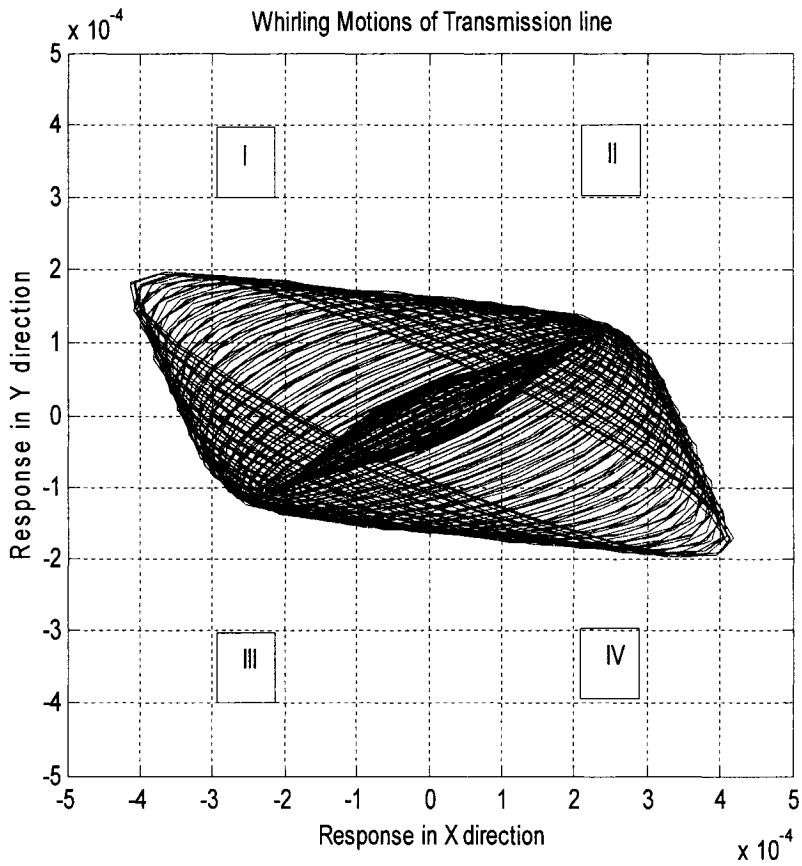

Fig 3.3.e: Whirl motions at U=5m/s; $\beta = 0°$; $\theta=0°$; t = 25 seconds; X – Y responses in meters

3.3.1.2 At wind speed U = 6.4 m/s

Lissajous figure or the orbital motions of the conductor-ice model are obtained for various simulation times when the speed of the wind flow is 6.4 m/s.

For a simulation time of 5 seconds, the Lissajous figure is shown in the figure 3.4.a. Initially the orientation of the orbits is in the quadrants II and III as discussed in the section 3.3.1.1.

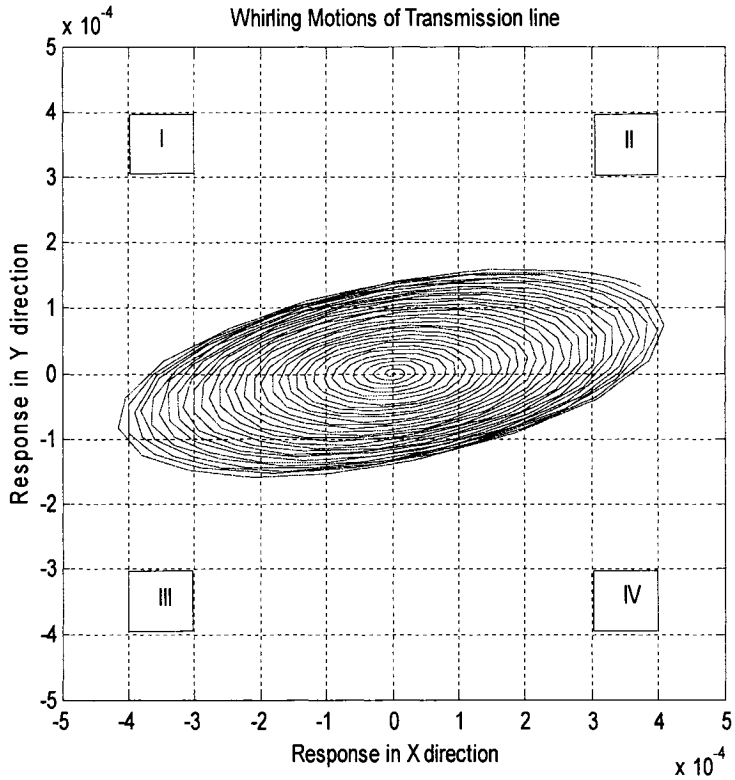

Fig 3.4.a: Whirl motions at U = 6.4m/s; $\beta = 0°$; $\theta=0°$; t =5 seconds; X – Y responses in meters

When the simulation time is increased to 15 seconds, the Lissajous figure obtained is shown in the figure 3.4.b.

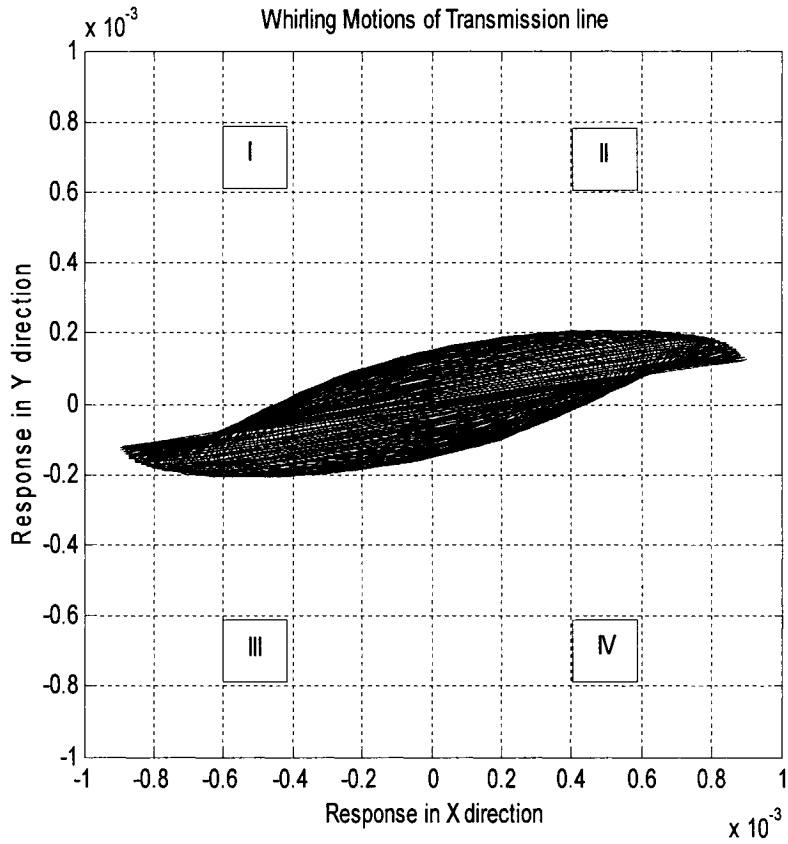

Fig 3.4.b: Whirl motions at U = 6.4m/s; $\beta = 0°$; $\theta=0°$; t =15 seconds; X – Y responses in meters

The Lissajous figure for a simulations time of 25 seconds is shown in the figure 3.4.c below. From the figure, it can be noticed that the orientation of the orbits changes from the quadrants II and III to I and IV.

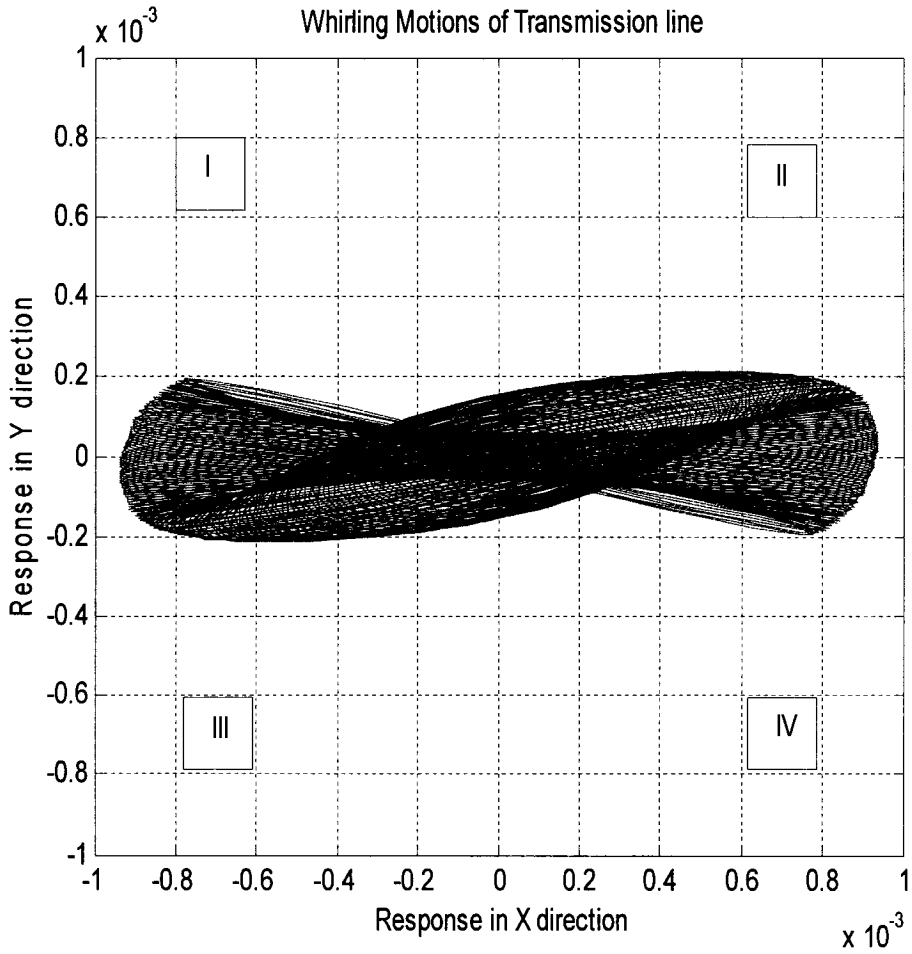

Fig 3.4.c: Whirl motions at U = 6.4m/s; $\beta = 0°$; $\theta = 0°$; t = 25 seconds; X – Y responses in meters

3.3.1.3 At wind speed U = 9.5 m/s

The Lissajous figures are obtained for two different simulation times when the speed of the wind flow over the conductor is 9.5 m/s. These are shown in figures 3.5.a and 3.5.b for simulation times of 5 and 25 seconds, respectively.

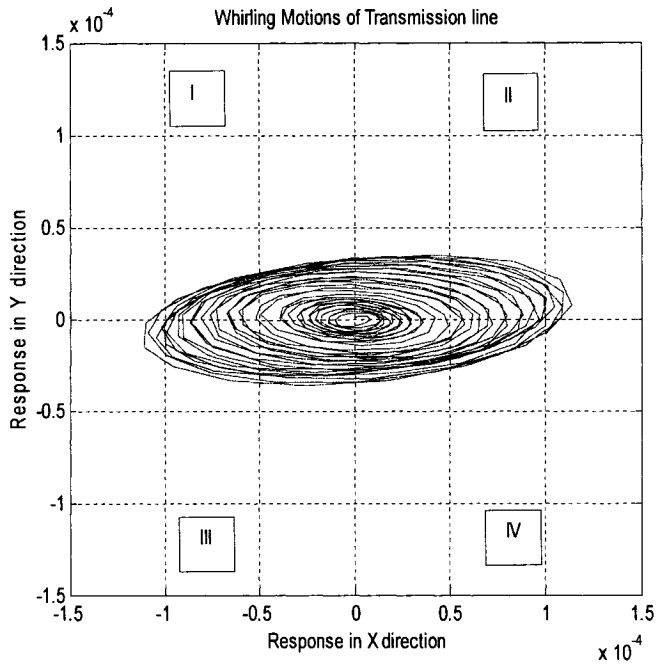

Fig 3.5.a: Whirl motions at U = 9.5 m/s; $\beta = 0°$; $\theta = 0°$; t = 5 seconds; X – Y responses in meters

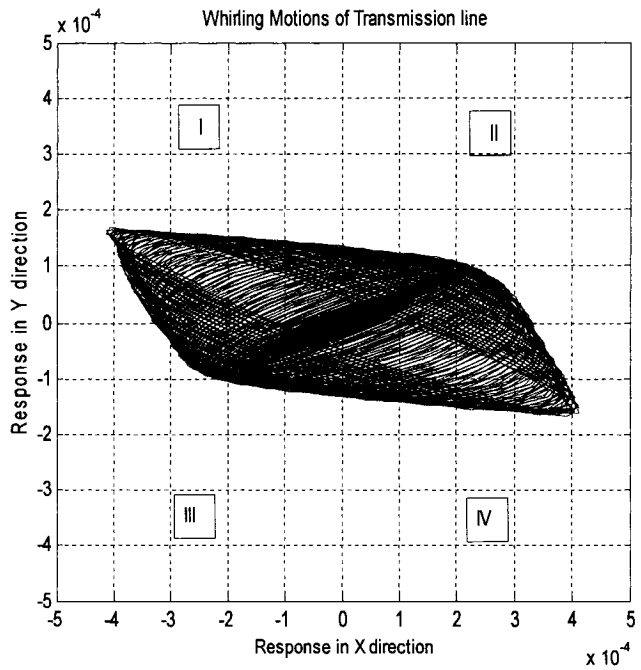

Fig 3.5.b: Whirl motions at U = 9.5 m/s; $\beta = 0°$; $\theta = 0°$; t = 25 seconds; X – Y responses in meters

3.3.1.4 At wind speed U = 15 m/s

The Lissajous figures are obtained for two different simulation times when the speed of the wind flow over the conductor is 15 m/s. These are shown in figures 3.6.a and 3.6.b for simulation times of 5 and 25 seconds, respectively.

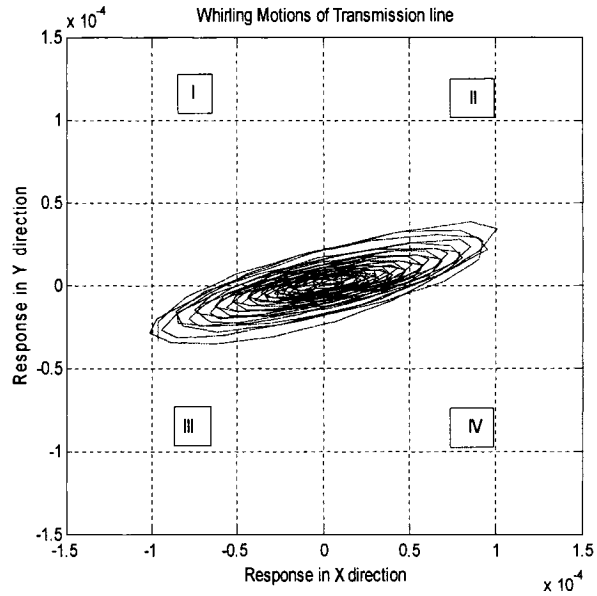

Fig 3.6.a: Whirl motions at U=15m/s; $\beta = 0°$; $\theta = 0°$; t = 5 seconds; X – Y responses in meters

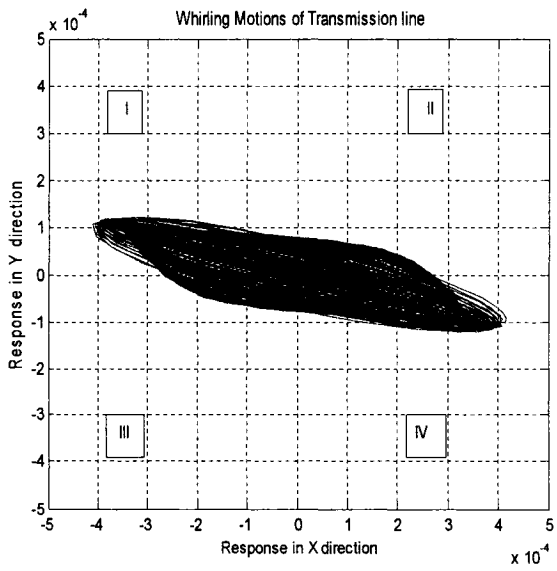

Fig 3.6.b: Whirl motions at U=15m/s; $\beta = 0°$; $\theta = 0°$; t = 25 seconds; X – Y responses in meters

3.3.2 When the angle of incidence of wind β = 30°

In the previous section, the direction of wind flow was horizontal. In this section, the Lissajous figures of the conductor orbital motion are obtained for an angle of incidence of wind β = 30° and for various simulation times. The figure 3.7 shows the schematic sketch of the conductor-ice model with wind acting at an angle of 30° on it.

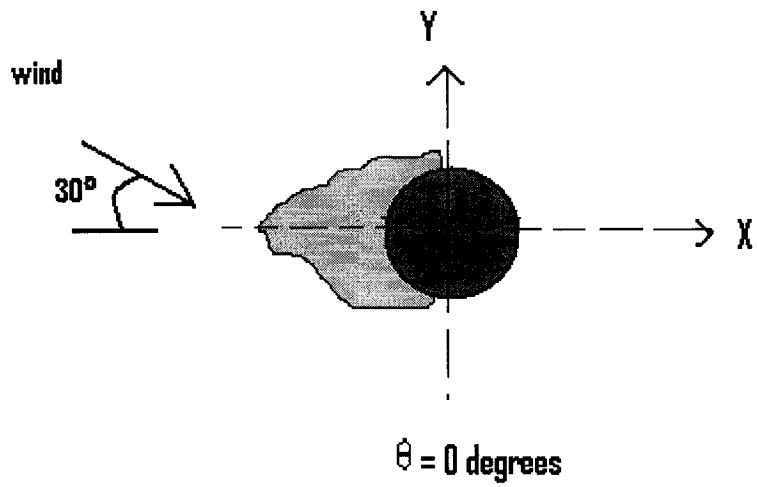

Fig 3.7: Sketch of conductor-ice model with wind at an angle β = 30°

3.3.2.1 At wind speed U = 5 m/s

The Lissajous figures of the conductor motions for two different simulation times are obtained when the speed of the wind flow is 5 m/s.

When the simulation is made to run for 5 seconds, the corresponding responses in X and Y directions over time 't' seconds is shown in the figure 3.8.a and the orbital motions obtained are shown in the figure 3.8.b.

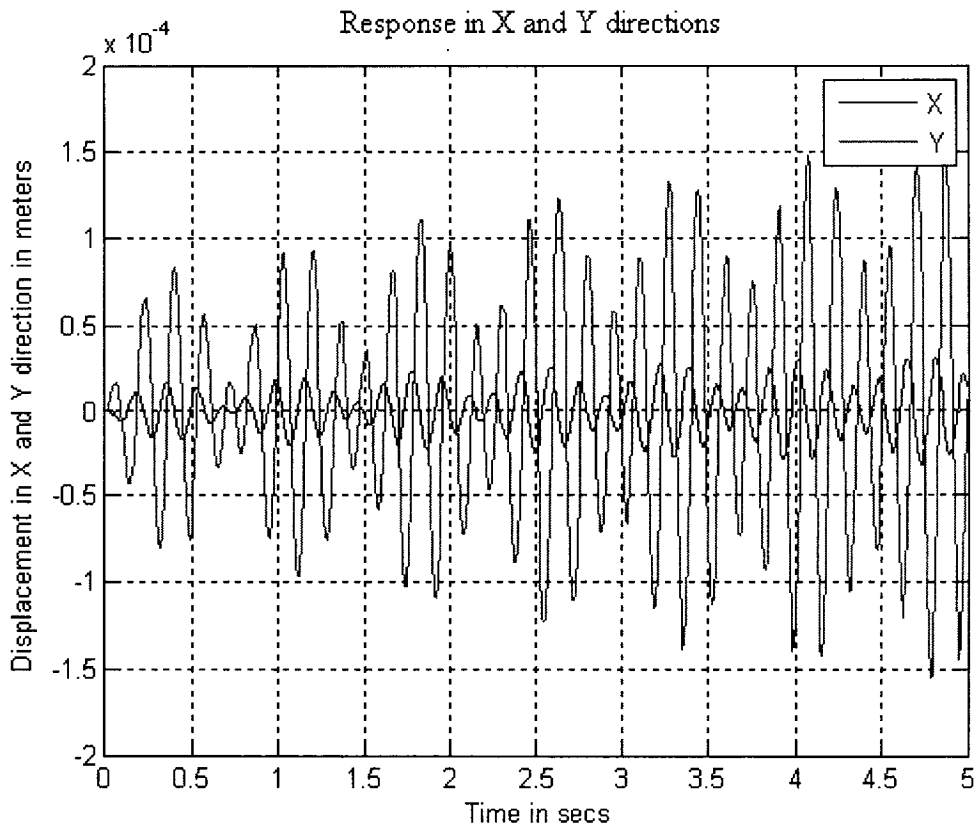

Fig 3.8.a: Responses in X and Y directions versus time't'

The Lissajous figure in this case shows elliptical orbits with major axes along Y with initial orientations along the quadrants I and IV as shown in the figure 3.8.b below.

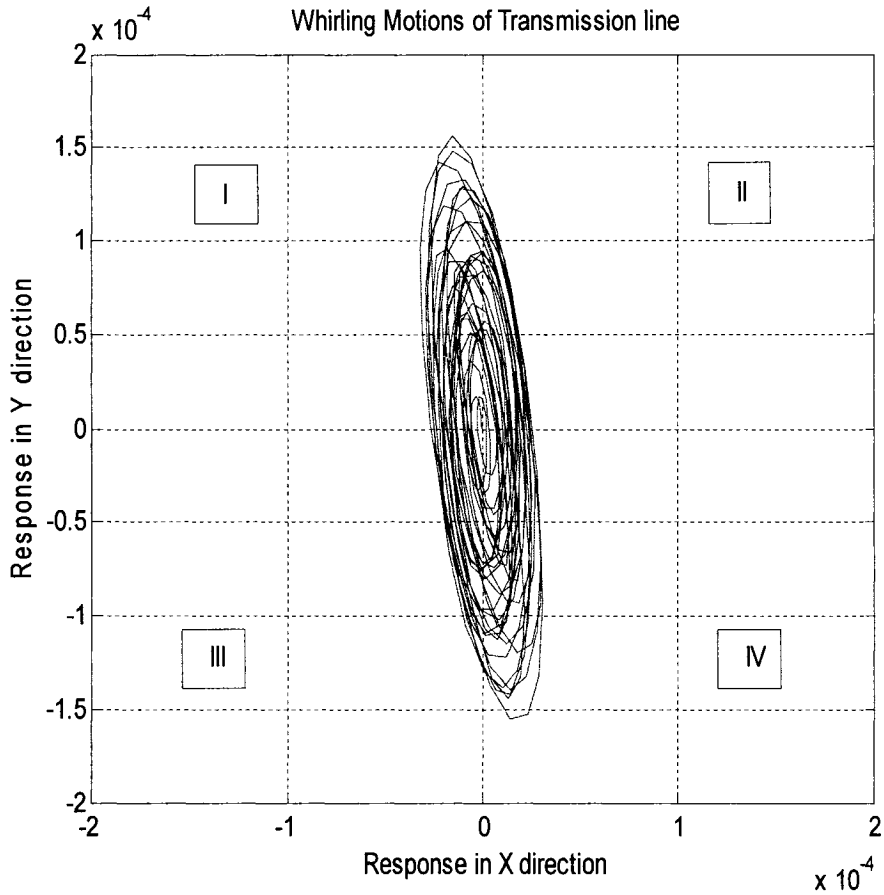

Fig 3.8.b: Whirl motions at U = 5m/s; $\beta = 30°$; $\theta = 0°$; t = 5 seconds; X – Y responses in meters

The Lissajous figure for a simulations time of 25 seconds is shown in the figure 3.8.c below. From the figure, it can be noticed that the orientation of the orbits changes from the quadrants I and IV to II and III.

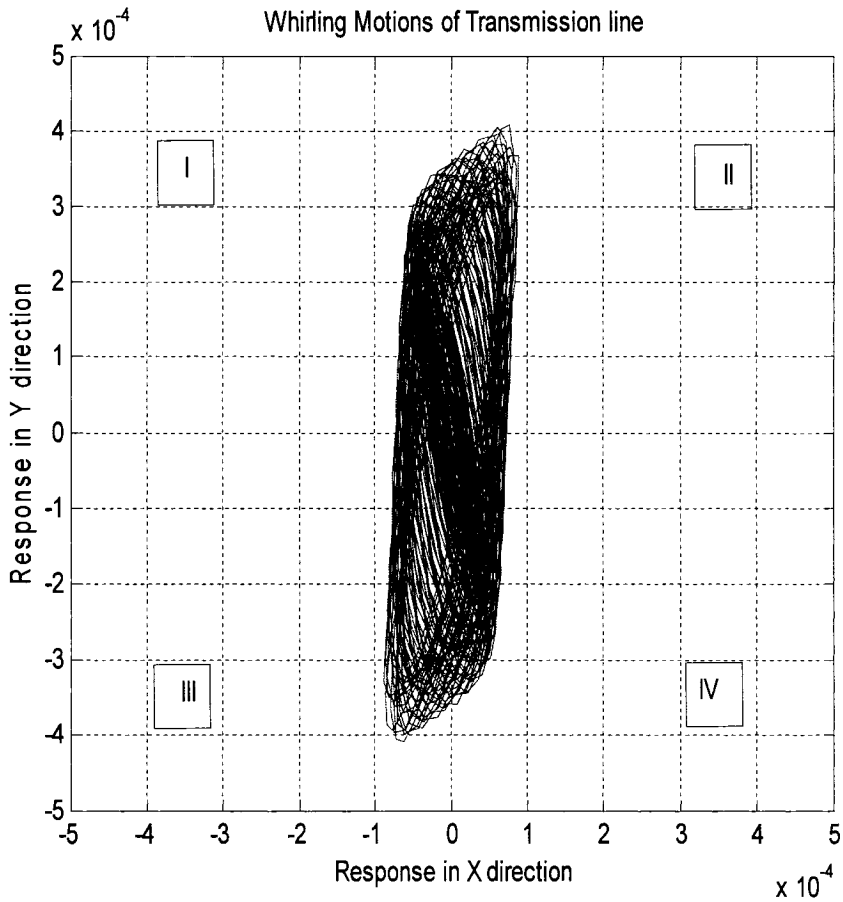

Fig 3.8.c: Whirl motions at U = 5m/s; $\beta = 30°$; $\theta = 0°$; t = 25 seconds; X – Y responses in meters

3.3.2.2 At wind speed U = 6.4 m/s

The Lissajous figures for the conductor motions are obtained in the similar manner as discussed in sections 3.3.1 and 3.3.2.1 above for two different simulation times when the wind flow is 6.4 m/s.

When the simulation time is 5 seconds, the Lissajous figure is shown in the figure 3.9.a.

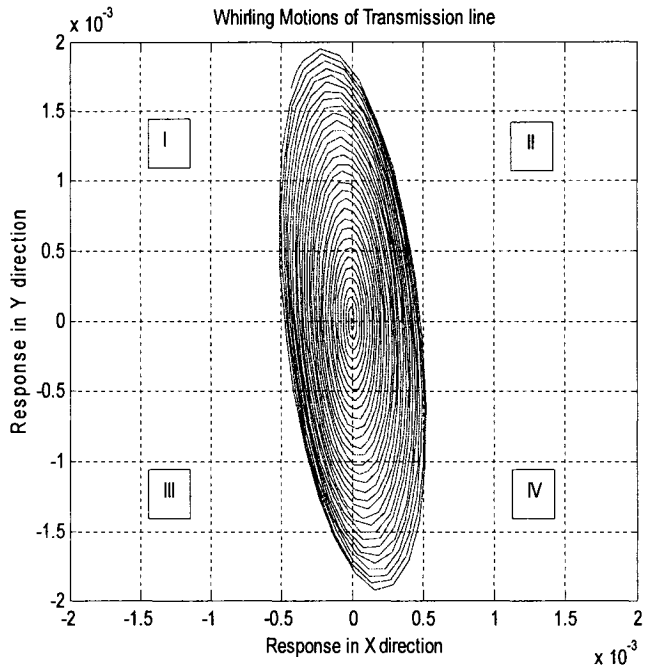

Fig 3.9.a: Whirl motions at U = 6.4m/s; $\beta = 30°$; $\theta = 0°$; t = 5 seconds; X – Y responses in meters

When the simulation time is 25 seconds, the Lissajous figure is shown in the figure 3.9.b.

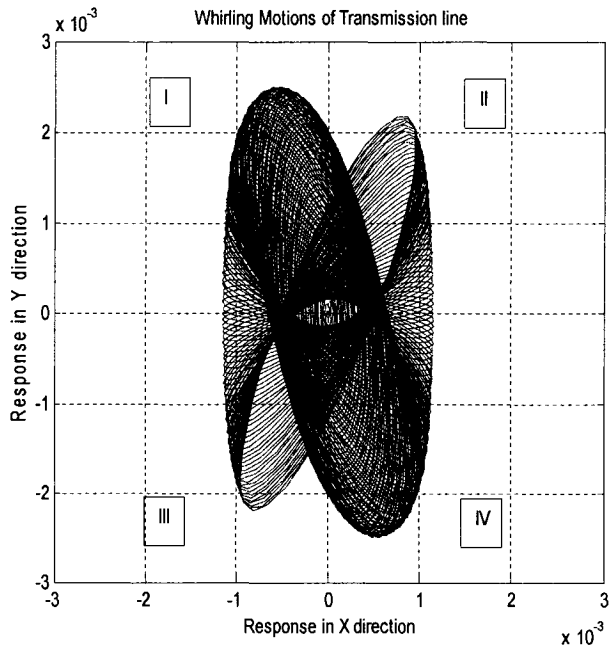

Fig 3.9.b: Whirl motions at U = 6.4m/s; $\beta = 30°$; $\theta = 0°$; t = 25 seconds; X – Y responses in meters

3.3.2.3 At wind speed U = 9.5 m/s

When the speed of the wind flow is 9.5 m/s, the Lissajous figure for simulation time of 5 and 25 seconds are shown in the figures 3.10.a and 3.10.b

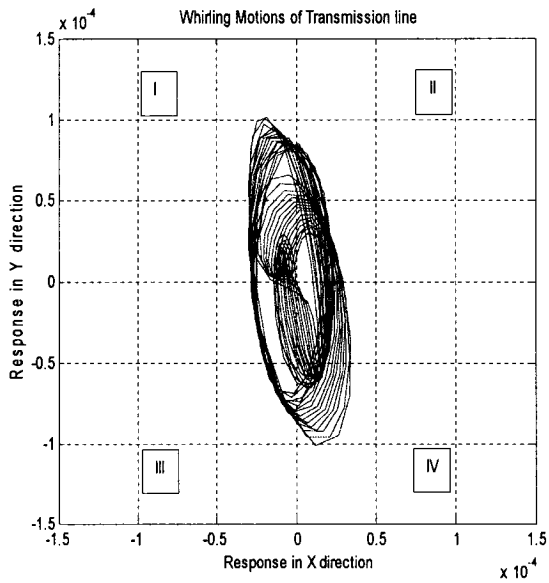

Fig 3.10.a: Whirl motions at U = 9.5m/s; β = 30°; θ = 0°; t = 5 seconds; X – Y responses in meters

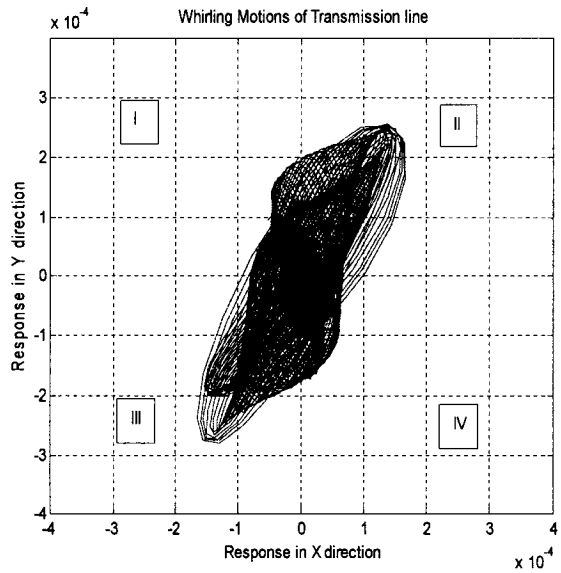

Fig 3.10.b: Whirl motions at U = 9.5m/s; β = 30°; θ = 0°; t = 25 seconds; X – Y responses in meters

3.3.2.4 At wind speed U = 15 m/s

When the speed of the wind flow is 15 m/s, the Lissajous figure for simulation time of 5 and 25 seconds are shown in the figures 3.11.a and 3.11.b

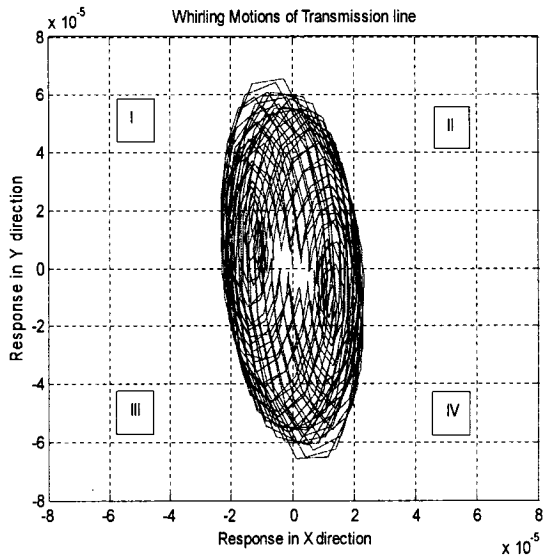

Fig 3.11.a: Whirl motions at U = 15m/s; $\beta = 30°$; $\theta = 0°$; t = 5 seconds; X – Y responses in meters

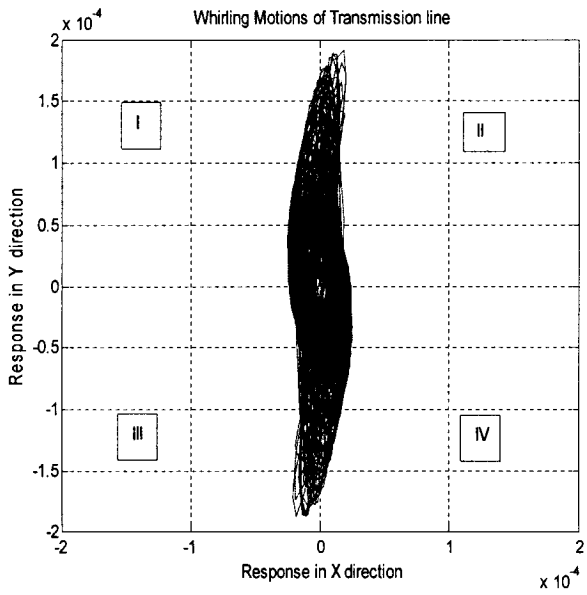

Fig 3.11.b: Whirl motions at U = 15m/s; $\beta = 30°$; $\theta = 0°$; t = 25 seconds; X – Y responses in meters

3.4 Orbital motions of transmission line when the angle of attack $\theta = 25°$

The responses of transmission line conductors and Lissajous figures were obtained for various angles of incidences of wind and simulation times. As mentioned earlier in chapter 2, the present work is based on Den Hartog's principle of galloping. The co-efficient of drag and lift forces are taken from O. Chabart's work [16] as shown in the figure 2.12. From figure 2.12, it can be noticed that maximum vibration occurs when the angle of attack ranges between 15 to 50 degrees.

3.4.1 When the angle of incidence of wind $\beta = 0°$

The figure 3.12 shows the schematic sketch of the conductor and ice model when the angle of attack is 25 degrees and angle of incidence of the wind on conductor is also 0 degrees. For every angle of incidence of wind β, orbital motions are found by varying the wind speed U from 5 m/s to 15 m/s.

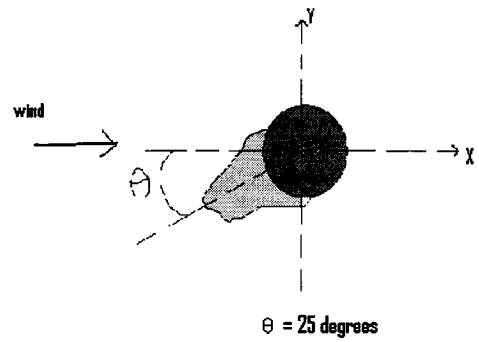

Fig 3.12: Sketch of conductor ice model at $\theta = 25°$ and $\beta = 0°$

3.4.1.1 At wind speed U = 5 m/s

The figure 3.13.b shows the Lissajous figure of the conductor-ice model when the wind flows over the conductor at 5 m/s. The simulation was initially made to run for 5 seconds. The responses in X and Y directions versus time't' are shown in figure 3.13.a.

The Responses in the figure 3.13.a shows a steady vibration response in X and increasing in Y. The maximum vibrations occurs in Y direction even when the angle of incidence was 0 degrees

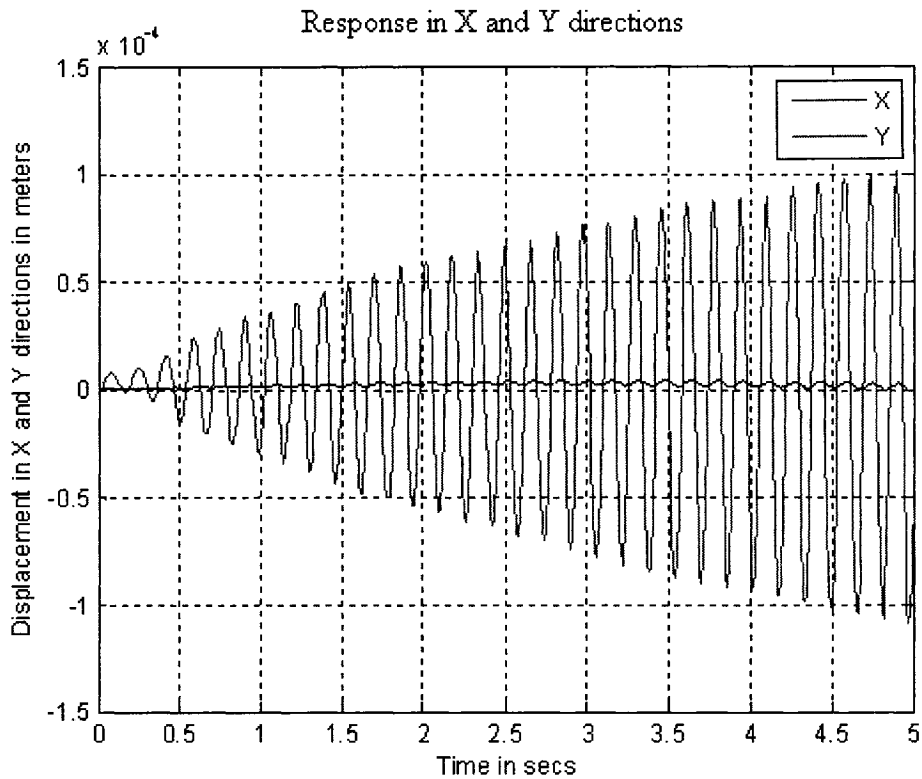

Fig 3.13.a: Responses of X and Y displacements over time't'

The Lissajous figure for a simulation time of 5 seconds is shown in the figure 3.13.b below. It can be noticed that the shape of the orbit is elliptical with major axes on Y and the orientation is the quadrants II and III.

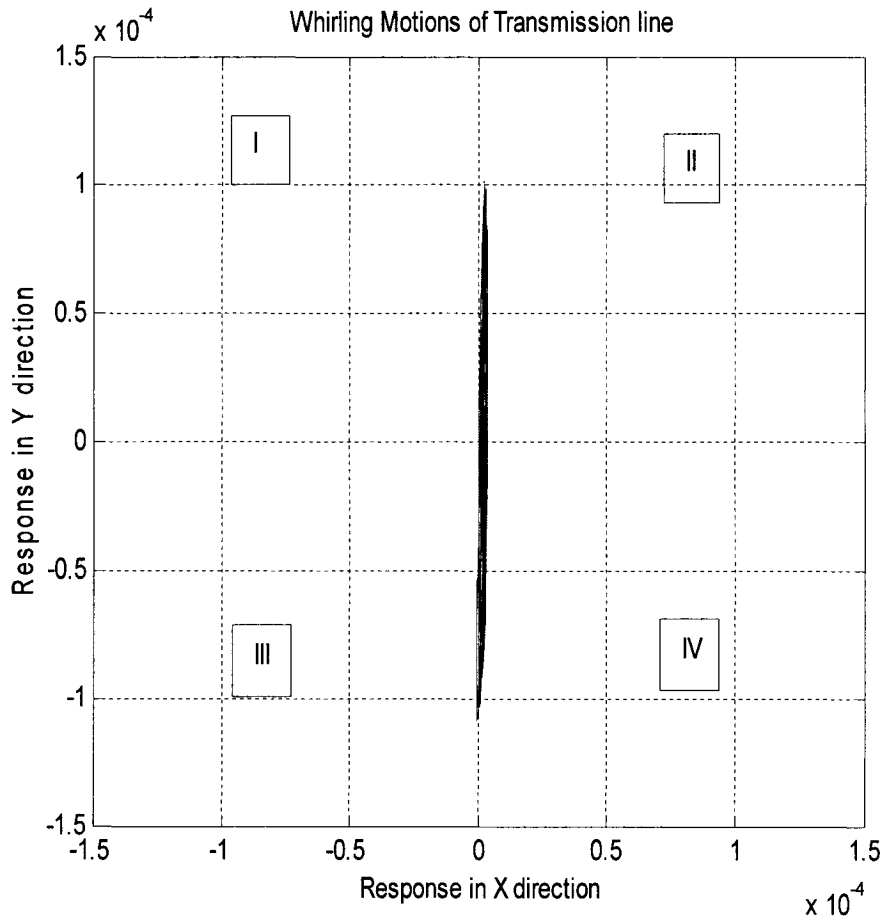

Fig 3.13.b: Whirl motions at U = 5m/s; $\beta = 0°$; $\theta = 25°$; t = 5 seconds; X – Y responses in meters

The Lissajous figure for the simulation time for 25 seconds is shown in the figure 3.13.c. The orientation of the orbits changes between the quadrants II and III to I and IV.

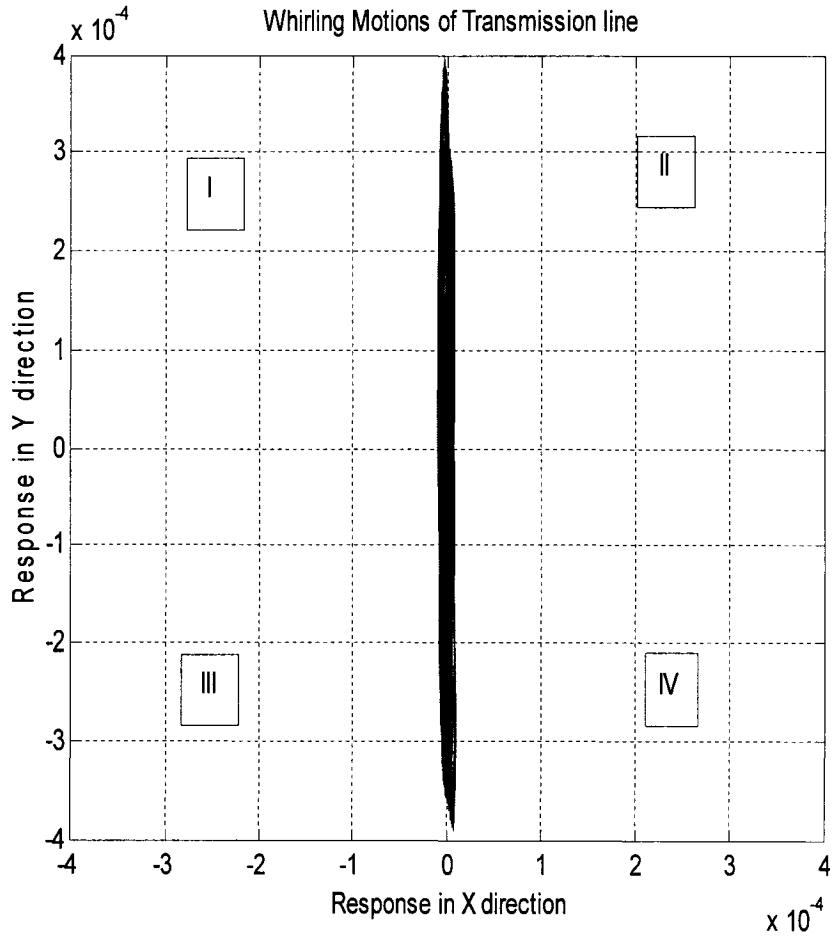

Fig 3.13.c: Whirl motions at U = 5m/s; $\beta = 0°$; $\theta = 25°$; t = 25 second; X – Y responses in meters

3.4.1.2 At wind speed U =6.4 m/s

In a similar manner, the Lissajous figures for a wind speed of 6.4 m/s are obtained for simulation time of 5 and 25 seconds, respectively, as shown in the figures 3.14.a and 3.14.b.

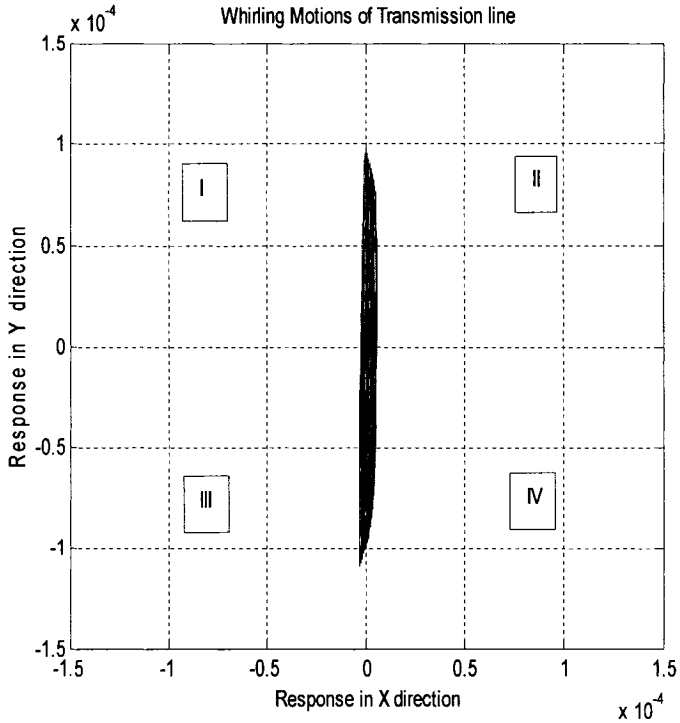

Fig 3.14.a: Whirl motions at U = 6.4m/s; $\beta = 0°$; $\theta = 25°$; t =5 seconds; X – Y responses in meters

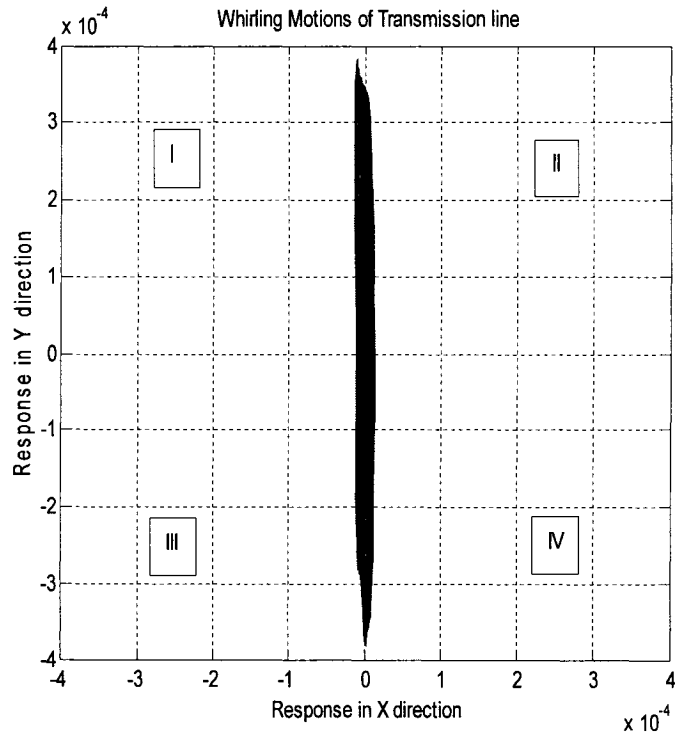

Fig 3.14.b: Whirl motions at U = 6.4m/s; $\beta = 0°$; $\theta = 25°$; t = 25 seconds; X – Y responses in meters

3.4.1.3 At wind speed U = 9.5 m/s

When the speed of the wind flow is 9.5 m/s, the Lissajous figure for simulation time of 5 and 25 seconds are shown in the figures 3.15.a and 3.15.b

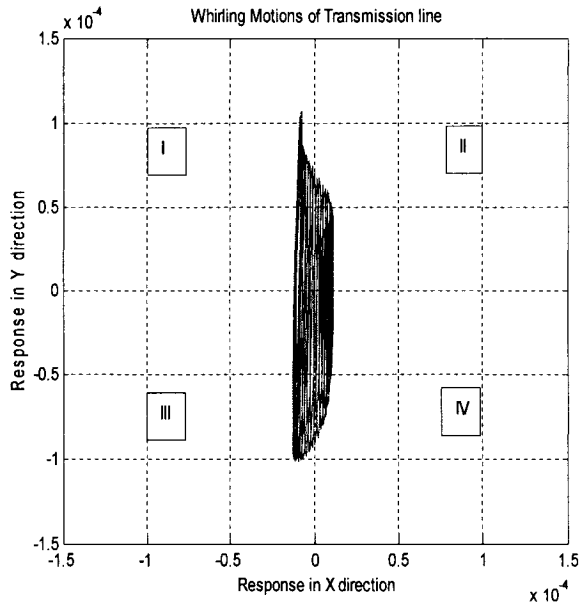

Fig 3.15.a: Whirl motions at U = 9.5m/s; β = 0°; θ = 25°; t = 5 seconds; X – Y responses in meters

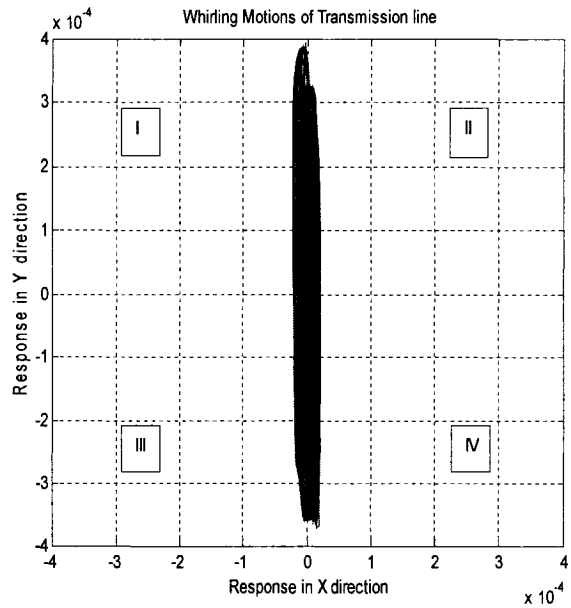

Fig 3.15.b: Whirl motions at U = 9.5m/s; β = 0°; θ = 25°; t = 25 seconds; X – Y responses in meters

3.4.1.4 At wind speed U = 15 m/s

When the speed of the wind flow is 15 m/s, the Lissajous figure for simulation time of 5 and 25 seconds are shown in the figures 3.16.a and 3.16.b

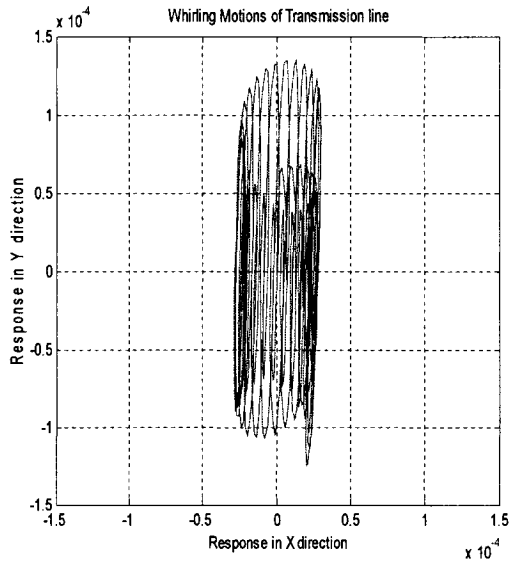

Fig 3.16.a: Whirl motions at U = 15m/s; β = 0°; θ = 25°; t = 5 seconds; X – Y responses in meters

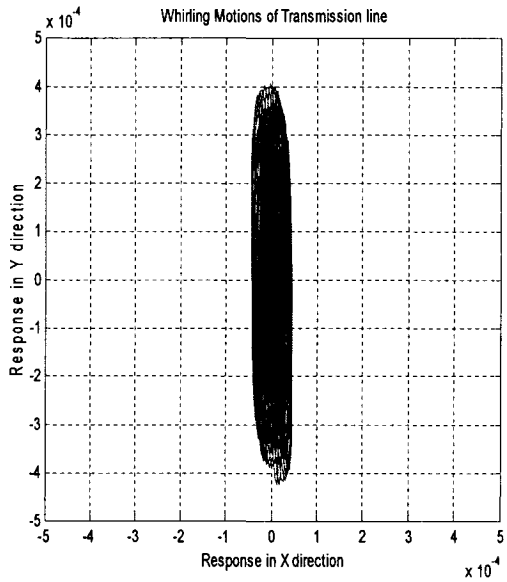

Fig 3.16.b: Whirl motions at U = 15m/s; β = 0°; θ = 25°; t = 25 seconds; X – Y responses in meters

3.4.2 When the angle of incidence of wind β = 30°

The Lissajous figures are obtained for various wind speeds when the angle of incidence of wind is 30 degrees.

3.4.2.3 At wind speed U = 5 m/s

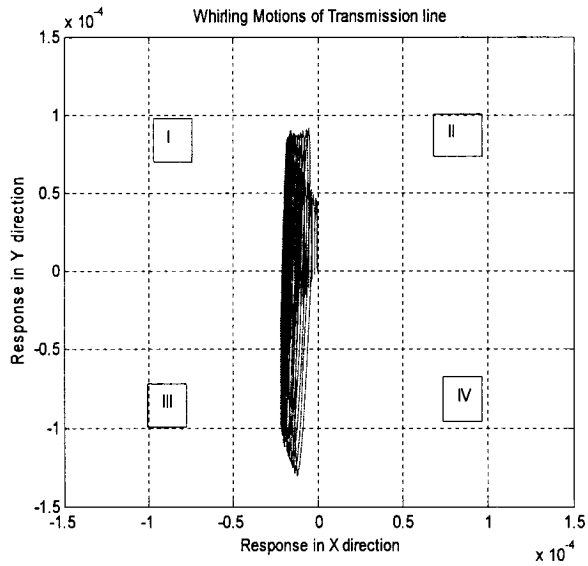

Fig 3.17.a: Whirl motions at U = 5m/s; β = 30°; θ = 25°; t = 5 seconds; X – Y responses in meters

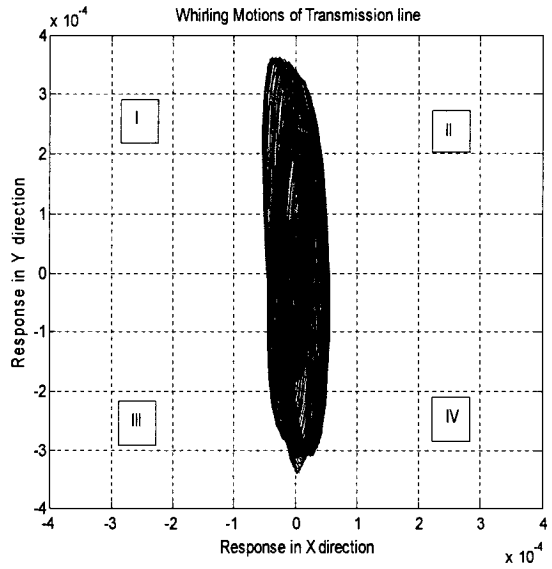

Fig 3.17.b: Whirl motions at U = 5m/s; β = 30°; θ = 25°; t = 25 seconds; X – Y responses in meters

3.4.2.4 At wind speed U = 15 m/s

The Lissajous figures for the wind speeds of 15 m/s are shown in the figure 3.18.a and 3.18.b.

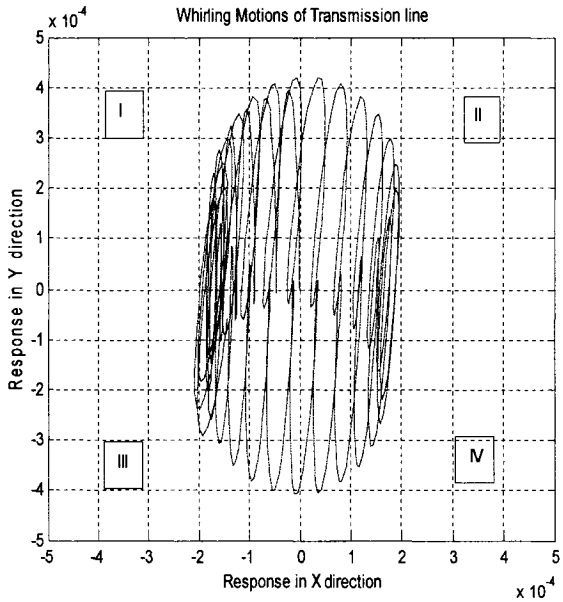

Fig 3.18.a: Whirl motions at U = 15m/s; β = 30°; θ = 25°; t=5 seconds; X – Y responses in meters

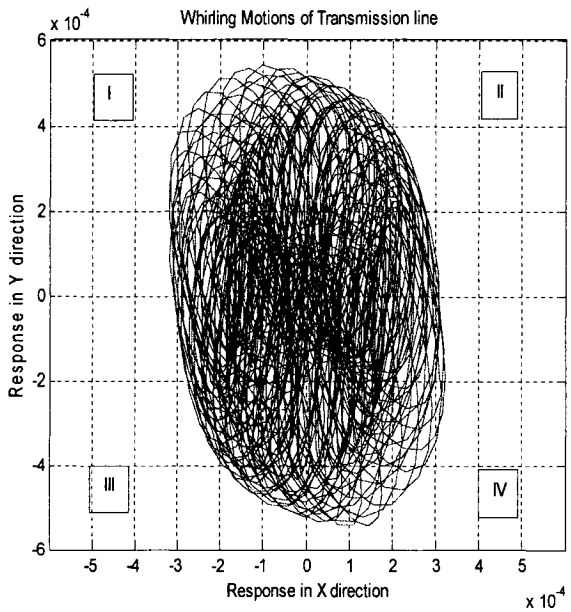

Fig 3.18.b: Whirl motions at U =15m/s; β = 30°; θ = 25°; t = 25 seconds; X – Y responses in meters

3.5 Orbital motions of transmission line when the angle of attack θ = 90°

The Lissajous figures for two different angles of incidences of the wind and for different simulations times were obtained.

3.5.1 When the angle of incidence of wind β = 0°

The figure 3.19 shows the schematic sketch of the conductor and ice model when the angle of attack is 90 degrees and angle of incidence of the wind on conductor is also 0 degrees. For every angle of incidence of wind β, orbital motions are found by varying the wind speed U from 5 m/s to 15 m/s.

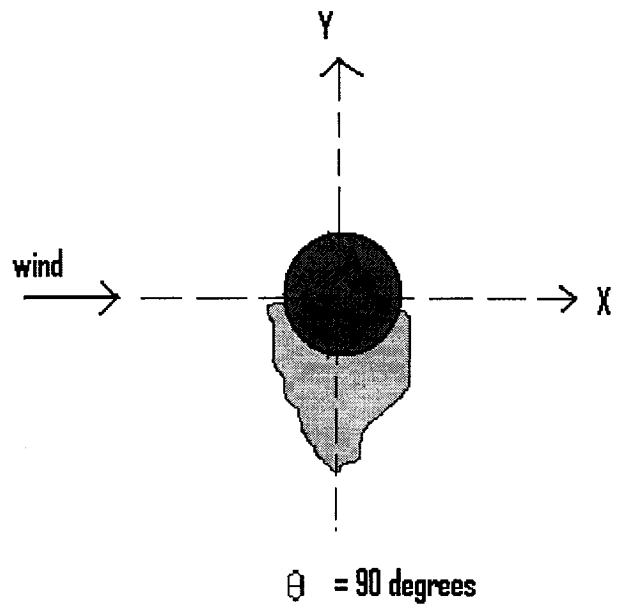

Fig 3.19: Sketch of conductor-ice model at θ = 90°and β = 0°

3.5.1.1 At wind speed U =5 m/s

The Lissajous figures for the simulation times of 5 and 25 seconds are shown in the figure 3.20.a and 3.20.b, respectively.

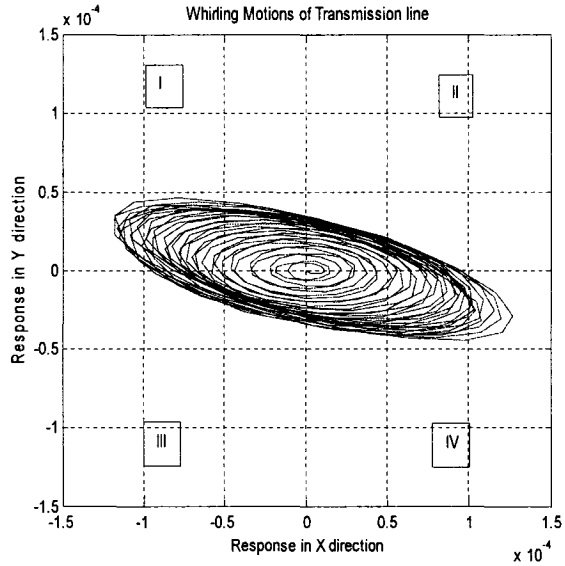

Fig 3.20.a: Whirl motions at U = 5m/s; β = 0°; θ = 90°; t = 5 seconds; X – Y responses in meters

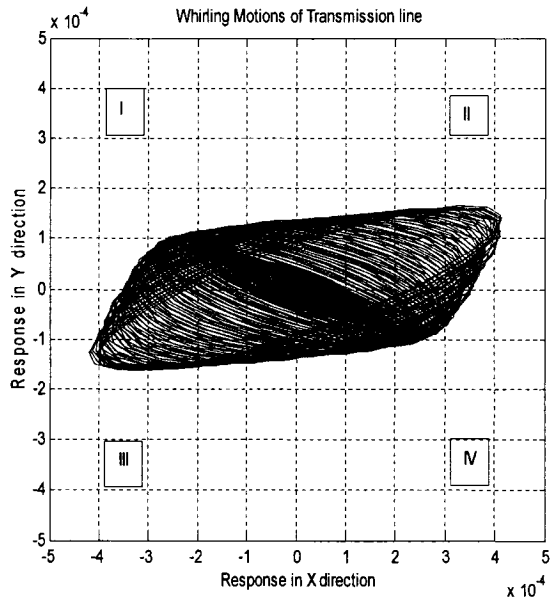

Fig 3.20.b: Whirl motions at U = 5m/s; β = 0°; θ = 90°; t = 25 seconds; X – Y responses in meters

3.5.1.2 At wind speed U =15 m/s

The Lissajous figures for the simulation times of 5 and 25 seconds are shown in the figure 3.21.a and 3.21.b, respectively

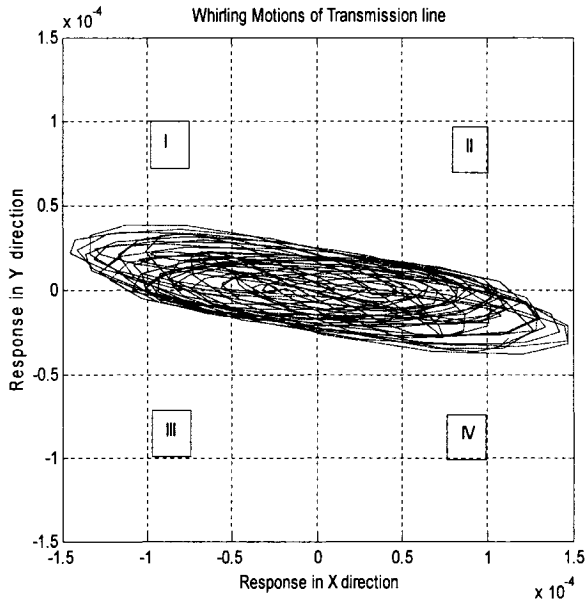

Fig 3.21.a: Whirl motions at U=15m/s; $\beta = 0°$; $\theta = 90°$; t = 5 seconds; X – Y responses in meters

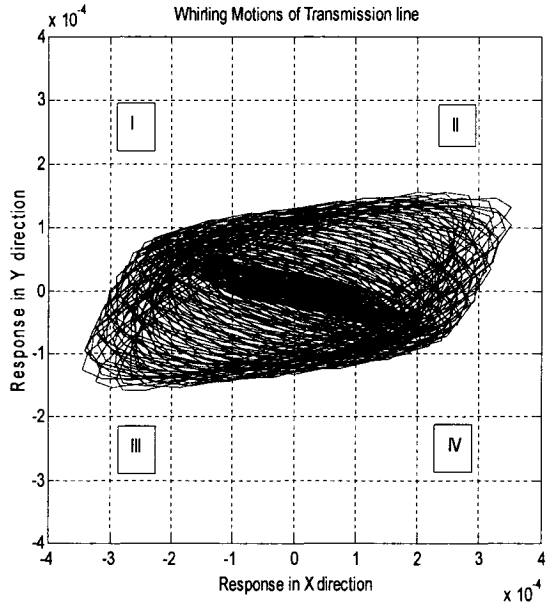

Fig 3.21.b: Whirl motions at U=15m/s; $\beta = 0°$; $\theta = 90°$; t = 25 seconds; X – Y responses in meters

3.5.2 When the angle of incidence of wind β = 30°

The Lissajous figures for two different wind speeds and at an angle of incidence of 30 degrees are obtained as shown in the figures below.

3.5.2.1 Wind speed: 5 m/sec

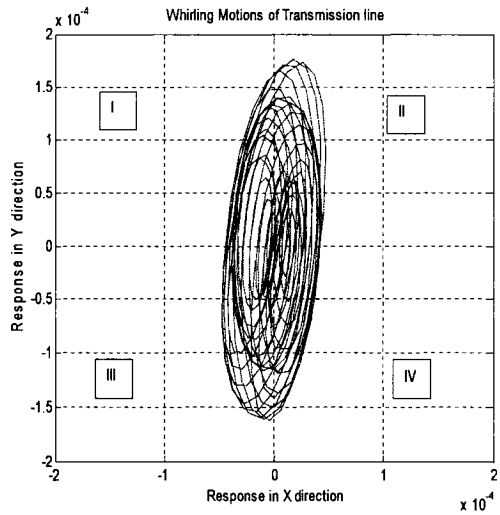

Fig 3.22.a: Whirl motions at U = 5m/sec; β = 30°; θ = 90°; t = 5 seconds; X – Y responses in meters

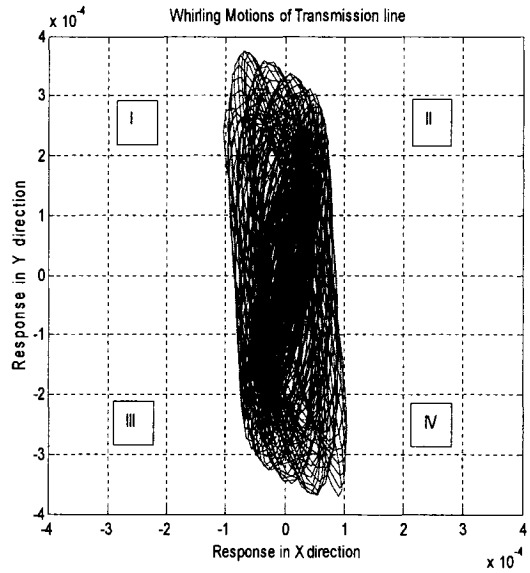

Fig 3.22.b: Whirl motions at U = 5m/sec; β = 30°; θ = 90°; t = 25 seconds; X – Y responses in meters

3.5.2.2 Wind speed: 15 m/sec

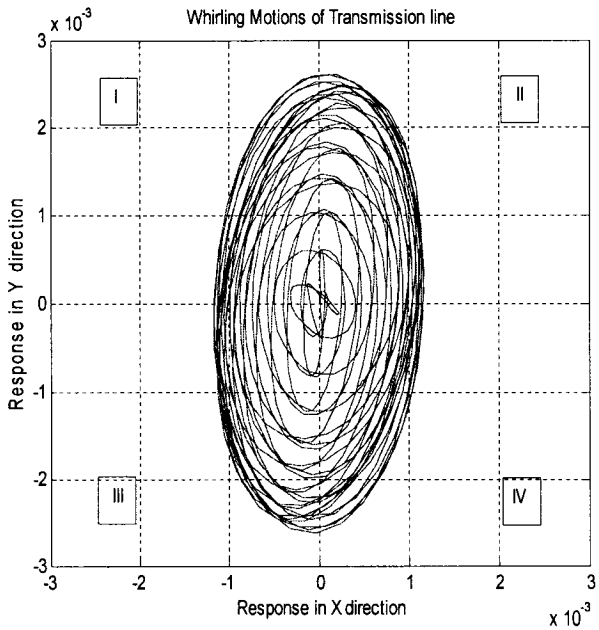

Fig 3.23.a: Whirl motions at U =15 m/sec; β = 30°; θ = 90°; t = 5 seconds; X – Y responses in meters

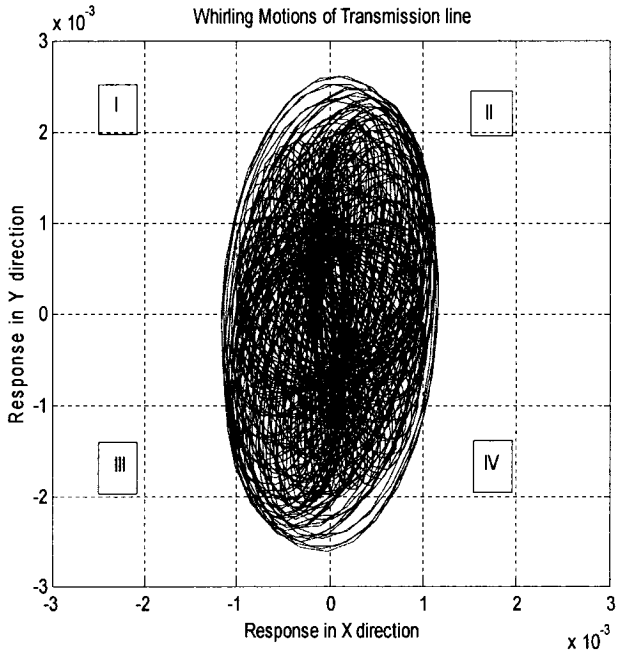

Fig 3.23.b: Whirl motions at U = 15 m/sec; β = 30°; θ = 90°; t = 20 seconds; X – Y responses in meters

3.6 Orbital motions of the transmission lines with the effect of structural damping

The equations of motion of the transmission line cable with aerodynamic and ice loads derived in chapter 2 are as follows:

In X-direction

$$\rho_m A_m \frac{\partial^2 x}{\partial t^2} - C_{X2}\dot{y} - 2\dot{x}C_{X3} + \rho_a A \dot{x}\dot{y}C_L - T\frac{\partial^2 x}{\partial s^2} = \frac{1}{2}\rho_a A U^2 C_{X1} \qquad \text{- (3.3)}$$

In Y-direction

$$\rho_m A_m \frac{\partial^2 y}{\partial t^2} - C_{Y2}\dot{y} + 2\dot{x}C_{Y3} + \rho_a A \dot{x}\dot{y}C_D - T\frac{\partial^2 y}{\partial s^2} - \rho_m A_m g - h(t) = \frac{1}{2}\rho_a A U^2 C_{Y1}$$

$$\text{- (3.4)}$$

Introducing structural damping in the system, the equations of motion of the transmission lines can be expressed as follows:

In X-direction

$$\rho_m A_m \frac{\partial^2 x}{\partial t^2} + C_{SX}\dot{x} - C_{X2}\dot{y} - 2\dot{x}C_{X3} + \rho_a A \dot{x}\dot{y}C_L - T\frac{\partial^2 x}{\partial s^2} = \frac{1}{2}\rho_a A U^2 C_{X1} \qquad \text{- (3.6)}$$

In Y-direction

$$\rho_m A_m \frac{\partial^2 y}{\partial t^2} + C_{SY}\dot{y} - C_{Y2}\dot{y} + 2\dot{x}C_{Y3} + \rho_a A \dot{x}\dot{y}C_D - T\frac{\partial^2 y}{\partial s^2} - \rho_m A_m g - h(t) = \frac{1}{2}\rho_a A U^2 C_{Y1}$$

$$\text{- (3.7)}$$

where C_{SX}, C_{SY} are the co-efficient of structural damping in X and Y directions.

3.6.1 When damping factor = 0.01, wind velocity U = 5m/s, angle of attack θ = 0° and angle of wind incidence β = 0°

The responses of transmission lines in X , Y directions and the orbital motions when the wind velocity is 5 m/s is shown in the figure 3.24.a 3.24.b and 3.24.c, respectively.

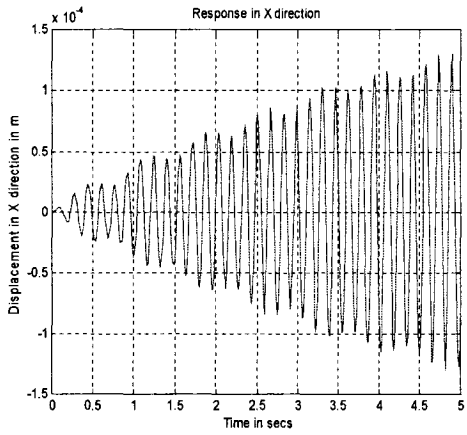

Fig 3.24.a: Response in X direction

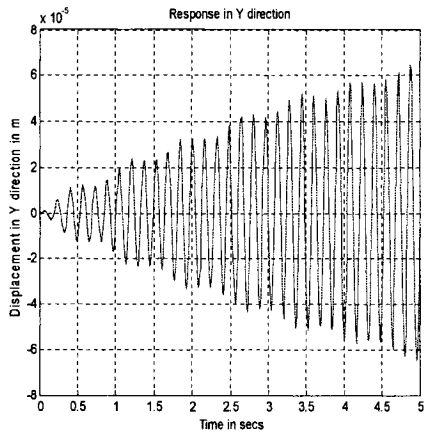

Fig 3.24.b: Response in Y direction

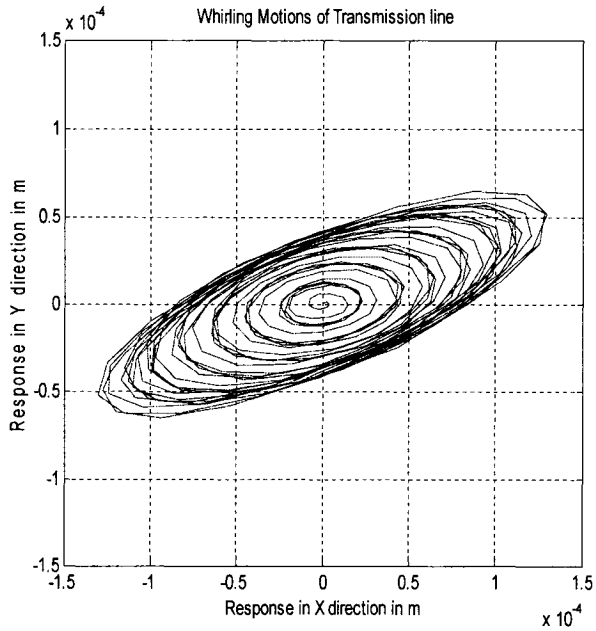

Fig 3.24.c: Orbital motions without damping when U = 5m/s, θ = 0°, β = 0°; X – Y responses in meters

From the figure 3.24.a and 3.24.b, it can be noticed that the maximum amplitudes reached in the 5 seconds of the simulation time were 0.128 mm in X direction and 0.065 mm in Y direction. When the structural damping factor in X and Y direction is considered to be 0.01, the responses in X, Y directions and the orbital motions are shown in the figure 3.25.a, 3.25.b and 3.25.c, respectively.

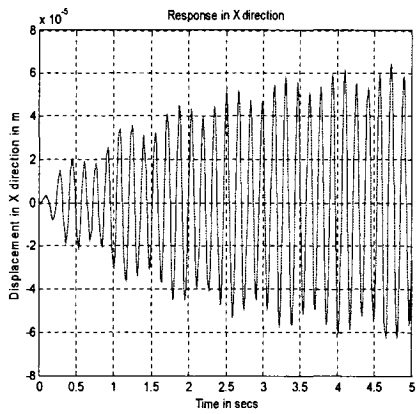

Fig 3.25.a: Response in X direction

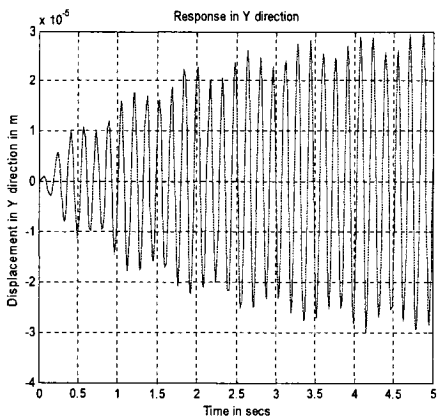

Fig 3.25.b: Response in Y direction

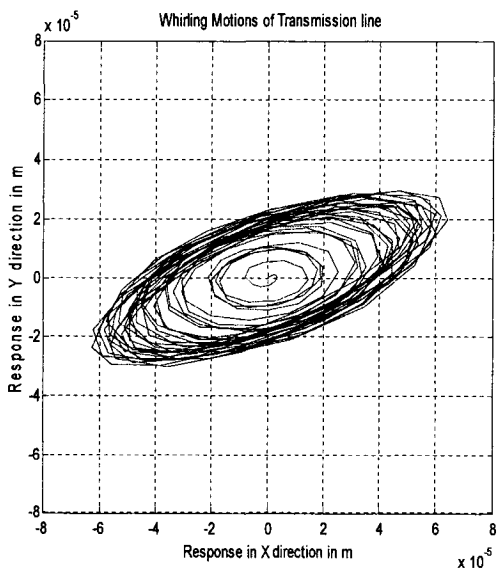

Fig 3.25.c: Orbital motions with damping factor = 0.01, U = 5m/s, $\theta = 0°$, $\beta = 0°$; X – Y responses in meters

From figure 3.25.a and 3.25.b, it can be noticed that the maximum amplitudes in X and Y directions reduces in the 5 seconds of the simulation time. The maximum amplitudes in X and Y direction in 5 seconds with damping factor of 0.01 were 0.065 mm and 0.03 mm respectively. The responses also shows the beginning of steadiness in X and Y directions.

3.6.2 When U =5m/s, angle of attack $\theta = 0°$, angle of wind incidence $\beta = 0°$ Damping factor = 0.05

When the structural damping factor in X and Y direction is considered to be 0.05, the responses in X, Y directions and the orbital motions are shown in the figure 3.26.a and 3.26.b, respectively.

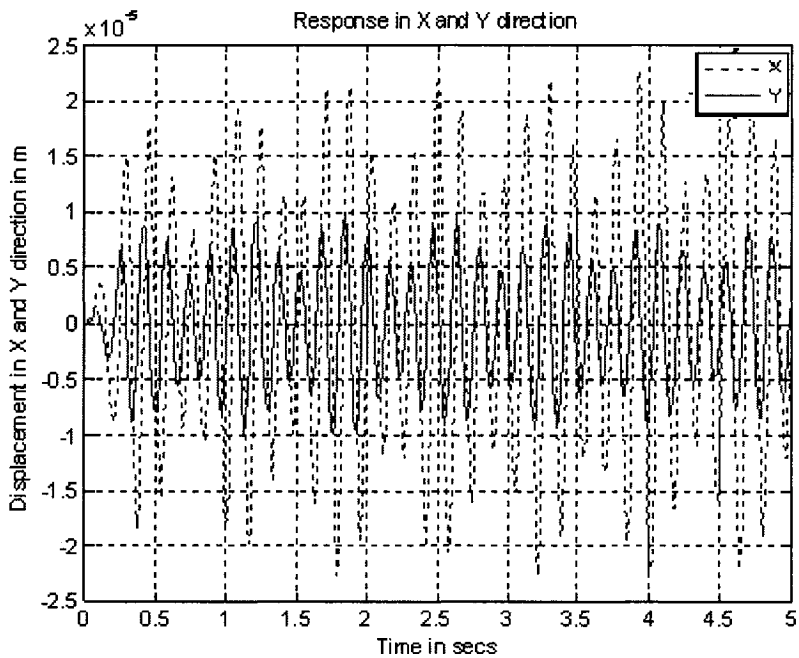

Fig 3.26.a: Response in X and Y directions over time't' secs

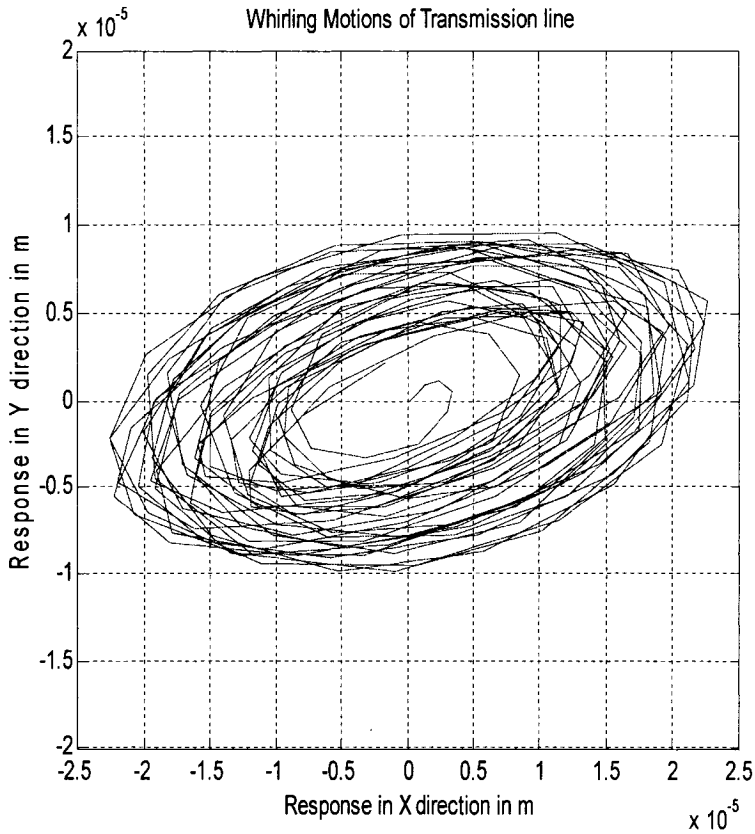

Fig 3.26.b: Orbital motions with damping factor = 0.05, U = 5m/s, $\theta = 0°$, $\beta = 0°$; X – Y responses in meters

From figure 3.26.a and 3.25.b, it can be noticed that at a damping factor of 0.05, the transmission line no longer exhibits self excited vibrations and steady state vibrations can be observed in X and Y directions. The maximum amplitudes in X and Y direction in 5 seconds with damping factor of 0.05 were 0.025 mm and 0.01 mm respectively.

3.6.3 With Damping U =5m/s, B =0, Theta = 0, Damping factor = 0.1

When the structural damping factor in X and Y direction is considered to be 0.1, the responses in X, Y directions and the orbital motions are shown in the figure 3.27.a, 3.27.b and 3.27.c, respectively.

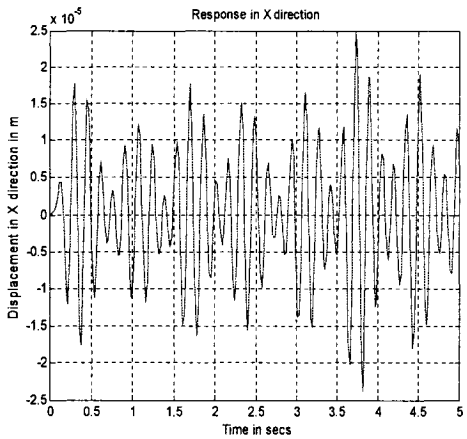

Fig 3.27.a: Response in X direction

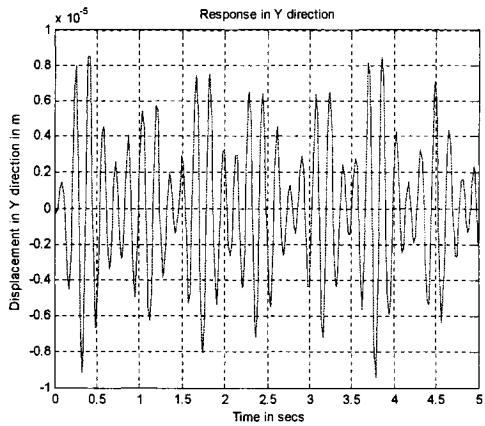

Fig 3.27.b: Response in Y direction

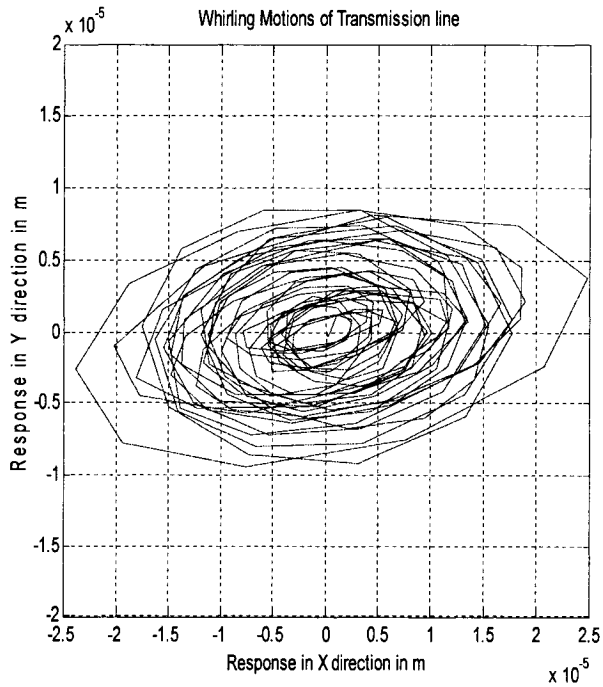

Fig 3.27.c: Orbital motions with damping factor = 0.1, U = 5m/s, θ = 0°, β = 0°; X – Y responses in meters

3.6.4 When damping factor = 0.05, wind velocity U = 5m/s, angle of attack θ = 0° and angle of wind incidence β = 30°

The responses of transmission lines in X and Y directions and the orbital motions when the wind velocity is 5 m/s and with no structural damping is shown in the figure 3.28.a and 3.28.b, respectively.

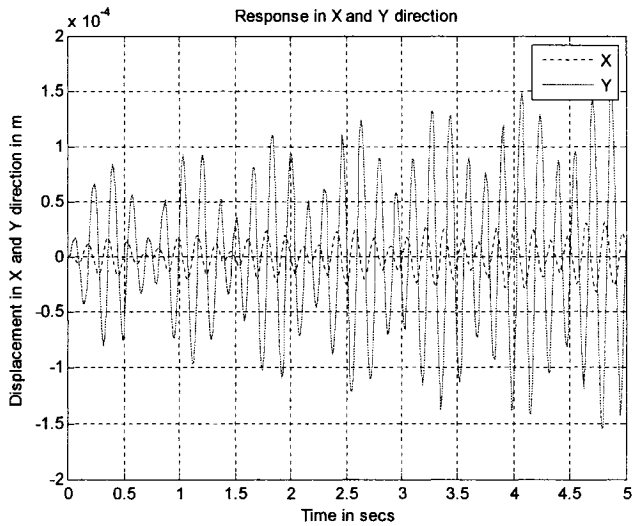

Fig 3.28.a: Response in X and Y directions over time't' secs

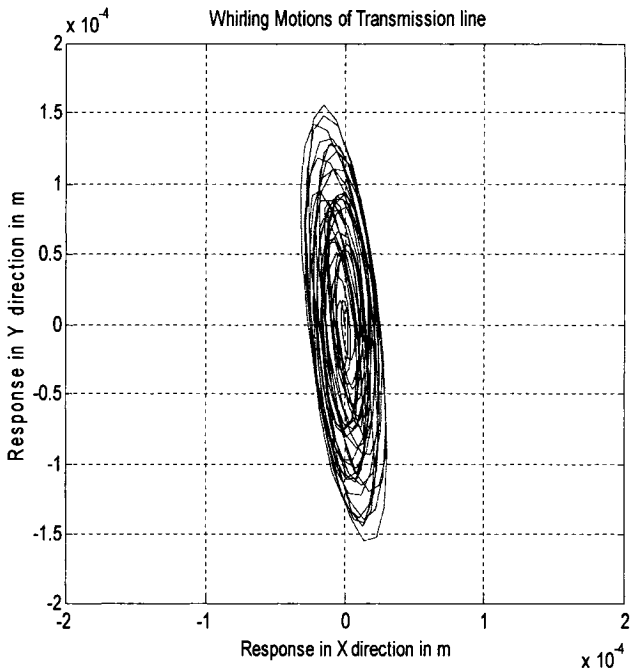

Fig 3.28.b: Orbital motions with no damping, U = 5m/s, θ = 0°, β = 30° ; X – Y responses in meters

From the figure 3.28.a and 3.28.b, it can be noticed that the system exhibits self excited vibrations with no structural damping. When the structural damping factor in X and Y direction is considered to be 0.05, the responses in X, Y directions and the orbital motions are shown in the figure 3.29.a and 3.29.b, respectively.

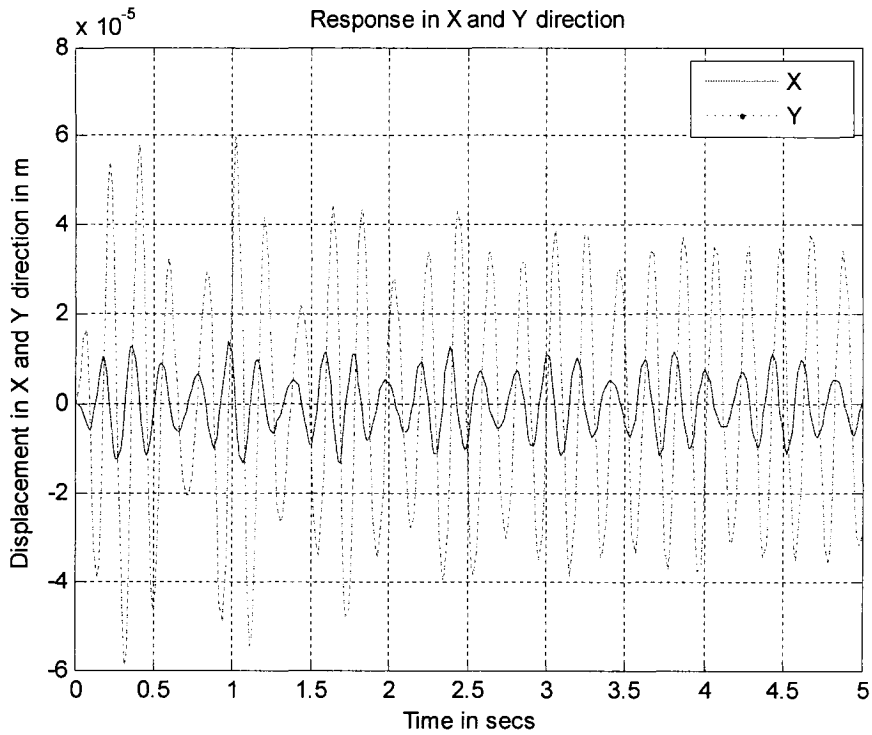

Fig 3.29.a: Response in X and Y directions over time't' secs

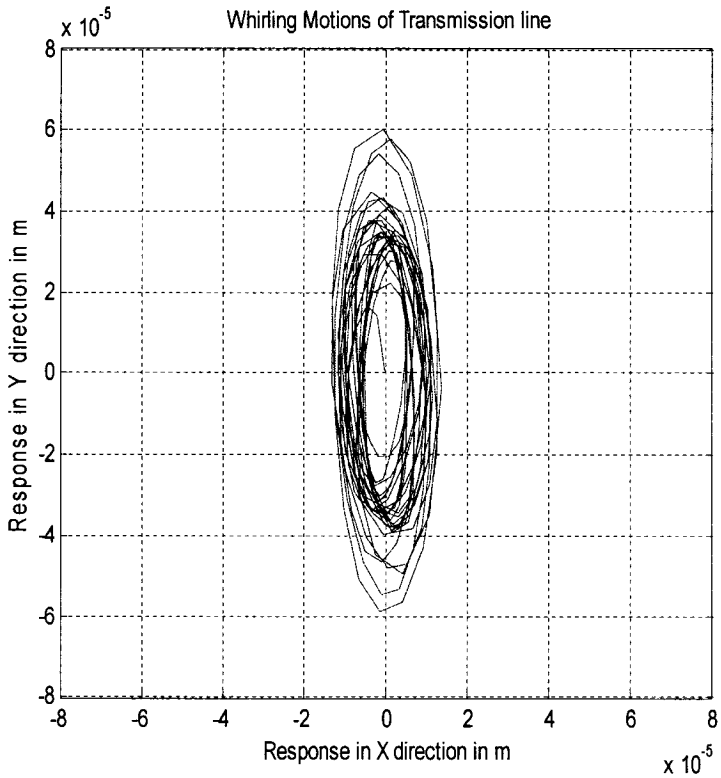

Fig 3.29.b: Orbital motions with a damping factor = 0.05, U = 5m/s, $\theta = 0°$, $\beta = 30°$; X – Y responses in meters

From figure 3.29.a and 3.29.b, it can be noticed that at a damping factor of 0.05, the transmission line exhibits steady state vibrations in X and Y directions.

3.6.5 When damping factor = 0.1, U = 5m/s, B = 30°, θ = 0°

When the structural damping factor in X and Y direction is considered to be 0.1, the responses in X, Y directions and the orbital motions are shown in the figure 3.30.a, 3.30.b and 3.30.c, respectively.

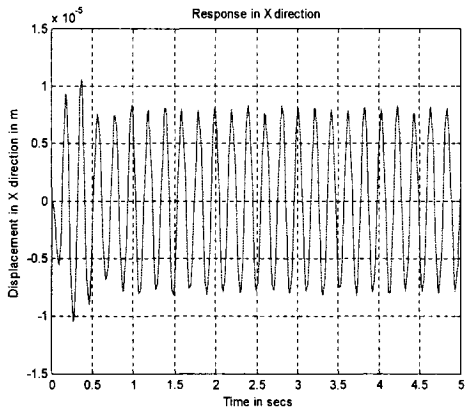

Fig 3.30.a: Response in X direction

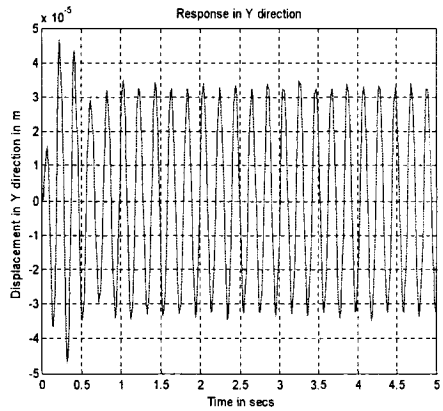

Fig 3.30.b: Response in Y direction

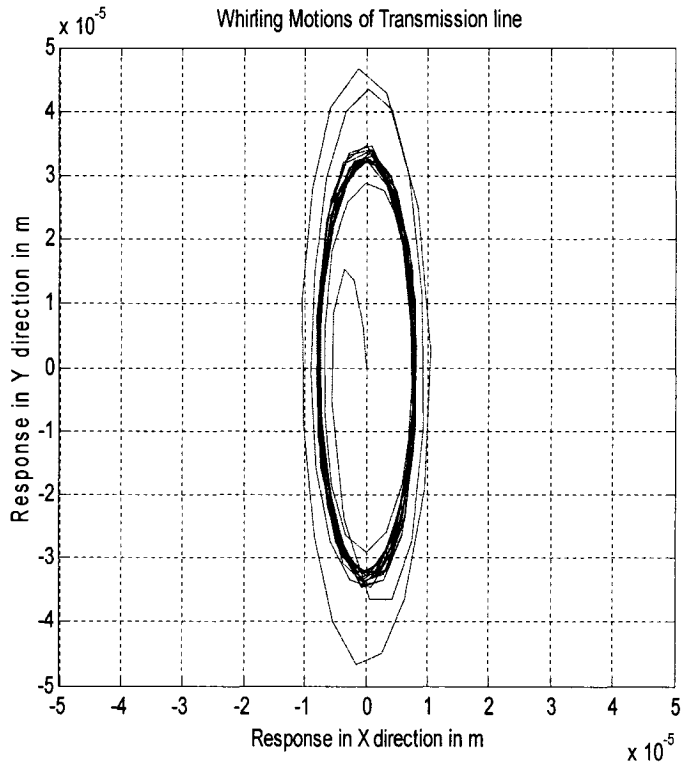

Fig 3.30.c: Orbital motions with a damping factor = 0.1, U = 5m/s, $\theta = 0°$, $\beta = 30°$;
X – Y responses in meters

3.7 Summary

In this chapter, the equations of motions of the transmission line cables as obtained from chapter 2 were solved using fourth order Runge - Kutta Method in MATLAB and the results were simulated for various wind speed, angles of attack and angles of incidence of the wind on the cable. From the results we see that when the angle of incidence of wind on cable is 0°, the shape of the orbit is elliptical with major axis on X- axis. Similarly when the angle of incidence was more than 0° (30° as assumed in this work) , the shape is elliptical with major axis on Y- axis. The co-efficient of drag and lift forces values were taken from the previous work done by Chabart [16] as mentioned in chapter 2. These values are not taken into consideration when the whirling motions of the cables are studied experimentally in the wind tunnel. The responses of transmission lines with the effect of structural damping were also studied. In the next chapter, the principle of scale modeling is explained briefly and is employed in order to obtain the dimensions of the actual and scaled cable models to be tested in a wind tunnel. The experimental set-up and results would be discussed in chapter 5.

CHAPTER 4

SCALE MODELLING OF TRANSMISSION LINES CABLES

4.1 General

In the previous chapter, response of transmission line cable under the action of various wind velocities and angles of attack were studied. In the present chapter experimental investigations are performed on the cable at different wind speeds and angles of attack in a wind tunnel. Figure 4.1 below shows the test section of the wind tunnel.

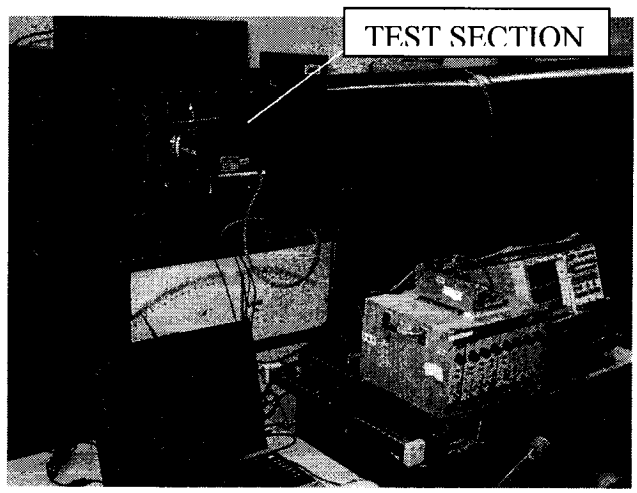

Fig 4.1: Test section of the wind tunnel

The test section of the wind tunnel shown above in the figure 4.1 is 0.5 meters long along the direction of the wind, has a breadth of 0.34 meters perpendicular to the direction of wind and has a height of 0.25 meters. The models to be tested are kept perpendicular to the direction of the wind flow. Thus it is clear that the entire cable section of length 142 meters cannot be tested in the test section of the wind tunnel. Due to this restriction, the concept of scale modeling is employed.

The model is based on the fact that the model and prototype systems obey the same physical laws. The model is constructed so as to embody all the relevant features and parts of the prototype system. This relationship between the model and the prototype is referred to as similarity. This similitude theory is employed to develop the necessary similarity conditions or known as scaling laws for dynamic testing of the scaled models. Scaling laws provide relationship between a full-scale structure and its small scale model, and can be used to predict the response of the prototype by performing dynamic testing on the models in the wind tunnel.

4.2 Dimensional analysis

Dimensional analysis is a procedure by which the above mentioned condition of similarity is achieved. This procedure is based on the fact that all general relationships in physics and engineering are expressed by dimensionally homogenous equations [21].

4.2.1 Primary and secondary quantities in dimensional analysis

Any physical situation can be described by certain familiar physical quantities, for example length, velocity, area, volume, acceleration etc. These are all known as **dimensions** [21]. The dimensions are, however, of no use without a magnitude being attached. Dimensions are properties which can be measured. Units are the standard elements used to quantify these dimensions. In dimensional analysis only the nature of the dimensions is of concern, i.e. its quality and not its quantity. Only three physical quantities: Mass, Length and Time are required to define both dimensions and quantity in Mechanics, and these quantities in mechanics are defined as **basic quantities** [21]. In general, the symbols used for the basic quantities such as length, mass, time, temperature and current are L, M, T, θ and I, respectively. These quantities are known as **primary quantities**, whereas quantities such as velocity, acceleration and force which can be expressed in terms of these basic quantities are known as **secondary quantities** [21].

4.2.2 Principle of scale modeling, representative quantity and concept of 'pi' numbers

The scale modeling is achieved by considering small elements of the prototype and their corresponding elements in the model. The homologous behavior of corresponding model elements is secured if each quantity of prototype can be transformed into the corresponding quantity of the model elements through

multiplication by a respective constant factor called **scale factor** [21]. The similarity condition expresses linearity between the corresponding variables of the prototype and the model which can be defined by a constant of proportionality, named scale factor Δ, which is the ratio

$$\Delta_j = \frac{Magnitude\ of\ j^{th}\ \text{var}iable\ in\ prototype}{Magnitude\ of\ j^{th}\ \text{var}iable\ in\ \text{mod}el}$$

where Δ_j is the scaling factor corresponding to the j^{th} physical quantity. Thus this shows that the ratio of the corresponding dimensional variables of prototype and model at corresponding points are constants. For instance length scale factor can be defined as

$$\Delta_l = \frac{l_p(prototype)}{l_m(\text{mod}el)} = \text{constant}$$

Similarly scale factor for time, velocity, mass etc can also be found out.

There are basically three similarity classifications in scale modeling [21]:

1. **Geometric similarity**: All linear dimensions of the model are related to the corresponding dimensions of the prototype by a constant length scale factor Δ_l
2. **Kinematic similarity**: The velocities at 'corresponding' points on the model and prototype are in the same direction and differ by a constant velocity scale factor Δ_v
3. **Dynamic similarity**: This is basically met if model and prototype forces differ by a constant scale factor at similar points.

In practice, modeling becomes difficult as every element of reduced or enlarged model must repeat every element of prototype on different but constant primary scales. For instance $\Delta_l = \frac{l_p}{l_m}$ indicates that any corresponding lengths, distance, deformations, or displacement of model and prototype must obey the same length scale factor. The quantities like l_p, l_m, v_p, v_m that are involved in the study of prototype and models are called **representative quantities** [21] and they are very important in scale modeling. Any scale factor can be expressed in terms of representative quantities. For example, the velocity scale factor can be expressed as

$$\Delta_v = \frac{\Delta_l}{\Delta_t} \text{ and this can be expressed as } \frac{v_p}{v_m} = \frac{l_p}{l_m}\frac{t_m}{t_p}$$

The above relationship can be written as

$$\frac{v_p t_p}{l_p} = \frac{v_m t_m}{l_m}$$

with all representative quantities of the prototype transferred to one side and the corresponding representative quantities of the model to other. These dimensionless products play an important role in scale modeling and they are called '**pi-numbers**' and are denoted by the Greek letter '**π**'. A pi-number is a pure number without any physical unit. Such a number is typically defined as a product or ratio of quantities that have units, in such a way that the product itself is dimensionless.

4.3 Derivation of scale factors for transmission line cables using dimensional analysis

In chapter 2, the equations of motions of transmission lines cables were derived. From the equations of motions, the relevant variables necessary to describe the cable motions and their basic dimensions are written in the tabular column as follows:

Symbol	Measured Quantity	Dimensions
l	Characteristic Length	L
ρ	Characteristic Density	ML^{-3}
F	Characteristic Force	MLT^{-2}
E	Modulus of Elasticity	$ML^{-1}T^{-2}$
M	Mass per unit length	ML^{-1}
t	Characteristic time	T
g	Acceleration due to gravity	LT^{-2}
U	Velocity of air	LT^{-1}
A	Characteristic area	L^2
ω	Frequency	T^{-1}

Table 4.1: Variables and their dimensions

By the principle of dimensional analysis, the first step is to form the product of the variables

$$(l)^{x_1}(\rho)^{x_2}(F)^{x_3}(E)^{x_4}(M)^{x_5}(t)^{x_6}(g)^{x_7}(U)^{x_8}(A)^{x_9}(\omega)^{x_{10}} \quad \text{- (4.1)}$$

where x_i are integers to which the powers of the variables are raised. Substituting the basics dimensions for each of the variables above in (4.1), we have

$$(L)^{x_1}(ML^{-3})^{x_2}(MLT^{-2})^{x_3}(ML^{-1}T^{-2})^{x_4}(ML^{-1})^{x_5}(T)^{x_6}(LT^{-2})^{x_7}(LT^{-1})^{x_8}(L^2)^{x_9}(T^{-1})^{x_{10}} \quad \text{- (4.2)}$$

Equating the basic dimensions [M, L, and T] in (4.2) to zero, we have

$$M: 0 + x_2 + x_3 + x_4 + x_5 + 0 + 0 + 0 + 0 + 0 = 0 \quad \text{- (4.3)}$$

$$L: x_1 - 3x_2 + x_3 - x_4 - x_5 + 0 + x_7 + x_8 + 2x_9 + 0 = 0 \quad \text{- (4.4)}$$

$$T: 0 + 0 - 2x_3 - 2x_4 + 0 + x_6 - 2x_7 - x_8 + 0 - x_{10} = 0 \quad \text{- (4.5)}$$

From 4.3, 4.4 and 4.5 the dimensional matrix can be formed as follows:

	l	ρ	F	E	M	t	g	U	A	ω
M	0	1	1	1	1	0	0	0	0	0
L	1	−3	1	−1	−1	0	1	1	2	0
T	0	0	−2	−2	0	1	−2	−1	0	−1
	x_1	x_2	x_3	x_4	x_5	x_6	x_7	x_8	x_9	x_{10}

Consider the determinant formed by first three column of the above matrix

$$\begin{array}{cccc} & l & \rho & F \\ M & 0 & 1 & 1 \\ L & 1 & -3 & 1 \\ T & 0 & 0 & -2 \end{array}$$

Since the determinant of the above matrix is nonzero the rank of the dimensional matrix is 3 and according to Buckingham's pi theorem there are 10-3=7 dimensionless products required for this model.

Hence in order to find the suitable sets of pi numbers, let us choose 3 parameters x_1, x_5 *and* x_6 and express them in terms of $x_2, x_3, x_4, x_7, x_8, x_9$ *and* x_{10}.

Looking at the dimensional matrix, we have

$$x_5 = -x_2 - x_3 - x_4 \qquad \text{- (4.6)}$$

$$x_1 = 3x_2 - x_3 + x_4 - x_5 - x_7 - x_8 - 2x_9 = 2x_2 - 2x_3 - x_7 - x_8 - 2x_9 \qquad \text{- (4.7)}$$

$$x_6 = 2x_3 + 2x_4 + 2x_7 + x_8 + x_{10} \qquad \text{- (4.8)}$$

Substituting the values of x_1, x_5, x_6 obtained from (4.6), (4.7) and (4.8) in (4.1), we have

$$(l)^{(2x_2-2x_3-x_7-x_8-2x_9)}(\rho)^{x_2}(F)^{x_3}(E)^{x_4}(M)^{(-x_2-x_3-x_4)}(t)^{(2x_3+2x_4+2x_7+x_8+x_{10})}(g)^{x_7}(U)^{x_8}(A)^{x_9}(\omega)^{x_{10}} \qquad \text{- (4.9)}$$

Combining similar powers in (4.9), we have

$$\left(\frac{l^2\rho}{M}\right)^{x_2}\left(\frac{Ft^2}{l^2M}\right)^{x_3}\left(\frac{E}{Mt^2}\right)^{x_4}\left(\frac{t^2g}{l}\right)^{x_7}\left(\frac{tU}{l}\right)^{x_8}\left(\frac{A}{l^2}\right)^{x_9}(\omega t)^{x_{10}} \qquad \text{- (4.10)}$$

In order to have sets of dimensionless numbers $x_2, x_3, x_4, x_7, x_8, x_9$ *and* x_{10} are assumed to lead to 7 dimensionless 'pi' numbers.

Thus we have

$$\pi_1 = \left(\frac{l^2\rho}{M}\right), \pi_2 = \left(\frac{Ft^2}{l^2M}\right), \pi_3 = \left(\frac{E}{Mt^2}\right), \pi_4 = \left(\frac{t^2g}{l}\right), \pi_5 = \left(\frac{tU}{l}\right), \pi_6 = \left(\frac{A}{l^2}\right) \text{and}$$
$$\pi_7 = (\omega t) \qquad \text{- (4.11)}$$

Based on the similarity conditions of the pi numbers, the scaling laws can be obtained. Thus in order to have similarity between the prototype and model, it is assumed that both these system may be represented as

$$prototype : f_p(\pi_1, \pi_2, \pi_3, \pi_4, \pi_5, \pi_6, \pi_7) = 0 \qquad \text{- (4.12)}$$

$$\text{mod}\,el : f_m(\pi_1, \pi_2, \pi_3, \pi_4, \pi_5, \pi_6, \pi_7) = 0 \qquad \text{- (4.13)}$$

Assuming the phenomenon of consideration to be same for prototype and model, the function 'f_p' for the prototype is same as that of the model 'f_m'. The pi numbers of prototype and model are equated and thus we obtain;

$\pi_{1P} = \pi_{1m}$, $\pi_{2p} = \pi_{2m}$, $\pi_{3p} = \pi_{3m}$, $\pi_{4p} = \pi_{4m}$, $\pi_{5p} = \pi_{5m}$, $\pi_{6p} = \pi_{6m}$ and $\pi_{7p} = \pi_{7m}$. - (4.14)

The scale factors can be obtained as follows:

1. $\pi_{1P} = \pi_{1m}$

$$\Rightarrow \left(\frac{l^2\rho}{M}\right)_p = \left(\frac{l^2\rho}{M}\right)_m$$

$$\Rightarrow \frac{M_m}{M_p} = \left(\frac{\rho_m}{\rho_p}\right)\left(\frac{l_m}{l_p}\right)^2 \Rightarrow \Delta_M = \Delta_\rho \Delta_l^2 \qquad \text{- (4.15)}$$

2. $\pi_{2p} = \pi_{2m}$

$$\Rightarrow \left(\frac{Ft^2}{l^2M}\right)_p = \left(\frac{Ft^2}{l^2M}\right)_m$$

$$\Rightarrow \Delta_F = \frac{\Delta_M \Delta_l^2}{\Delta_t^2} \qquad \text{- (4.16)}$$

3. $\pi_{3p} = \pi_{3m}$

$$\Rightarrow \left(\frac{E}{Mt^2}\right)_p = \left(\frac{E}{Mt^2}\right)_m \qquad \text{- (4.17)}$$

$$\Rightarrow \Delta_E = \Delta_M \Delta_t^2$$

4. $\pi_{4p} = \pi_{4m}$

$$\Rightarrow \left(\frac{t^2 g}{l}\right)_p = \left(\frac{t^2 g}{l}\right)_m \qquad \text{- (4.18)}$$

$$\Rightarrow \Delta_t = \sqrt{\frac{\Delta_l}{\Delta_g}}$$

But g is same for both model and prototype, thus $\Delta_g = 1, \therefore \Delta_t = \sqrt{\Delta_l}$

5. $\pi_{5p} = \pi_{5m}$

$$\Rightarrow \left(\frac{tU}{l}\right)_p = \left(\frac{tU}{l}\right)_m \qquad \text{- (4.19)}$$

$$\Rightarrow \Delta_U = \frac{\Delta_l}{\Delta_t}$$

6. $\pi_{6p} = \pi_{6m}$

$$\Rightarrow \left(\frac{A}{l^2}\right)_p = \left(\frac{A}{l^2}\right)_m \qquad \text{- (4.20)}$$

$$\Rightarrow \Delta_A = \Delta_l^2$$

7. $\pi_{7p} = \pi_{7m}$

$$\Rightarrow (\omega t)_p = (\omega t)_m$$

$$\Rightarrow \Delta_\omega = \frac{1}{\Delta_t} \qquad \text{- (4.21)}$$

Substituting the value of $\Delta_t = \sqrt{\Delta_l}$ in the above equations we have

I. $$\Delta_M = \Delta_\rho \Delta_l^2 \quad \text{- (4.22)}$$

II. $$\Delta_F = \frac{\Delta_M \Delta_l^2}{\Delta_t^2} = \Delta_M \Delta_l \quad \text{- (4.23)}$$

III. $$\Delta_E = \Delta_M \Delta_t^2 = \Delta_M \Delta_l \quad \text{- (4.24)}$$

IV. $$\Delta_U = \sqrt{\Delta_l} \quad \text{- (4.25)}$$

V. $$\Delta_A = \Delta_l^2 \quad \text{- (4.26)}$$

VI. $$\Delta_\omega = \frac{1}{\sqrt{\Delta_l}} \quad \text{- (4.27)}$$

The details of the prototype are as follows:

Length of the span	142 meters
Diameter of the conductor	35.56 mm
Density of Aluminium	2700 kg/m3
Density of ice	917 kg/m3
Mass per unit length of the conductor	2.375 kg/m

Table 4.2: Parameters of the transmission line conductor used for scale modeling

4.4 Scale modeling of transmission line cables

In section 4.3 above, the scale factors necessary to model the transmission line cable were derived. Experimental investigations are performed on two different types of models: Actual and the Scaled model. Figure 4.2.a, 4.2.b and 4.2.c shows the Scaled Model and Actual model.

Fig 4.2 a.: Picture of the Scaled model; b.: Actual model; c.: Actual model with ice.

Actual model as shown in the figure 4.2.b above is a small segment of the actual transmission line cable. EPOXY is used to represent ice on the cable. Figure 4.2.c shows the actual model with ice on it. The models are supported by a rectangular frame with the help of eight helical springs. The design and selection of the springs depends upon the dimensions and types of models used. The figure 4.3 shows the model arrangement in the test section of the wind tunnel.

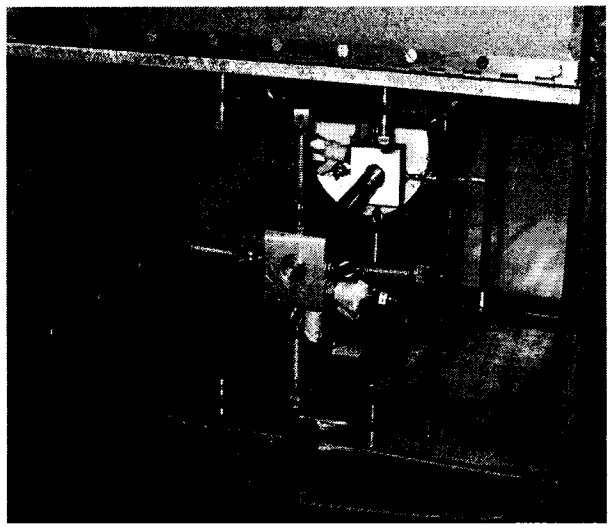

Fig 4.3: Model suspended by springs in the test section

Scale model technique is employed to obtain the dimensions of the models and springs. The design and dimensions of the cable models and the springs to be tested in a wind tunnel are given in Appendix II.

4.5 Model analysis by the principle of co-ordinate couplings for actual and scaled models

As mentioned earlier, the models are supported by a rectangular frame with the help of four horizontal and four vertical springs. Each end of the model is supported by two horizontal springs and two in vertical directions as shown in figure 4.4 below.

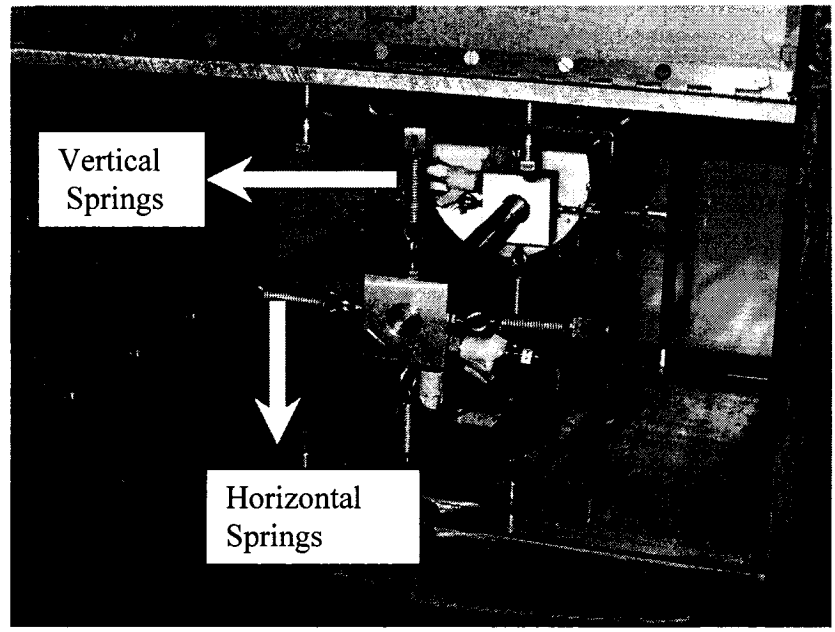

Fig 4.4: Spring- Model arrangement in the test section of wind tunnel

The model and the spring arrangement are shown in the X-Y lane in the figure 4.5 below.

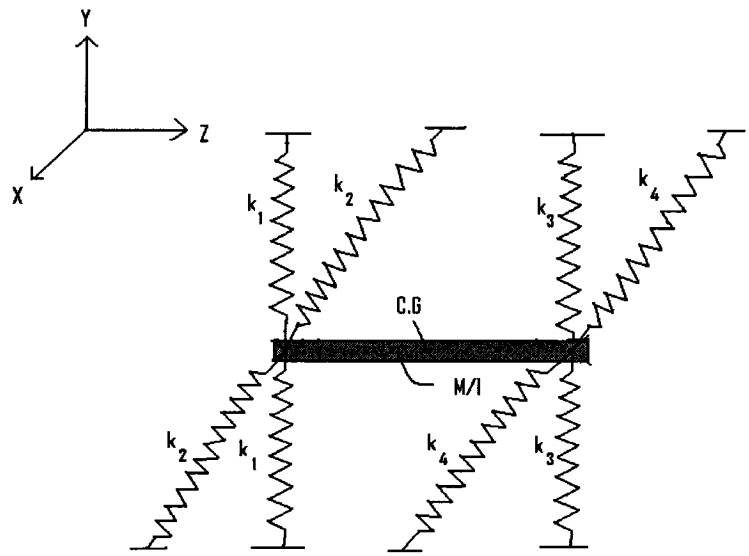

Fig 4.5: Free body diagram of the model-spring arrangement

In the figure 4.4 above k_1 and k_3 are the springs in vertical directions whereas k_2 and k_4 are the springs in horizontal directions. The equivalent stiffness K_1 can be written as follows:

$$K_1 = k_1 + k_1 = 2k_1 \qquad \text{- (4.48)}$$

Similarly the equivalent stiffness of other springs can be written as follows:

$$K_2 = 2k_2 \qquad \text{- (4.49)}$$

$$K_3 = 2k_3 \text{ and} \qquad \text{- (4.50)}$$

$$K_4 = 2k_4 . \qquad \text{- (4.51)}$$

The figure below shows the rod being supported by four equivalent springs.

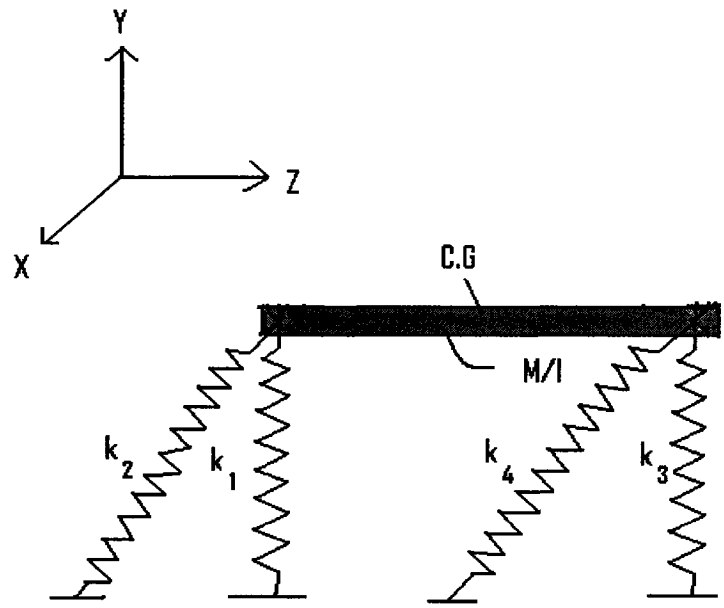

Fig 4.6: Equivalent spring-model system

4.5.1 Equations of motions of rod in Y-direction with no aerodynamic forces

Using the principle of co-ordinate coupling, the equations of motion of rod supported by vertical and horizontal equivalent springs under the absence of wind are derived. The rod undergoes deflections of x and y in vertical and horizontal directions, respectively, and angular deflection of α and θ in X and Y directions, respectively. In the actual model, $K_1 = K_3$ and $L_1 = L_2$; y, y_1 and y_2 are measured from the static equilibrium position.

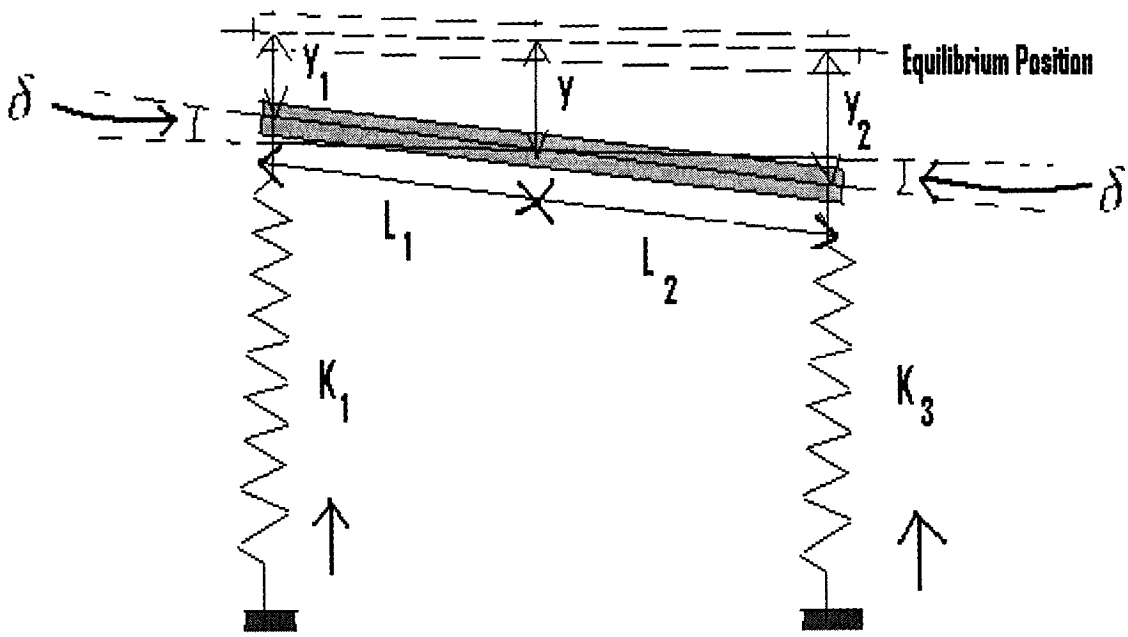

Fig 4.7: Free body diagram of the model-spring system in X-Y Plane

The figure 4.5 above shows the model being supported by vertical equivalent springs. The C.G. of the rod makes a deflection of 'y' meters whereas the end makes deflections of y_1 *and* y_2, respectively. As mentioned before the rod makes an angular deflection of δ radians.

From the above figure, the deflections of the centre of gravity (C.G.) can be expressed in terms of the end deflections y_1 and y_2 as follows

$$y = y_2 - L_2\delta \qquad \text{- (4.52)}$$

The equation (4.52) can be rearranged as

$$y_2 = y + L_2\delta \qquad \text{- (4.53)}$$

Similarly $y = y_1 + L_1\delta$ - (4.54)

and this gives $y_1 = y - L_1\delta$ - (4.55)

Applying Newton's laws of Motion to the model-spring arrangement as shown in the figure 4.5, we have the inertia force $M\ddot{y}$ being balanced by the spring force. Thus

$$M\ddot{y} = -K_1y_1 - K_3y_2 \qquad \text{- (4.56)}$$

Substituting the values of k_1 and k_3, 4.56 can be written as

$$M\ddot{y} = -2k_1(y - L_1\delta) - 2k_3(y + L_2\delta) \quad \text{- (4.57)}$$

The above equation 4.57 can be rearranged as follows:

$$M\ddot{y} + 2k_1(y - L_1\delta) + 2k_3(y + L_2\delta) = 0 \quad \text{- (4.58)}$$

The Moment equation of the rod assuming clockwise direction as positive can be written as

$$I\ddot{\delta} = +K_1 y_1 L_1 - K_3 y_2 L_2 \quad \text{- (4.59)}$$

Again on substitution of K_1 and K_3, we have

$$I\ddot{\delta} = 2k_1(y - L_1\delta)L_1 - 2k_3(y + L_2\delta)L_2 \quad \text{- (4.60)}$$

Rearranging (4.60),

$$I\ddot{\delta} - 2k_1(y - L_1\delta)L_1 + 2k_3(y + L_2\delta)L_2 = 0 \quad \text{- (4.61)}$$

Similarly in X – Direction, the motion and moment equation can be written as

$$M\ddot{x} + 2k_2(x - L_1\phi) + 2k_4(x + L_2\phi) = 0 \quad \text{- (4.62)}$$

$$I\ddot{\phi} - 2k_2(x - L_1\phi)L_1 + 2k_4(x + L_2\phi)L_2 = 0 \quad \text{- (4.63)}$$

Rearranging the equations we have

$$M\ddot{y} + (2k_1 + 2k_3)y + (-2k_1L_1 + 2k_3L_2)\delta = 0 \qquad \text{- (4.67)}$$

$$M\ddot{x} + (2k_2 + 2k_4)x + (-2k_2L_1 + 2k_4L_2)\phi = 0 \qquad \text{- (4.68)}$$

$$I\ddot{\delta} + (-2k_1L_1 + 2k_3L_2)y + (2k_1L_1^2 + 2k_3L_2^2)\delta = 0 \qquad \text{- (4.69)}$$

$$I\ddot{\phi} + (-2k_2L_1 + 2k_4L_2)x + (2k_2L_1^2 + 2k_4L_2^2)\phi = 0 \qquad \text{- (4.70)}$$

Writing the above equations in matrix form, we have

$$\begin{vmatrix} M & 0 & 0 & 0 \\ 0 & M & 0 & 0 \\ 0 & 0 & I & 0 \\ 0 & 0 & 0 & I \end{vmatrix} \begin{Bmatrix} \ddot{y} \\ \ddot{x} \\ \ddot{\delta} \\ \ddot{\phi} \end{Bmatrix} + \begin{vmatrix} (2k_1 + 2k_3) & 0 & (2k_1L_1 + 2k_3L_2) & 0 \\ 0 & (2k_2 + 2k_4) & 0 & (2k_2L_1 + 2k_4L_2) \\ (-2k_1L_1 + 2k_3L_2) & 0 & (2k_1L_1^2 + 2k_3L_2^2) & 0 \\ 0 & (2k_2L_1 + 2k_4L_2) & 0 & (2k_2L_1^2 + 2k_4L_2^2) \end{vmatrix} \begin{Bmatrix} y \\ x \\ \delta \\ \phi \end{Bmatrix} = 0$$

- (4.71)

The above matrix equation is solved for the Eigen values which are obtained as follows:

λ_e = 1.0e+003 *

1.5231
1.5231
4.5692
4.5692

The frequencies are $\omega_{nx1} = \omega_{ny1}$ = 39.02 radians per second, and $\omega_{nx2} = \omega_{ny2}$ = 67.59 rad /s. Further $\frac{\omega_{nx2}}{\omega_{nx1}}$ = 1.7.

4.5.2 Equations of motions of rod in Y-direction when aerodynamic forces are considered

In the previous section, equations of motions of the model with springs were derived without wind force. In this section the equations of motion of the model under the action of aerodynamic forces are derived. The figure 4.6 below shows the cross section of the model with springs placed perpendicular to the direction of the wind.

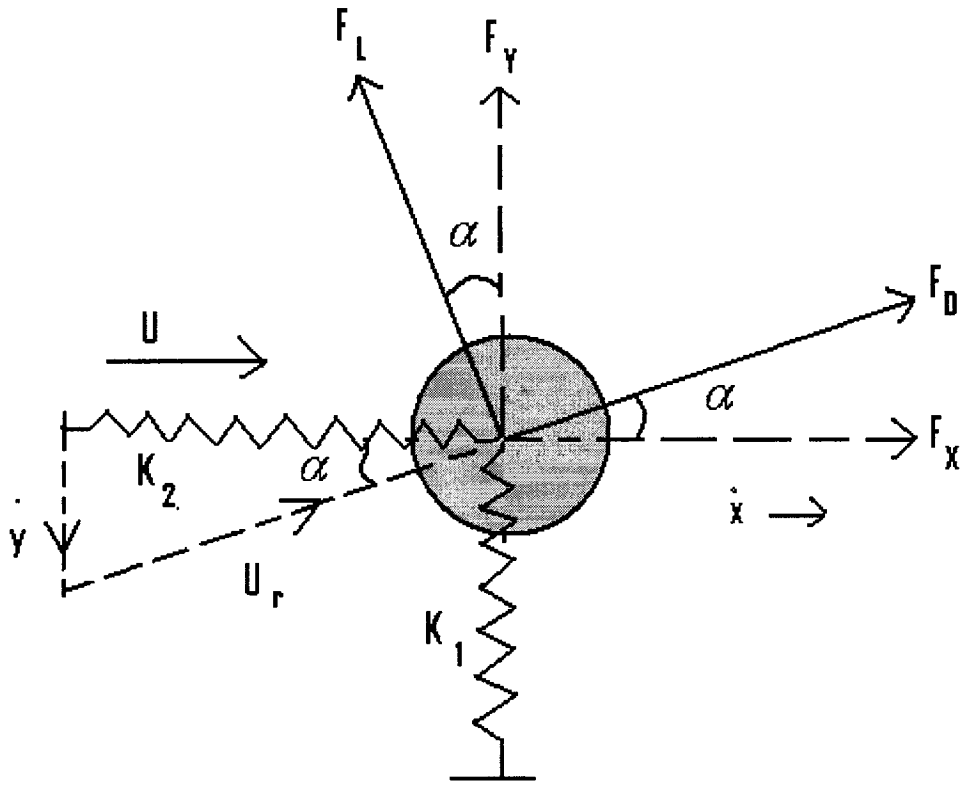

Fig 4.8: Free-body diagram of the cable model with springs under the action of aerodynamic forces

The relative velocity diagram is shown in the figure 4.7 below, where $\dot{y}$ is the velocity of the wind relative to the cable.

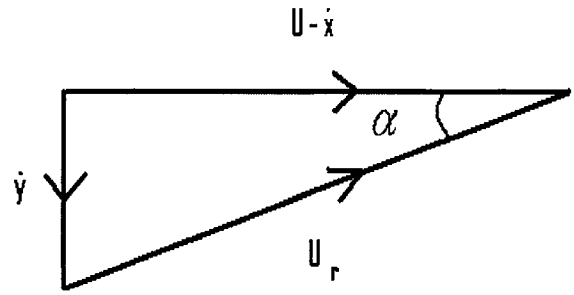

Fig 4.9: Relative velocity diagram

From the above figure 4.7, we see that U_r, the relative wind velocity can be expressed as follows:

$$U_r^2 = \left(U - \dot{x}\right)^2 + \left(\dot{y}\right)^2 \qquad \text{- (4.71)}$$

$$\approx U^2 - 2U\dot{x} \text{ (Neglecting higher powers in } \dot{x} \text{ and } \dot{y}\text{)} \qquad \text{- (4.72)}$$

The angle subtended by the relative wind velocity to horizontal α can be expressed as

$$\tan\alpha = \frac{\dot{y}}{U - \dot{x}} \approx \frac{\dot{y}}{U} \text{ (} \dot{x} \text{ is neglected as it is much smaller than U)}$$

- (4.73)

As mentioned before in chapter 2, the drag and lift force can be expressed as

$$F_D = \frac{1}{2}\rho_a A_m U_r^2 C_D(\theta, U_r) \qquad \text{- (4.74)}$$

$$F_L = \frac{1}{2}\rho_a A_m U_r^2 C_L(\theta, U_r) \qquad \text{- (4.75)}$$

From figure 4.6, the total horizontal force can be expressed as

$$F_X = F_D \cos\alpha - F_L \sin\alpha \qquad \text{- (4.76)}$$

Similarly vertical force can be expressed as

$$F_Y = F_D \sin\alpha + F_L \cos\alpha \qquad \text{- (4.77)}$$

Since α is small, (4.76) and (4.77) can be written as

$$F_X = F_D - F_L\alpha \qquad \text{- (4.78)}$$

and $$F_Y = F_D\alpha + F_L \qquad \text{- (4.79)}$$

Substituting the expressions for F_D, F_L, U, α in F_X and F_Y, we have

$$F_X = \frac{1}{2}\rho_a A_m\left(U^2 - 2U\dot{x}\right)C_D - \frac{1}{2}\rho_a A_m\left(U^2 - 2U\dot{x}\right)C_L\left(\frac{\dot{y}}{U}\right) \qquad \text{- (4.80)}$$

Rearranging the above equation, we have

$$F_X = \frac{1}{2}\rho_a A_m C_D U^2 - \rho_a A_m U C_D \dot{x} - \frac{1}{2}\rho_a A_m U C_L \dot{y} + \rho_a A_m C_L \dot{x}\dot{y}$$

$$\Rightarrow F_X = \frac{1}{2}c_{mXX}U - c_{mXX}\dot{x} - \frac{1}{2}c_{mXY}\dot{y} + \frac{c_{mXY}}{U}\dot{x}\dot{y} \qquad \text{- (4.81)}$$

where $c_{mXX} = \rho_a A_m U C_D$ and $c_{mXY} = \rho_a A_m U C_L$

Similarly F_Y can be expressed as

$$F_Y = \frac{1}{2}\rho_a A_m C_L U^2 - \rho_a A_m U C_L \dot{x} + \frac{1}{2}\rho_a A_m U C_D \dot{y} - \rho_a A_m C_D \dot{x}\dot{y}$$

$$\Rightarrow F_Y = \frac{1}{2}c_{mYX}U - c_{mYX}\dot{x} + \frac{1}{2}c_{mYY}\dot{y} - \frac{c_{mYY}}{U}\dot{x}\dot{y} \qquad \text{- (4.82)}$$

where $c_{mYX} = \rho_a A_m U C_L$ and $c_{mYY} = \rho_a A_m U C_D$

The equations of motions of the rod considering aerodynamic forces are

$$M\ddot{y} + (2k_1 + 2k_3)y + (-2k_1L_1 + 2k_3L_2)\delta = -F_y \qquad \text{- (4.83)}$$

$$M\ddot{x} + (2k_2 + 2k_4)x + (-2k_2L_1 + 2k_4L_2)\phi = F_x \qquad \text{- (4.84)}$$

$$I\ddot{\delta} + (-2k_1L_1 + 2k_3L_2)y + (2k_1L_1^2 + 2k_3L_2^2)\delta = 0 \qquad \text{- (4.85)}$$

$$I\ddot{\phi} + (-2k_2L_1 + 2k_4L_2)x + (2k_2L_1^2 + 2k_4L_2^2)\phi = 0 \qquad \text{- (4.86)}$$

On substituting the expression for F_y, equation 4.83 can be written as

$$M\ddot{y}+(2k_1+2k_3)y+(-2k_1L_1+2k_3L_2)\delta=-\frac{1}{2}c_{mYX}U+c_{mYX}\dot{x}-\frac{1}{2}c_{mYY}\dot{y}+\frac{c_{mYY}}{U}\dot{x}\dot{y}$$

$$\Rightarrow M\ddot{y}+(2k_1+2k_3)y+(-2k_1L_1+2k_3L_2)\delta-c_{mYX}\dot{x}+\frac{1}{2}c_{mYY}\dot{y}-\frac{c_{mYY}}{U}\dot{x}\dot{y}=-\frac{1}{2}c_{mYX}U$$

- (4.87)

Similarly (4.84) can be rearranged as

$$M\ddot{x}+(2k_2+2k_4)x+(-2k_2L_1+2k_4L_2)\phi=\frac{1}{2}c_{mXX}U-c_{mXX}\dot{x}-\frac{1}{2}c_{mXY}\dot{y}+\frac{c_{mXY}}{U}\dot{x}\dot{y}$$

$$\Rightarrow M\ddot{x}+(2k_2+2k_4)x+(-2k_2L_1+2k_4L_2)\phi+c_{mXX}\dot{x}+\frac{1}{2}c_{mXY}\dot{y}-\frac{c_{mXY}}{U}\dot{x}\dot{y}=\frac{1}{2}c_{mXX}U$$

- (4.88)

Thus the equations of motions of the rod considering aerodynamic forces can be summarized as follows

$$M\ddot{y}+(2k_1+2k_3)y+(-2k_1L_1+2k_3L_2)\delta-c_{mYX}\dot{x}+\frac{1}{2}c_{mYY}\dot{y}-\frac{c_{mYY}}{U}\dot{x}\dot{y}=-\frac{1}{2}c_{mYX}U$$

- (4.87)

$$M\ddot{x}+(2k_2+2k_4)x+(-2k_2L_1+2k_4L_2)\phi+c_{mXX}\dot{x}+\frac{1}{2}c_{mXY}\dot{y}-\frac{c_{mXY}}{U}\dot{x}\dot{y}=\frac{1}{2}c_{mXX}U$$

- (4.88)

$$I\ddot{\delta}+(-2k_1L_1+2k_3L_2)y+(2k_1L_1^2+2k_3L_2^2)\delta=0$$

- (4.89)

$$I\ddot{\phi}+(-2k_2L_1+2k_4L_2)x+(2k_2L_1^2+2k_4L_2^2)\phi=0$$

- (4.90)

Thus solving the above equations for actual model with ice in MATLAB, we have the X and Y direction responses in figure 4.10 and the whirling motions of the actual cable model in Fig 4.11.a. The angle of attack of the wind is taken to be 90° and co-efficient of drag and lift forces were again taken from O. Chabart's work [16]. The co-efficient of drag and lift forces were 1.95 and 0.45, respectively. The wind speed is 5 m/sec and the angle of incidence of wind on cable $\beta = 0°$.

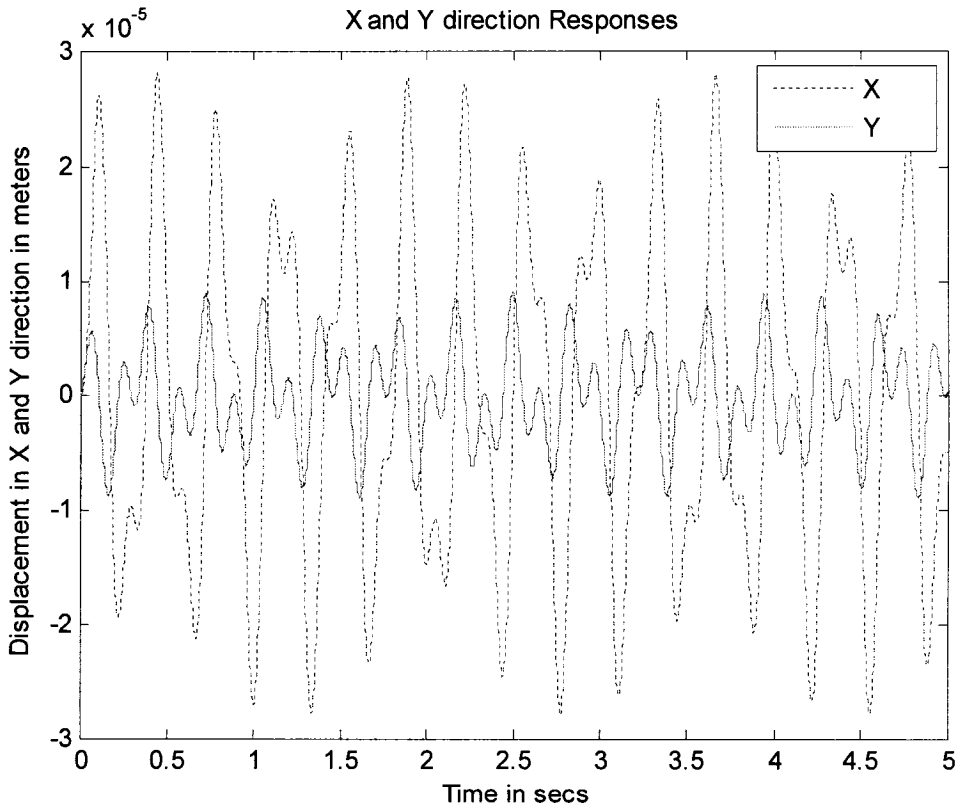

Fig 4.10: X and Y direction responses over time for actual model at 5 m/s wind speed

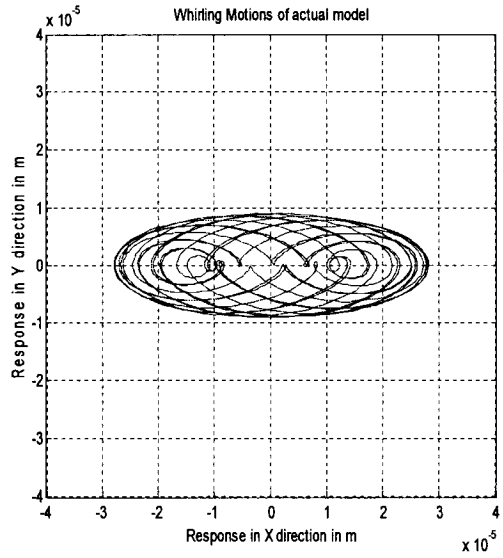

Fig 4.11.a: Whirling motions of actual model with ice at 5 m/s

The figure 4.11.a gives the Lissajous figure or orbital motions of the actual model with ice at 5m/s and $\theta = 90°$. Although the inner orbits were not elliptical in nature, the outer orbits were elliptical with major axis on X plane. Under similar conditions the orbital motions of scaled model at 5 m/sec is obtained as follows;

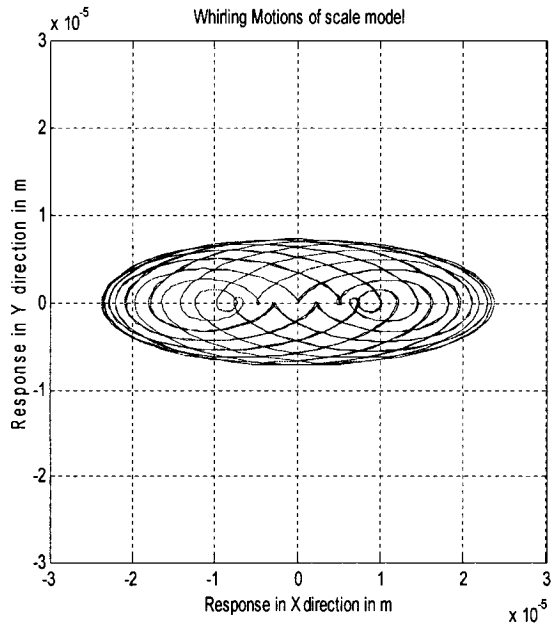

Fig 4.11.b: Whirling motions of scale model at 5 m/s

The model analysis on actual and scaled cable models were performed to show that the models when tested in the wind tunnel would exhibit similar responses as those obtained analytically in chapter 3. From the figures 4.11.a and 4.11.b, it can be noticed that the overall shape of the orbits were elliptical with major axis on X plane when the wind flow was horizontal. This validates that the scale modeling and the model analysis performed on the cables were meaningful and matches with the responses obtained analytically. In chapter 5, experimental investigations have been performed on actual and scaled model with and without ice under various conditions.

4.6 Summary

In this chapter, the principle of scale modeling employed to obtain the dimensions of actual and scaled model. Principle of co-ordinate coupling was used to obtain the equations of motions of the model-spring arrangement in the wind tunnel considering the aerodynamic excitations. Model testing of the cable models was performed by simulating the equations of motions in MATLAB. In the next chapter, experimental investigations were carried out on actual and scale models of the transmission line conductor. The orbital motions at various wind speeds and angles of attack were obtained.

CHAPTER 5

EXPERIMENTAL INVESTIGATIONS

In chapter 2, a continuous model for transmission line system was derived incorporating the aerodynamic instability of the system, and the orbital responses of the system under the action of wind were studied in chapter 3. In order to validate the analytical studies on the orbital motions of the transmission lines cables, the dynamic responses in the actual system are experimentally measured.

In this chapter, the actual cable and scale models are analyzed for the factors responsible for orbital motions of the cable. The models are tested in the wind tunnel as shown in figure 5.1 and the orbital motions are obtained for actual cable and scale model under different wind speeds, angles of attack and with and without the effect of ice. EPOXY is used to represent ice on the models.

Several studies have illustrated different methods of experimentation to describe the orbital behaviour of transmission line cables. In the present work, the cable model was suspended by four springs on either side as shown in figure 5.1.b. The springs help in bringing down the stiffness of the model to that of an actual transmission line.

5.1 Experimental set-up, description and instruments

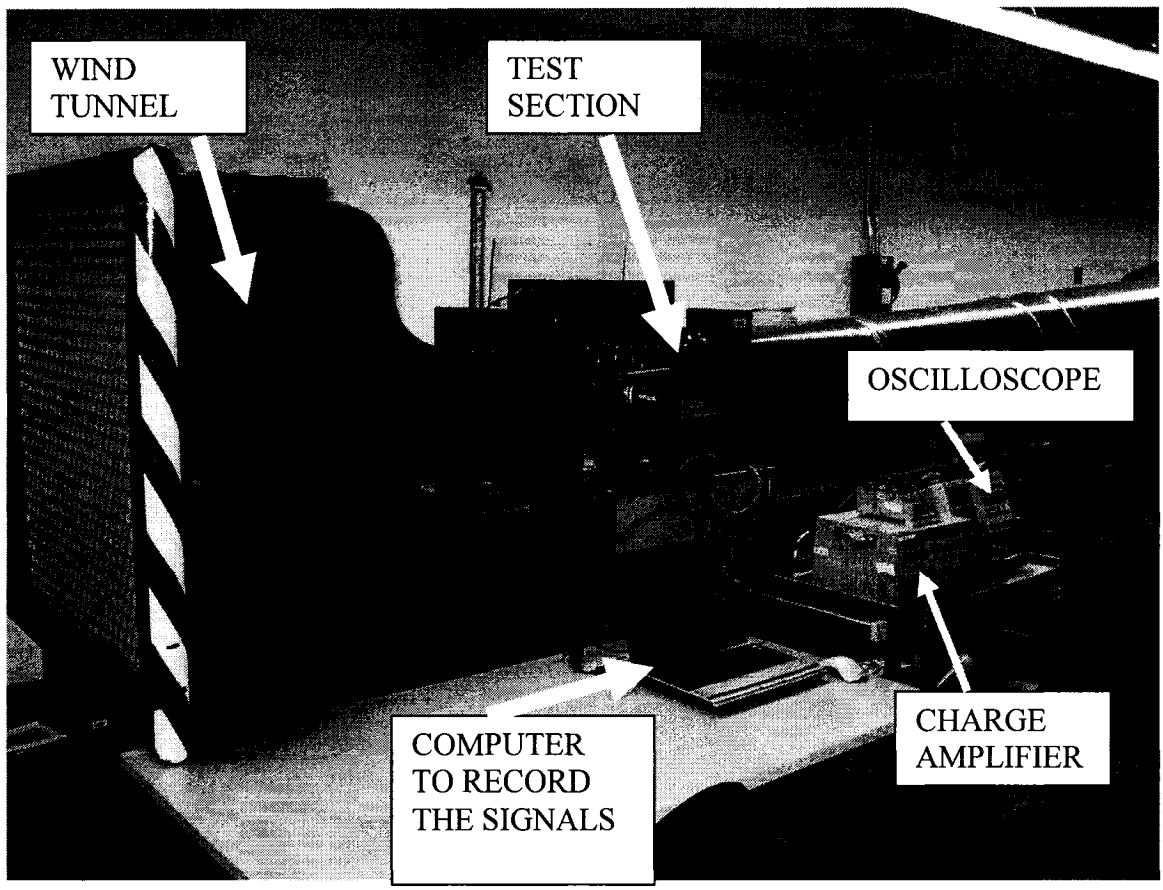

Fig 5.1.a: Experimental set-up

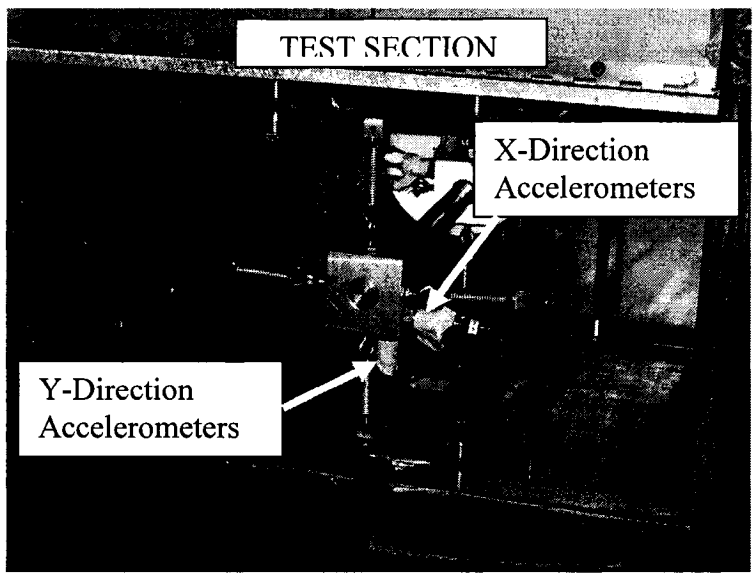

Fig 5.1.b: Spring-model arrangement in the test section

5.1.1 Accelerometers

Four similar accelerometers are used to measure the accelerations of the model as shown in the figure 5.1.b, two in each side of the rod, one for X-direction measurement and the other for Y-direction.

5.1.2 Charge amplifiers

The signals received by the accelerometers are sent to amplifiers. The displacements are input to an oscilloscope for measuring the accelerations.

5.2 Accelerometer calibrations

It is important to know the exact accelerometer sensitivity at various frequencies of interest. The sensitivity of an accelerometer is usually expressed in mV/g (voltage mode) or pC/g (charge mode) at a given frequency [82]. The accelerometers are calibrated to accurately determine the sensitivity at various frequencies throughout the frequency range of interest. An unknown accelerometer is attached to the back-to-back of a standard accelerometer and thus, both accelerometers experience the same motion. At each frequency of interest, the g-level is precisely set by measuring the output of the standard accelerometer. At the same time or alternately, the output of the unknown accelerometer is measured and sensitivity (mV/g or pC/g) versus frequency is obtained.

5.3 Experimental investigations

The schematic representation of the experimental testing of the models in the wind tunnel is shown in the figure 5.2 below.

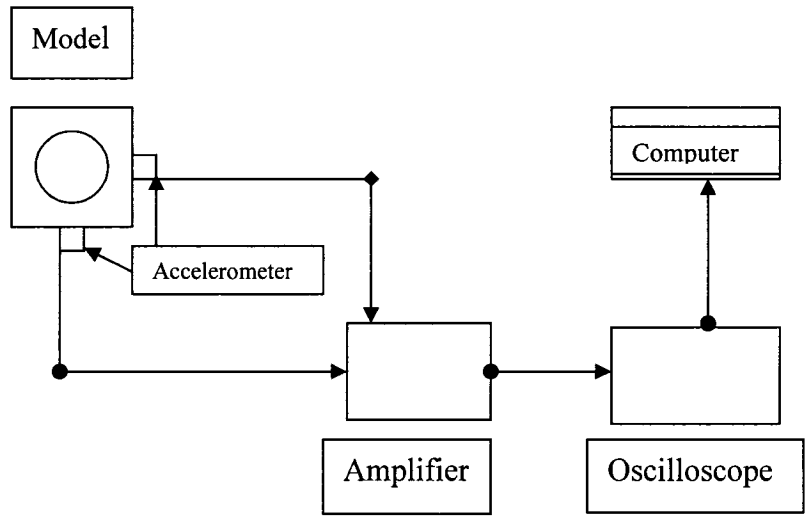

Fig 5.2: Schematic sketch of the transmission line model testing

The experimental testing has four stages. In the first stage the actual model without ice is suspended with the help of springs and is placed perpendicular to the direction of wind. The orbits are obtained for the three different sets of wind velocities. In the second stage the actual model with ice is placed in the rectangular frame suspended by springs. The model is tested for three different angles of attack, namely, 0°, 25° and 90°. Under each angle of attack, the orbits are obtained for three different wind speeds. The third and fourth stages are

testing the scale model with and without ice for the same angles of attack and wind speeds.

5.4 Experimental results

5.4.1 Actual model without ice

The actual model as shown in figure 4.2.b is tested in wind tunnel under various wind speeds. In the present work, results for two speeds are presented.

5.4.1.1 At a wind speed of 7.6 m/s (1500 feet per minute)

The responses of the actual cable in X and Y directions over time 't' are shown in the figure 5.3.a and 5.3.b, respectively, below. It can be noticed that the actual cable exhibits self excited vibrations with the amplitudes gradually increasing with time.

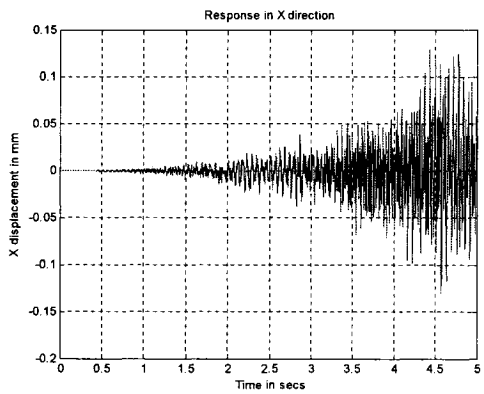

5.3. a: Response in X direction over time 't'

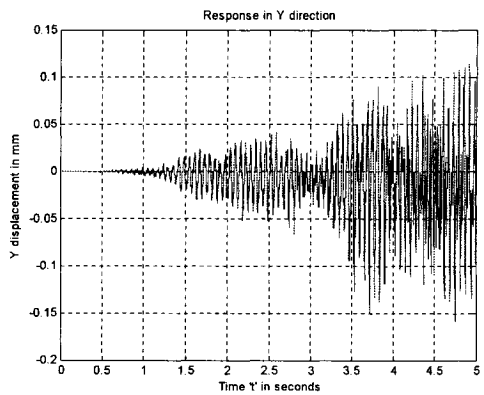

5.3. b.: Response in Y direction over time 't'

It can be noticed from the figures 5.3.a and 5.3.b that the amplitudes of the vibrations keep increasing from rest and at the fifth second of the response it begins to stabilize. The orbits cannot be plotted for the entire time response since it would result in some complex figure including transients. The first natural frequency of the system was 39 rad/s or 6.12 Hz. Thus it would take 0.15 second to complete a cycle. Taking this into consideration, a single orbit was plotted at the 5^{th} second of the response in order to understand the nature and orientation of the whirl.

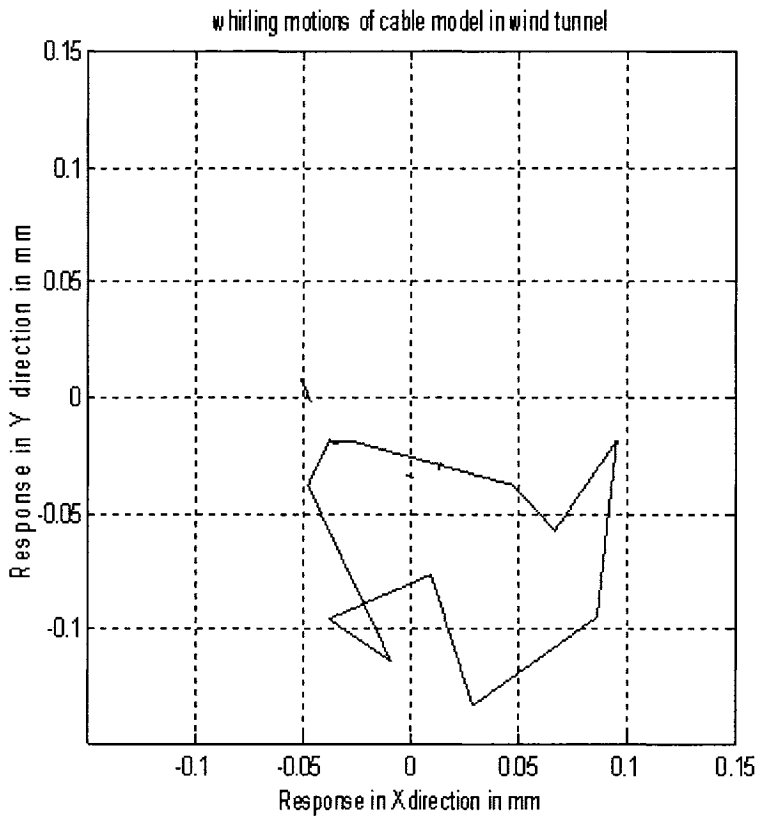

Fig 5.4: Orbital motion of actual cable model at 1500 feet per minute

The figure 5.4 shows the orbital motions of the actual transmission line cable when tested in wind tunnel at 7.6 m/s (1500 feet per minute). The orbit was

plotted at the fifth second of the response. The motion follows a closed orbit, with some resemblance to an ellipse.

5.4.2 Actual cable with ice

As mentioned earlier in chapter 4, EPOXY is used to represent ice model on the actual cables. Figure 4.2.c shows the actual cable with ice which is tested in wind tunnel under various wind speeds. In the present work, whirling motions of the cables are obtained for three angles of attacks of the wind.

5.4.2.1 At θ = 90 degrees ; 7.5 m/s (1480 feet per minute)

The responses of the actual transmission line model in X and Y directions and the orbital motions at 7.5 m/s (1480 feet per minute) are shown in the figure 5.5.a, 5.5.b and 5.5.c, respectively.

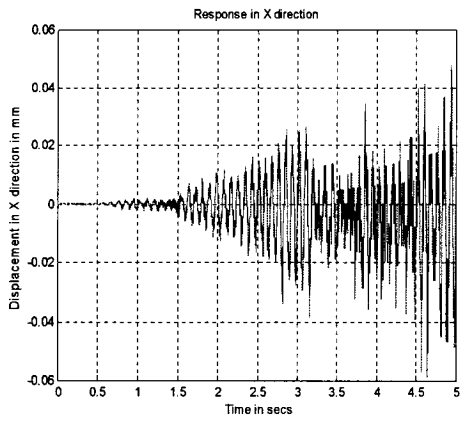

5.5. a: Response in x direction over time 't'

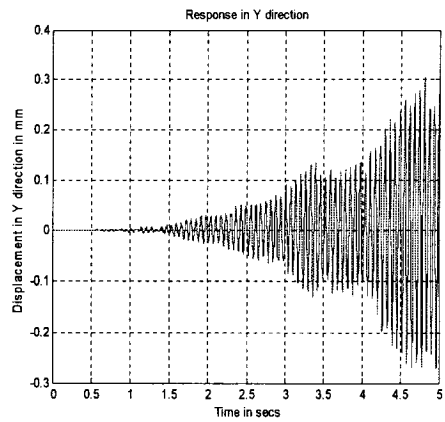

5.5. b.: Response in Y direction over time 't'

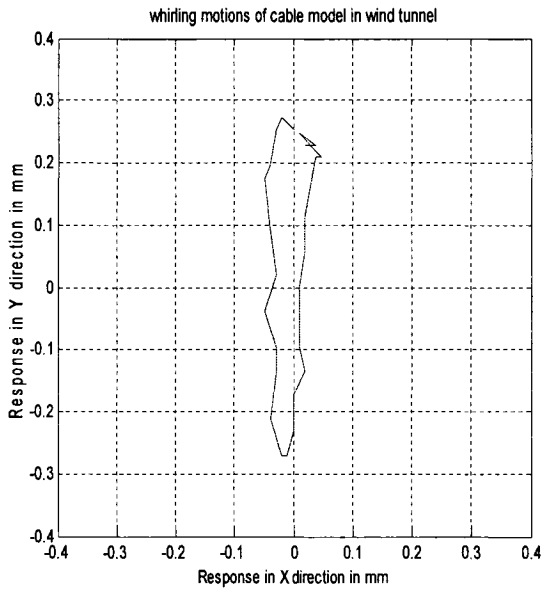

Fig 5.5.c: Whirling motion of actual cable model at 7.5 m/s (1480 feet per minute)

The figure 5.5.c shows the orbital motions of the actual transmission line cable when tested in wind tunnel at 7.5 m/s (1480 feet per minute). The orbit was plotted at the fifth second of the response. The shape of the orbit has some resemblance to an ellipse with major axis on Y plane.

5.4.2.2 At an Angle of Attack θ = 90 degrees; 9.1 m/s (1800 feet per minute)

The orbital motion of the actual transmission line cable at 9.1 m/s (1800 feet per minute) are shown in the figure 5.6.

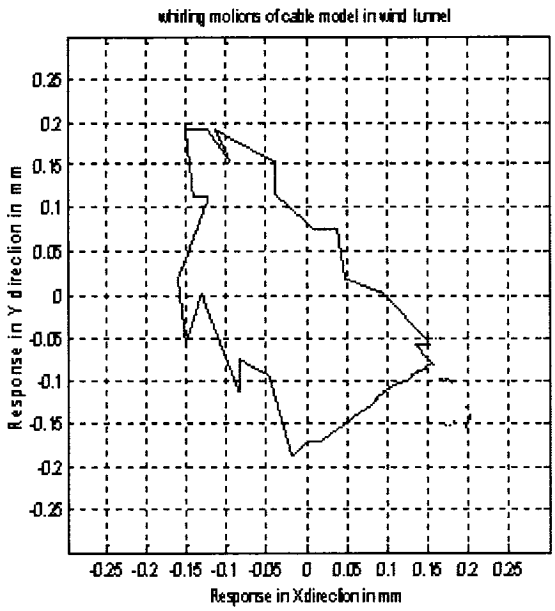

Fig 5.6: Whirling motion of actual cable model at 1800 feet per minute

5.4.2.3 At θ = 0 degrees ; 7.6 m/s (1500 feet per minute)

The responses of the actual transmission line cable in X and Y directions and the orbital motions at 7.6 m/s (1500 feet per minute) and for angle of attack θ = 0° are shown in the figure 5.7.a, 5.7.b and 5.7.c, respectively.

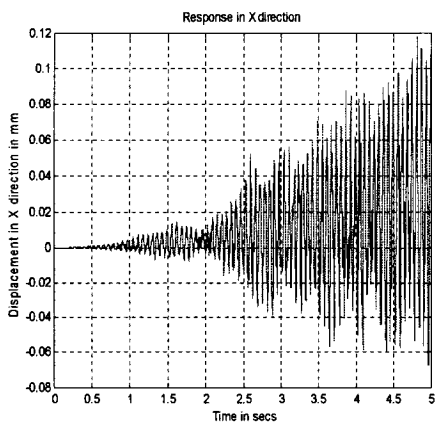

5.7. a: Response in x direction over time 't'

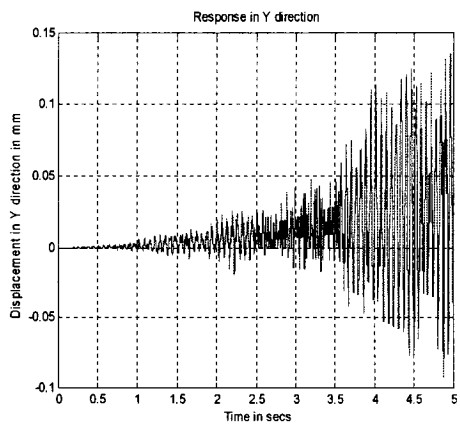

5.7. b.: Response in Y direction over time 't'

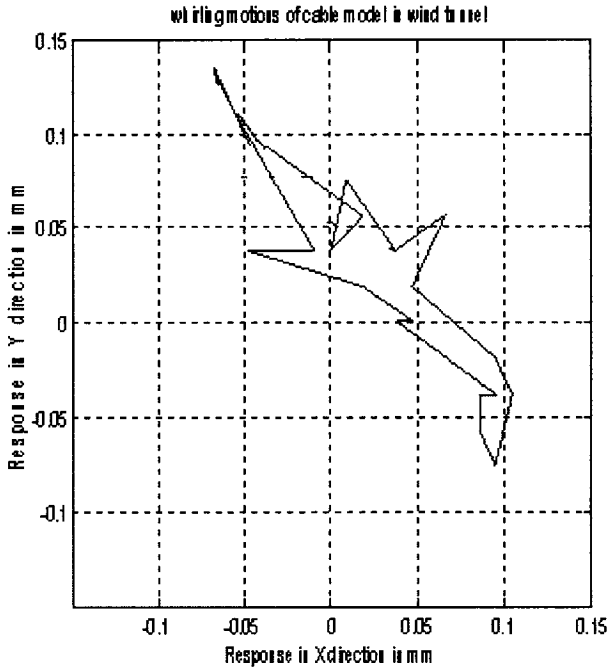

Fig 5.7.c: Whirling motion of actual cable model at 1500 feet per minute

The figure 5.7.c shows the orbital motions of the actual transmission line cable when tested in wind tunnel at 7.6 m/s (1500 feet per minute). The orbits were plotted at the fifth second of the response. The values of the co-efficient of drag and lift forces considered in chapter 3 were based on O. Chabart's experimental results [16] whereas those considered in the present's work experimentation are different. This is explained in the section 5.5 where a comparison is made between the analytical and the experimental results.

5.4.2.4 At θ = 0 degrees ; 14.9 m/s (2950 feet per minute)

The orbital motion of the actual transmission line cable model at 14.9 m/s (2950 feet per minute) are shown in the figure 5.8.

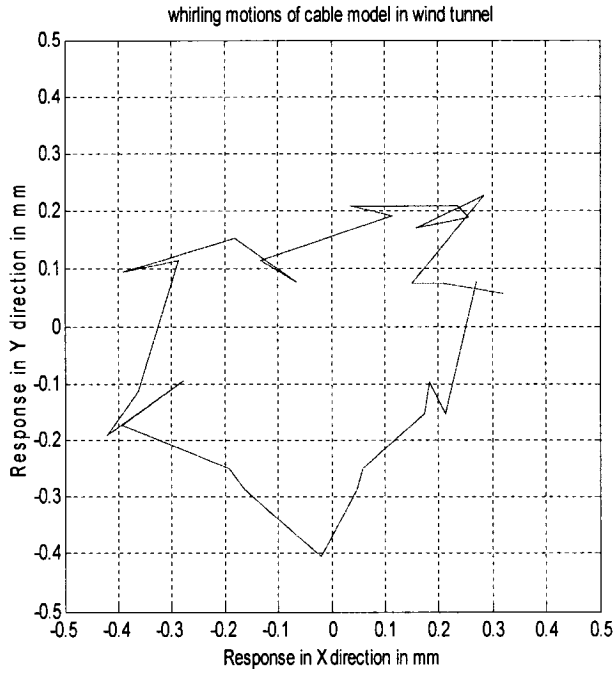

Fig 5.8: Whirling motion of actual cable model at 2950 feet per minute

5.4.2.5 At θ = 25 degrees ; 8.07 m/s (1590 feet per minute)

The responses of the actual transmission line cable in X and Y directions and the orbital motions at 8.07 m/s (1480 feet per minute) and for angle of attack θ = 25° are shown in the figure 5.9.a, 5.9.b and 5.9.c, respectively.

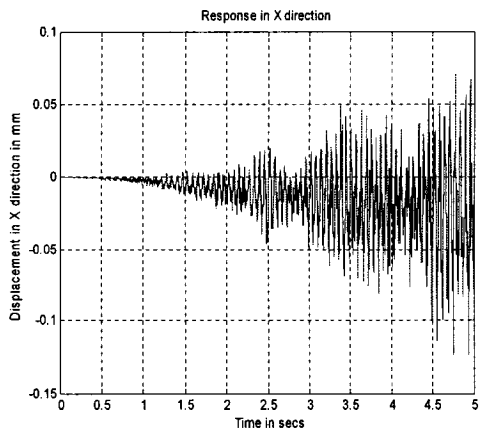

5.9. a: Response in x direction over time 't'

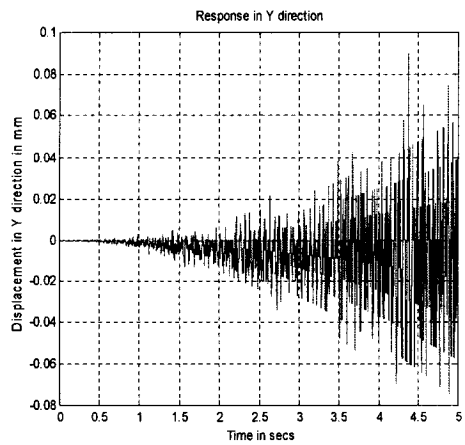

5. 9. b.: Response in Y direction over time 't'

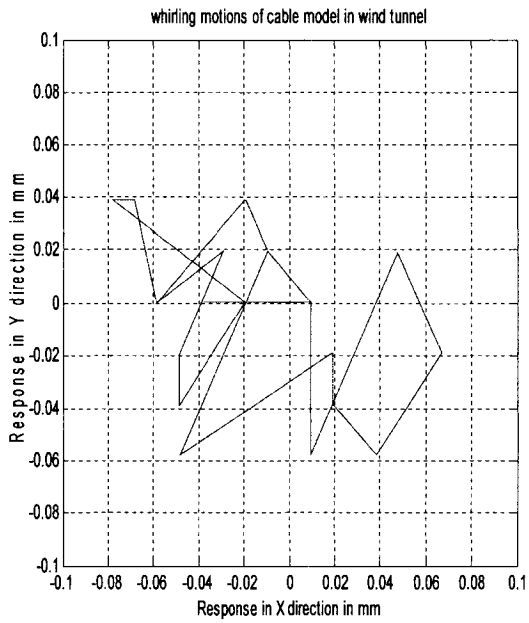

Fig 5.9.c: Whirling motion of actual cable model at 1590 feet per minute

5.4.2.6 At θ = 25 degrees ; 14.52 m/s (2860 feet per minute)

The whirl motion of the actual transmission line cable at 14.52 m/s (2860 feet per minute) are shown in the figure 5.10.

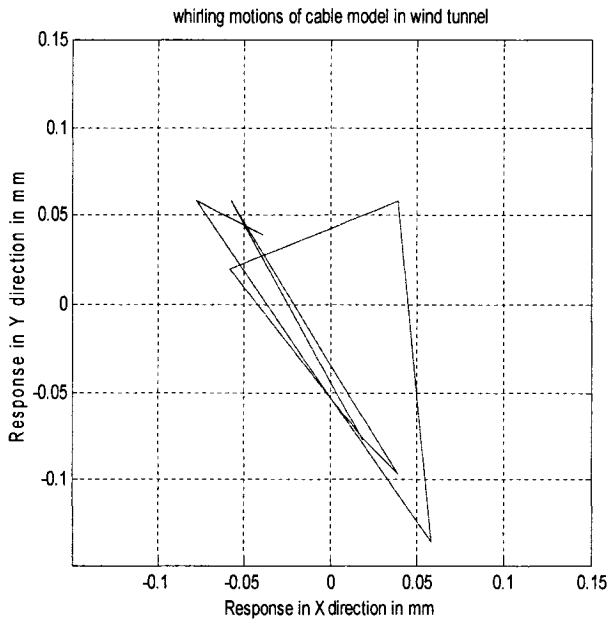

Fig 5.10: Whirling motion of actual cable model at 2860 feet per minute

5.4.3 Scale model without ice

Scale model as shown in figure 4.2.a is a model with a smaller diameter than that of the actual one. The scale model is tested in the wind tunnel under various wind speeds and the whirling motions of the scale model are obtained.

5.4.3.1 At 14.42 m/s (2840 feet per minute)

The responses of the scaled cable model in X and Y directions over time 't' are shown in the figure 5.11.a and 5.11.b, respectively, below. The orbital motion of the scaled transmission line cable model at 14.42 m/s (2860 feet per minute) are shown in the figure 5.12

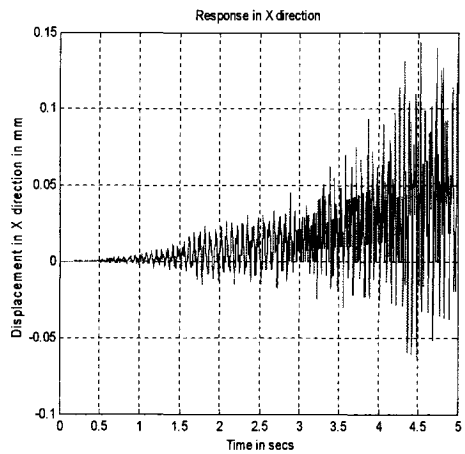

5.11. a: Response in x direction over time't'

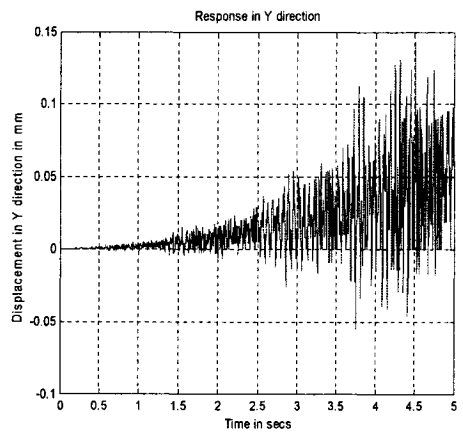

5.11. b.: Response in Y direction over time't'

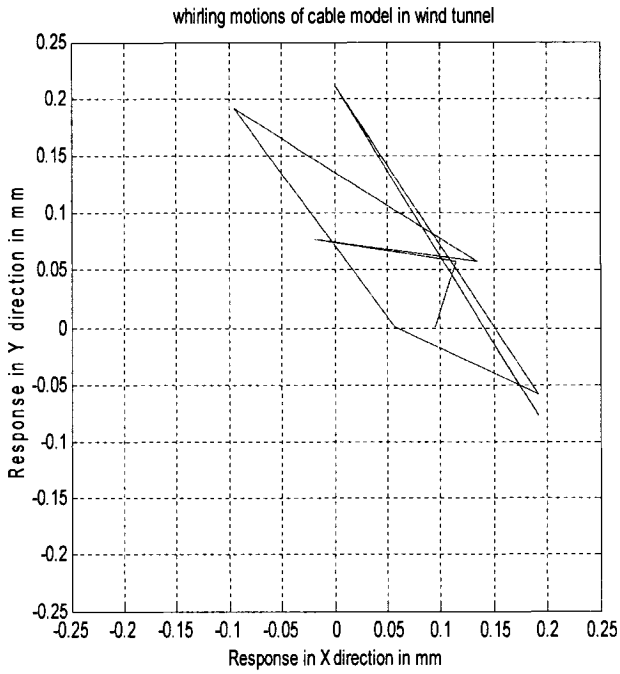

Fig 5.12: Whirling motion of scaled cable model model at 2840 feet per minute

The figure 5.12 shows the orbital motions of the scaled transmission line cable model when tested in wind tunnel at 14.42 m/s (2840 feet per minute). The orbits were plotted at the fifth second of the response.

5.4.4 Scale model with ice

The scaled model tested in the wind tunnel for three different angles of attacks of the wind and the whirling motions are obtained at different wind speeds.

5.4.4.1 At θ = 0 degrees ; 8.02 m/s (1580 feet per minute)

The responses of the actual transmission line model in X and Y directions and the orbital motions at 8.02 m/s (1580 feet per minute) and for angle of attack $\theta = 0°$ are shown in the figure 5.13.a, 5.13.b and 5.13.c, respectively.

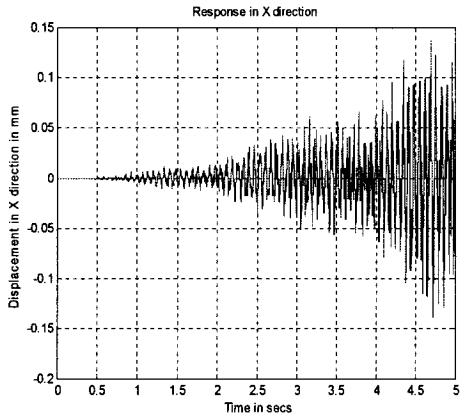

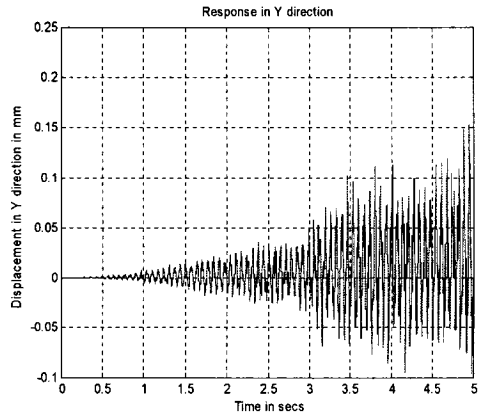

5.13 a: Response in x direction over time't'

5.13. b.: Response in Y direction over time't'

The figure 5.13.c below shows the whirling motions of the scaled transmission line cable model when tested in wind tunnel under a speed of 8.02 m/s (1580 feet per minute).

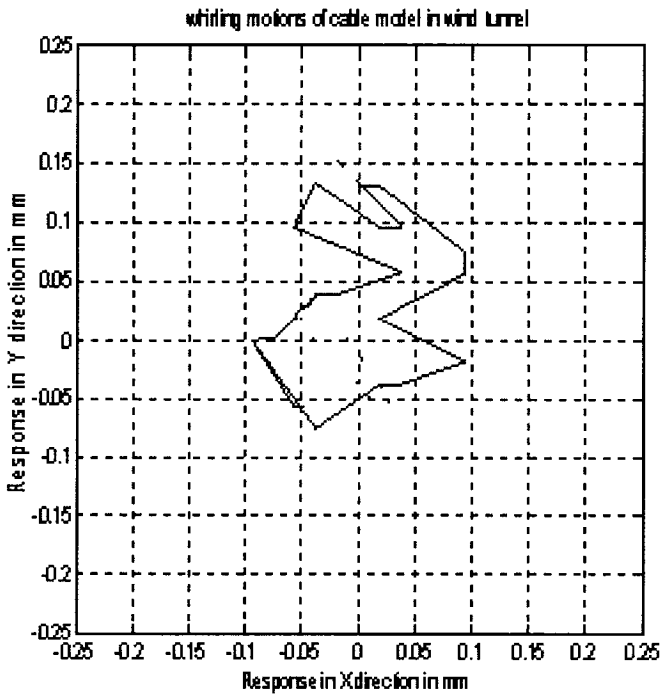

Fig 5.13.c: Whirling motion of scaled cable model model at 1580 feet per minute

5.4.4.2 At θ = 0 degrees ; 15 m/s (3000 feet per minute)

The orbital motion of the scaled transmission line cable model at 15 m/s (3000 feet per minute) are shown in the figure 5.14.

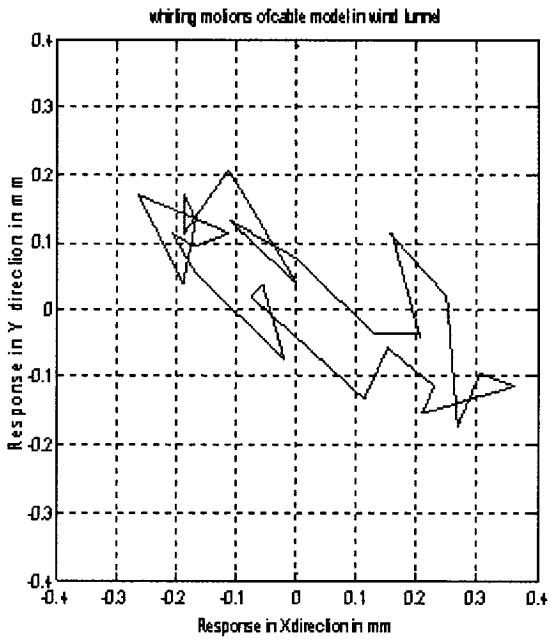

Fig 5.14: Whirling motion of scaled cable model model at 3000 feet per minute

5.4.4.3 At θ = 90 degrees ; 7.77 m/s (1530 feet per minute)

The responses of the scaled transmission line cable model in X and Y directions and the orbital motions at 7.77 m/s (1530 feet per minute) and for angle of attack θ = 90° are shown in the figure 5.15.a, 5.15.b and 5.15.c, respectively.

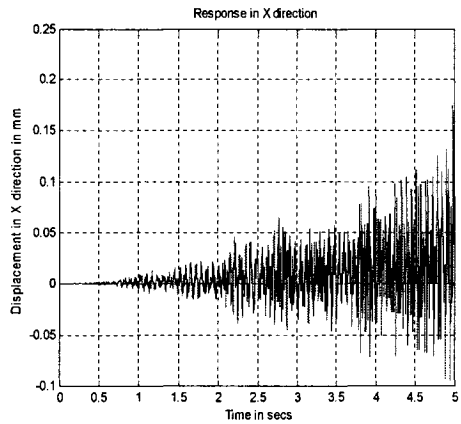

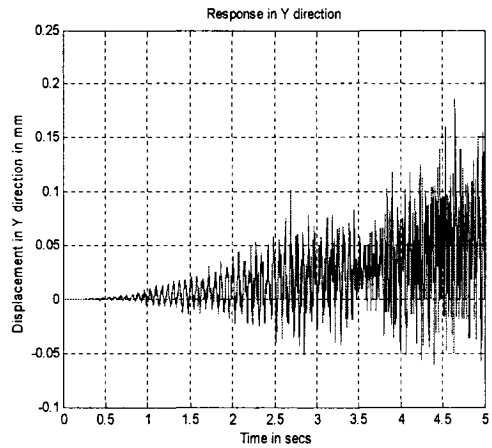

5.15. a: Response in x direction over time 't'

5.15 b.: Response in Y direction over time 't'

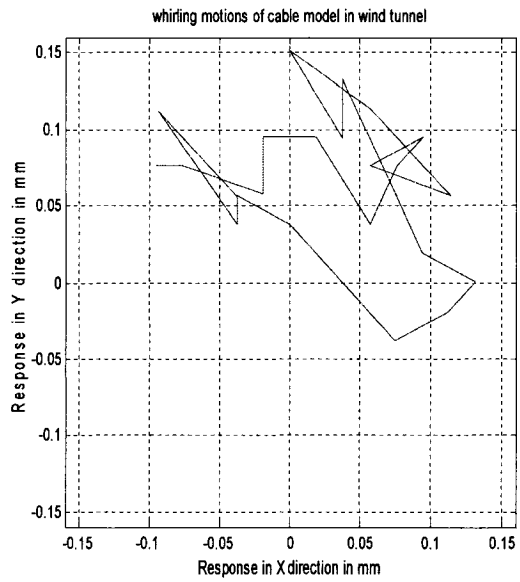

Fig 5.15.c: Whirling motion of scaled cable model model at 1530 feet per minute

The figure 5.15.c above shows the whirling motions of the scaled transmission line cable model when tested in wind tunnel under a speed of 7.7 m/s (1530 feet per minute).

5.4.4.4 At θ = 90 degrees ; 14.22m/s (2800 feet per minute)

The orbital motion of the scaled transmission line cable model at 14.22 m/s (2800 feet per minute) are shown in the figure 5.16.

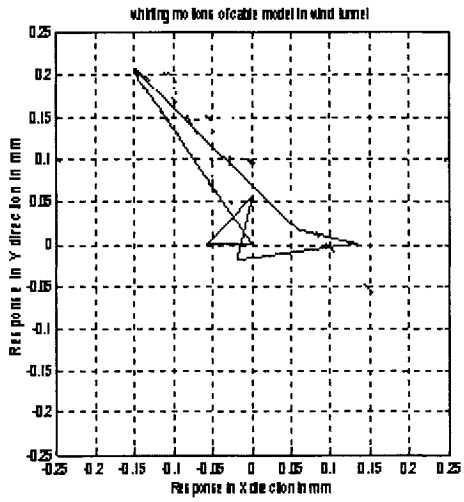

Fig 5.16: Whirling motion of scaled cable model model at 3000 feet per minute

5.4.4.5 At θ = 25 degrees ; 7.72 m/s (1520 feet per minute)

The responses of the scaled transmission line cable model in X and Y directions and the orbital motions at 7.72 m/s (1530 feet per minute) and for angle of attack θ = 90° are shown in the figure 5.17.a, 5.17.b and 5.17.c, respectively.

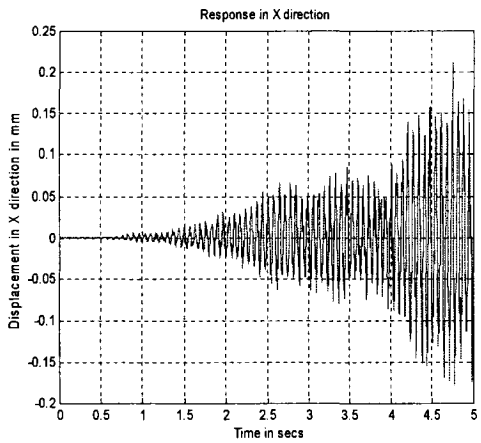

5.17. a: Response in x direction over time 't'

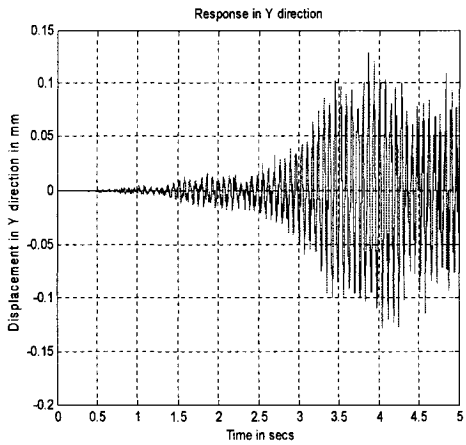

5.17 b.: Response in Y direction over time 't'

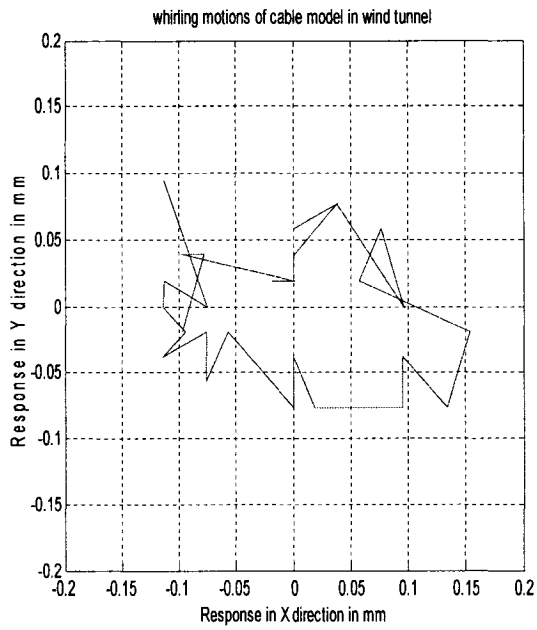

Fig 5.17.c: Whirling motion of scaled cable model model at 1520 feet per minute

The figure 5.17.c above shows the whirling motions of the scaled transmission line cable model when tested in wind tunnel under a speed of 7.72 m/s (1520 feet per minute).

5.4.4.6 At θ = 25 degrees ; 13.46 m/s (2650 feet per minute)

The orbital motion of the scaled transmission line cable model at 13.46 m/s (2650 feet per minute) are shown in the figure 5.18.

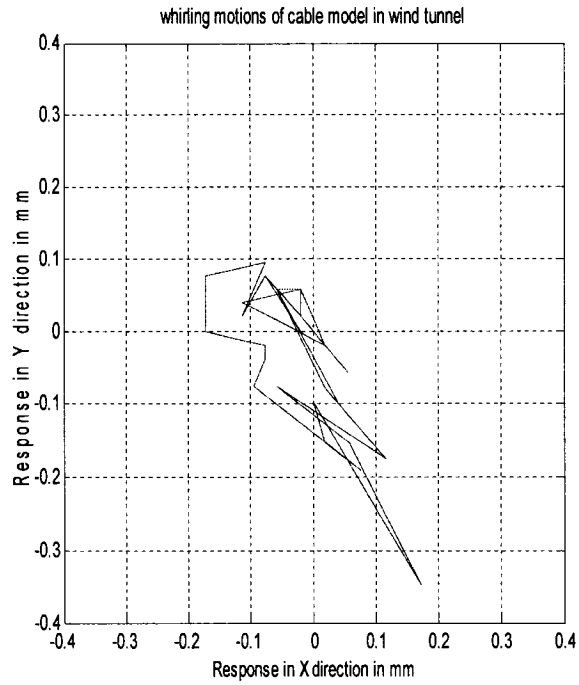

Fig 5.18: Whirling motion of scaled cable model model at 2650 feet per minute

5.5 Comparison of the analytical and experimental results

As mentioned earlier, the values of the co-efficient of drag (C_D) and lift (C_L) forces considered in chapter 3 for analytical simulations were based on the experimental work done by O. Chabart [16]. In the present work, the experimental investigations on the cables were performed in the wind tunnel and the values of the co-efficient of lift (C_L) and drag (C_D) forces were not based on O. Chabart's work [16]. Also these values were not measured in the present experimental investigations.

In order to compare the orbits obtained analytically with those obtained by experiments, the values of the co-efficient of lift and drag forces are predicted from the experimental results obtained in section 5.3 and 5.4. These values are then substituted in the equations

of motion of the transmission line cables given by equations 2.69 and 2.70 as shown below:

$$\rho_m A_m \frac{\partial^2 x}{\partial t^2} - C_{X2}\dot{y} - 2\dot{x}C_{X3} + \rho_a A \dot{x}\dot{y}C_L - T\frac{\partial^2 x}{\partial s^2} = \frac{1}{2}\rho_a A U^2 C_{X1}$$

- (5.1)

$$\rho_m A_m \frac{\partial^2 y}{\partial t^2} + C_{Y2}\dot{y} - 2\dot{x}C_{Y3} - \rho_a A \dot{x}\dot{y}C_D - T\frac{\partial^2 y}{\partial s^2} - \rho_m A_m g - h(t) = -\frac{1}{2}\rho_a A U^2 C_{Y1}$$

- (5.2)

The above equations are solved by forth order Runge – Kutta method in MATLAB and the orbits obtained are compared with those obtained experimentally.

When the actual and scaled cable models were tested in the wind tunnel for a wind speed of 7.5 m/s and 8.02 m/s, respectively, angle of attack $\theta = 90°$, angle of incidence of the wind on cable $\beta = 0°$, the responses in X and Y directions and the Lissajous figures or the orbital motions obtained experimentally are shown in figure 5. 19. a, 5.19.b, 5.19.c and 5.19.d, respectively.

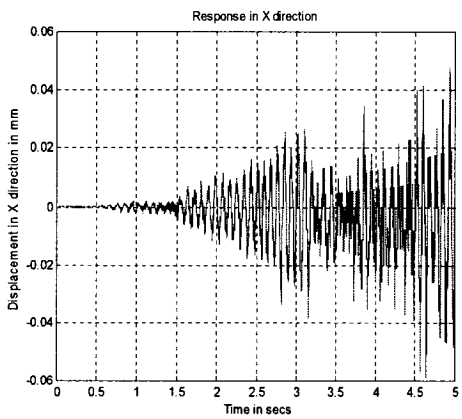

5.19. a: Response in x direction over time 't'

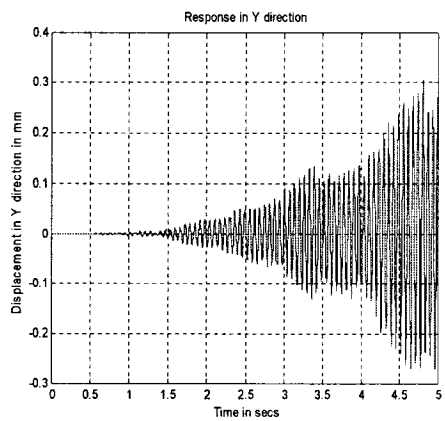

5.19. b.: Response in Y direction over time 't'

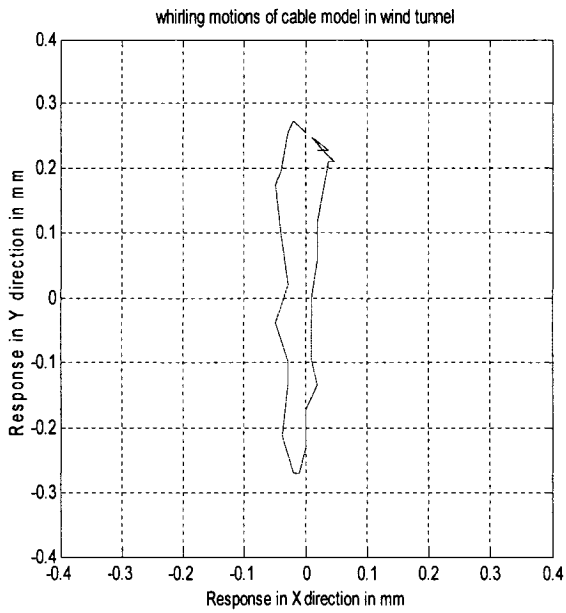

Fig 5.19. c: Whirling motion of actual cable model model at U = 7.5 m/s; $\theta = 90°$; $\beta = 0°$

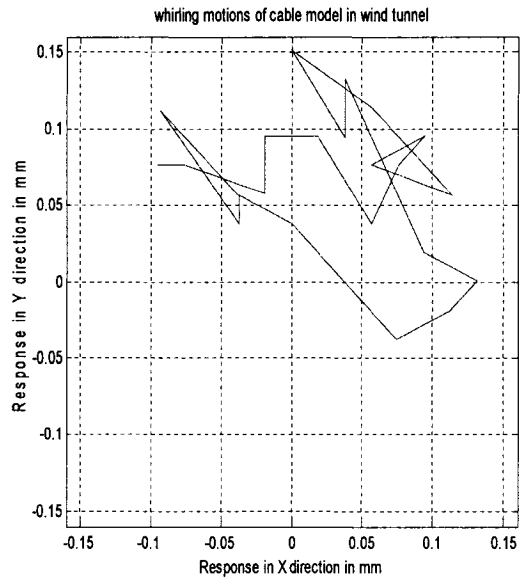

Fig 5.19. d: Whirling motions of scaled cable model at U = 8.02 m/s; $\theta = 90°$; $\beta = 0°$

From the figures 5.19.a and 5.19.b, it can be noticed that the shape of the Lissajous figures were elliptical with major axis on Y plane. As mentioned earlier, the lift force acts perpendicular to the direction of the wind and drag force acts in the direction of wind. So in order to obtain an elliptical orbit with major axis on Y plane, it is obvious that the lift force should be greater than that of the drag force. Hence the value of co-efficient of lift force (C_L) is assumed to be more than that of the drag force (C_D). In chapter 3, these values were taken to be C_L = 0.45 and C_D = 1.95. Now assuming C_L = 1.95 and C_D = 0.45, and substituting them in equations 5.1 and 5.2, we have the responses in X and Y directions and the Lissajous figure obtained on solving 5.1 and 5.2 in MATLAB as shown in figure 5.20.a, 5.20.b and 5.20.c, respectively below.

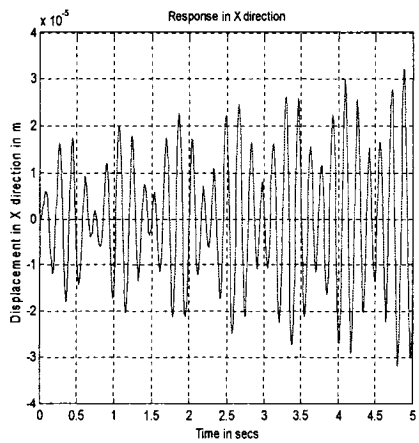

5.20. a: Response in x direction over time 't'

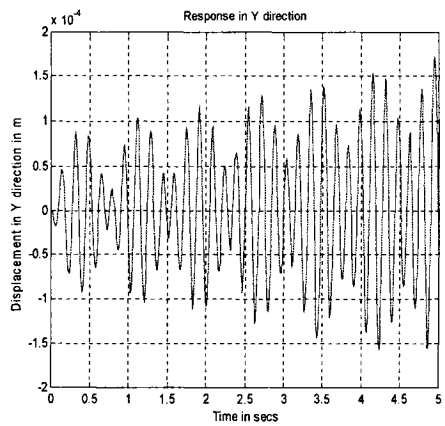

5.20. b.: Response in Y direction over time 't'

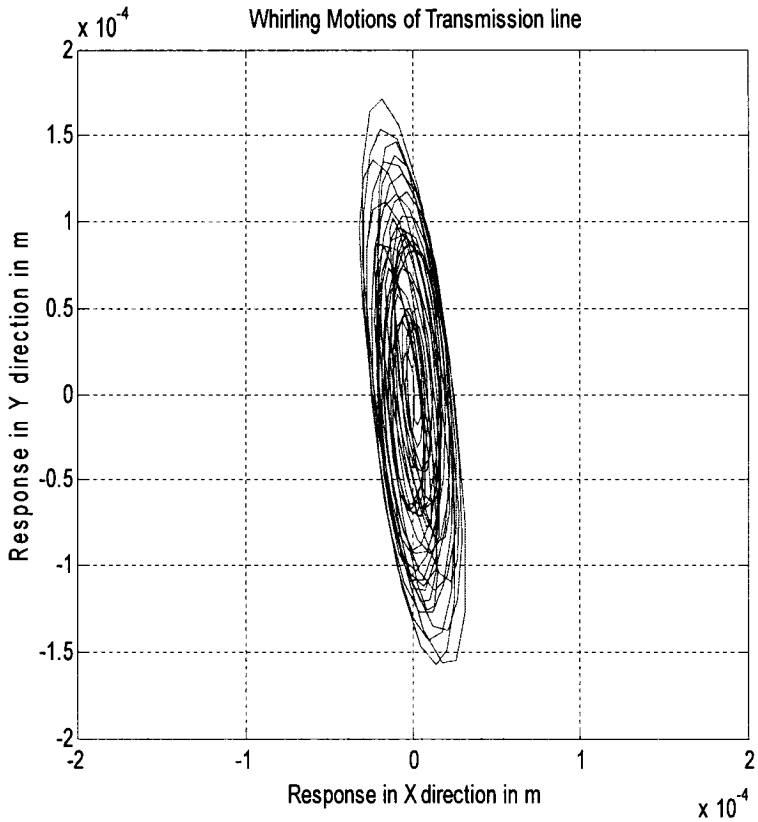

Fig 5.20.c: Whirl motions obtained analytically for U =7.5 m/s with C_L = 1.95 and C_D = 0.45

On comparing the figure 5.19.a with 5.20.a and 5.19.b with 5.20.b, it can be noticed that the responses exhibits self-excited motions with amplitudes gradually increasing over the period of time. Also the maximum amplitude reached experimentally in 5 seconds was 0.04 mm in X direction and 0.25 mm in Y direction. The analytical measurements were 0.035 and 0.2 mm respectively in X and Y directions. From figure 5.20, it can be noticed that the Lissajous figure on solving the equations of motions in MATLAB with the substitution of the values of the co-efficient of lift and drag forces assumed from experimental results, were elliptical in nature with major axes on Y plane. This also showed that the orbital motions obtained analytically resembled with those obtained experimentally.

Similarly for the angle of attack $\theta = 25°$, the responses in X and Y directions and the Lissajous figures for the actual cable model tested in the wind tunnel for a wind speed of 8.07 m/s is shown in figure 5.21. It can again be noticed that the shape of the orbit is elliptical with major axis making an angle with the X plane.

The maximum amplitudes reached in 5 seconds from the figures 5.21.a and 5.21.b are 0.055 mm and 0.07 mm in X and Y directions experimentally. This is compared with the one obtained analytically from the figures 5.22.a and 5.22.b respectively.

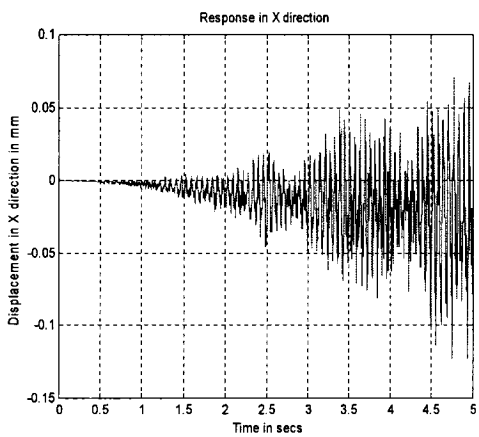

5.21.a: Response in x direction over time 't'

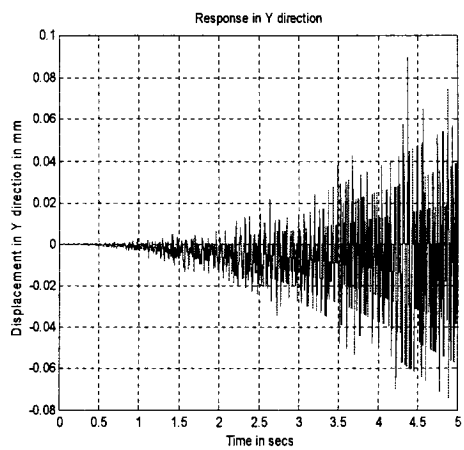

5.21.b.: Response in Y direction over time 't'

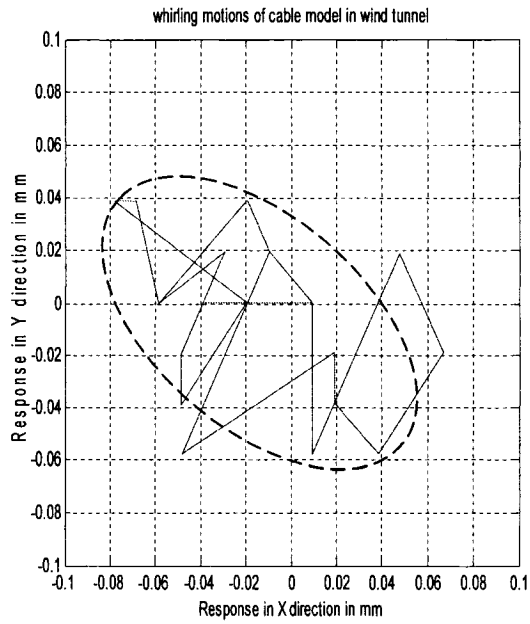

Fig 5.21.c: Whirling motion of actual cable model model at U = 8.07 m/s; $\theta = 25°$; $\beta = 0°$

Assuming $C_D = 0.85$ and $C_L = 0.45$, substituting these values in the equations of motion 5.1 and 5.2 and solving in MATLAB we have the responses and the orbital motions as shown in figure 5.22.a, 5.22.b and 5.22.c, respectively.

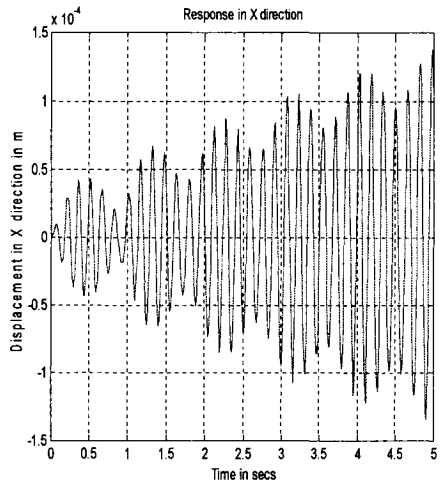

5.22.a: Response in x direction over time 't'

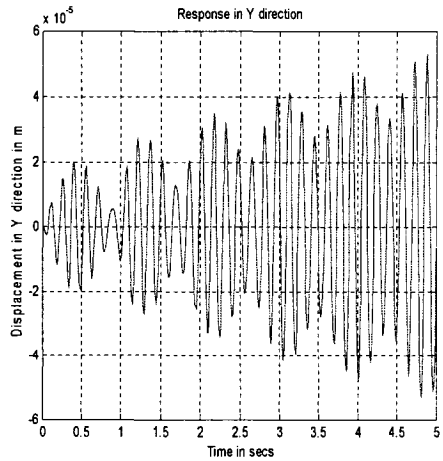

5.22.b.: Response in Y direction over time 't'

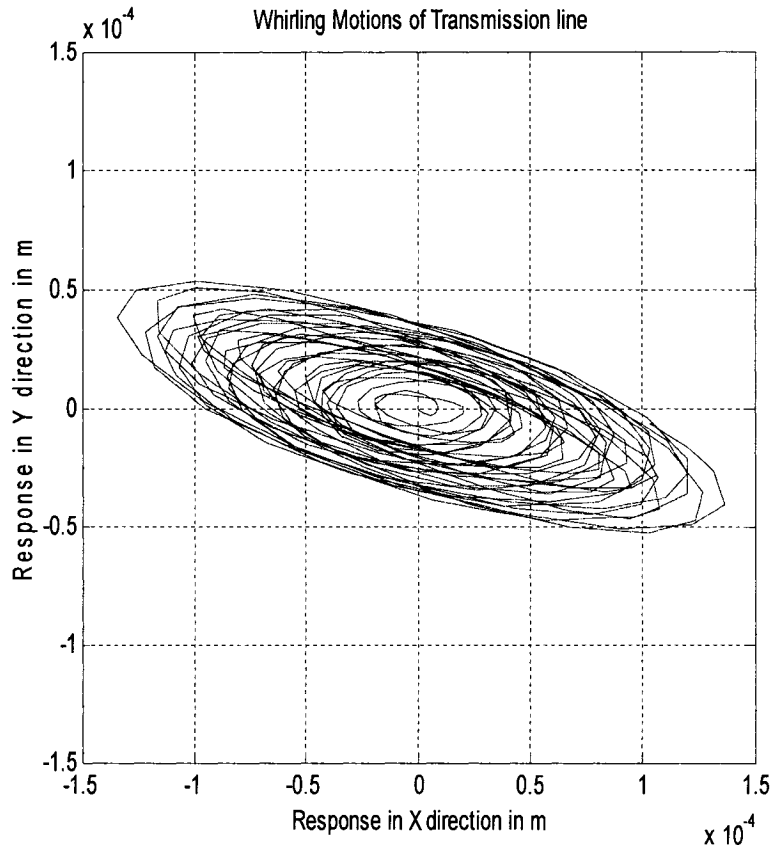

Fig 5.22.c: Whirl motions obtained analytically with $C_D = 0.85$ and $C_L = 0.45$

Again on comparing the figure 5.20.a with 5.21.a and 5.20.b with 5.21.b, it can be noticed that the responses exhibits self-excited motions with amplitudes gradually increasing over the period of time. Also the maximum amplitude reached experimentally in 5 seconds was 0.055 mm in X direction and 0.07 mm in Y direction. The analytical measurements were 0.1mm and 0.055 mm respectively in X and Y directions. From figure 5.20, it can be noticed that the Lissajous figure on solving the equations of motions in MATLAB with the substitution of the values of the co-efficient of lift and drag forces assumed from experimental results, were elliptical in nature with major axes making an angle with the X plane. This also showed that the orbital motions obtained analytically matched with those obtained experimentally.

5.6 Discussion of results and Summary

In this chapter, experimental investigations on actual and scale cable models are carried out in wind tunnel. Under various wind speeds and angles of attack of the wind, the whirling motions of the cable models are obtained. In chapter 3, the orbital motions obtained were based on the values of the co-efficient of drag and lift forces obtained from experimental results of O. Chabart et al [16]. This explains the possible variations in the shape and orientations of the orbits obtained experimental on testing the cable models than those obtained analytically in chapter 3. A brief comparison between the orbits obtained on testing the cables in wind tunnel and those obtained analytically is presented. Predicting the possible values of the co-efficient of lift and drag forces, the orbits obtained on solving the equations of motion in MATLAB were revised and were compared with the the experimental results.

CHAPTER 6

CONCLUSIONS AND RECOMMENDATIONS FOR FUTURE WORK

6.1 Summary

A two dimensional mathematical model of the transmission line cable system under galloping condition was formulated ignoring the flexural rigidity and torsion of the cable. The cable system was excited by the aerodynamic forces when wind flows over the ice accumulated cable. The second order equations of motion are solved for two transverse displacements in X and Y directions, respectively, for various parameters. The x and y displacements are plotted to obtain the orbital shapes, which gives an insight into the transmission line cable motion behavior subjected to galloping vibrations. Scale modeling principle was employed to obtain the dimensions of the actual and scaled model to be tested in wind tunnel. A series of experimental testing were performed on the actual and the scaled cable model under various wind velocities and angles of attack, in order to validate the mathematical model. Comparison of the analytical and experimental results were also performed and discussed.

6.2 Conclusions

The galloping motions of the transmission lines conductor were highly dependent angle of attack relative to the ice, angle of incidence of the wind on the conductor,

the shape of the ice, the effect of sagging and the speed of the wind flow. The following conclusions were drawn from the present analysis:

1. The simulation results showed that the system exhibited maximum amplitudes in vertical direction when the angles of attack were 25° and 90°, respectively. This proves that Den Hartog's approach to study aerodynamic instability is meaningful.
2. When the angle of incidence of the wind was 0°, the shape of the Lissajous figures or the orbital motions of the transmission line cable were elliptical with major axis on X-plane. Similarly when the angle of incidence of the wind on cable was increased to 30°, the shape of the orbits were elliptical with major was shifted to Y-plane. This shows that the amplitudes of cable in Y direction increases as the angle of wind incidence increase.
3. Model analysis were performed on the actual and scaled cable models using the principle of co-ordinate coupling to show that the models when tested in the wind tunnel would exhibit similar responses as those obtained analytically. The orbits obtained were in the shape of ellipse which validated that the model analysis was meaningful. The dimensions of the actual and scaled cable models were obtained by the principle of scale modeling.
4. Experimental testing was performed on actual and scaled models of the transmission line cables. The orbits obtained by experiments were elliptical in shape. The experiment results were compared with those obtained analytically. The values of co-efficient of drag and lift forces were predicted

from the experimental results and were substituted in the equations of motions of the transmission line cable. The amplitudes of the actual cable model on testing in the wind tunnel were found to be similar to those obtained analytically. Lissajous figures obtained on solving these equations in MATLAB was compared and were found to be similar as those obtained by experiments. This validates the experimental testing of actual and scaled models.

6.3 Recommendations for future work

1. The two-dimensional mathematical model is not enough to have a clear understanding of the transmission line conductor motions subjected to galloping vibrations. A three dimensional model considering the torsional stiffness of the cable and flexural rigidity should be included in order to have a better insight into the problem.
2. In the present analysis, the galloping motions were analyzed in a single conductor cable between any two towers or a span. The effect the vibrations from the neighboring spans were neglected. Hence the present analysis could be extended by considering the effect neighboring towers or spans.
3. In the present work, the values of the co-efficient of drag and lift forces were based on the experimental results performed by O.Chabart et al [16]. Experimental investigations can be performed on the ACSR cables models to

obtain the values of these co-efficient at various wind speeds and angles of attack.

4. Experimental investigations in the present work were performed in a wind tunnel with smaller test section. The cable and the frame of support occupied 10-15 % of the area of the test section of the wind tunnel. Thus better results could have been obtained if the experiments are performed on longer cables in a wind tunnel with larger test section.

REFERENCES

1. S. W. Rienstra, "Non Linear Free Vibrations of Coupled Spans of Overhead Transmission Lines", Journal of Engineering Mathematics, Vol. 53, 2006, pp. 337-348.
2. J. D. Anderson Jr., "Fundamentals of Aerodynamics", 4th Edition, McGraw-Hill Publications, New York, NY, 2007.
3. EPRI Transmission Line Reference Book, "Wind Induced Conductor Motion, Aeolian Vibrations", Electrical Power Research Institute, 1979, Palo Alto, California.
4. J. P. Den Hartog, "Mechanical Vibrations", Fourth Edition, McGraw Hill Publications, New York, NY, 1956.
5. H. Verma, "The Stockbridge Damper as a Continuous Hysteric System in Single Overhead Transmission Lines", Masters Thesis, Indian Institute of Technology, Chennai, India, 2002.
6. S. Houari, M. Rahli and A. Massoum, "Aeolian Vibrations of the Overhead Cables", Journal of Technical Acoustics, Vol. 13, 2004, pp. 1-8.
7. J. L. Lilien and D. Snegovski, "Wake-Induced Vibration in Power Transmission Line. Parametric Study", Fluid Induced Vibration, de Langre and Axissa edition, Ecole Polytechnique, Paris, 2004.
8. G. Poots, "Ice and Snow Accretions on Structures", Research Studies Press Ltd, New York, 1996.

9. R. M. Corless and G. V. Parkinson, "A Model of the Combined Effects of Vortex-Induced Vibrations and Galloping", Journal of Fluids and Structure, Vol. 2, 1988, pp. 203-220

10. J. P. Den Hartog, "Transmission Lines Vibrations due to Sleet", Transaction of the American Institute of Electrical Engineers, Vol. 51, 1932, pp. 1074-1077.

11. J. Wang and J. L. Lilien, "Overhead Electrical Transmission Line Galloping: A Full Multi-Span 3-DOF Model, Some Applications and Design Recommendations", IEEE Transaction on Power Delivery, Vol.13, No.3, 1998, pp. 909-916

12. T. Ohkuma, J. Kagami, H. Nakauchi, T. Kikuchi, K. Takeda and H. Marukawa, "Analytical Study on Galloping of Four Bundle Conductors with Ice Accretion Model", Proceedings of the 7th Annual Conference of Power and Energy Society, IEEE Japan, 1996, pp. 659-660.

13. T. Ohkuma, J. Kagami, H. Nakauchi, T. Kikuchi, K. Takeda and H. Marukawa, "Numerical Analysis of Overhead Transmission Line Galloping Considering Wind Turbulence", Electrical Engineering in Japan, Vol. 131, 2000, pp. 1386-1397.

14. A. M. Loredo-Souza and A. G. Davenport, "A Novel Approach for Wind Tunnel Modeling of Transmission Lines", Journal of Wind Engineering and Industrial Aerodynamics, Vol.89, 2001, pp. 1017-1029.

15. A. M. Loredo-Souza and A. G. Davenport, "The Effects of High Winds on Transmission Lines", Journal of Wind Engineering and Industrial Aerodynamics, Vol. 74-76, 1998, pp. 987-994.

16. O. Chabart and J. L. Lilien, "Galloping of Electrical Lines in Wind Tunnel Facilities", Journal of Wind Engineering and Industrial Aerodynamics, Vol. 74-76, 1998, pp. 967-976.

17. M. A. Baenziger, W. D. James, B. Wouters and L.Li, " Dynamic Loads on Transmission Line Structure due to Galloping Conductors", IEEE Transactions on Power Delivery, Vol. 9, No. 1, 1994, pp. 40-49

18. L. A. Pipes, "Cable and Damper Vibration Studies", AIEE Transactions on Power Transmission and Distribution, 1936, pp. 600-613

19. J. S. Caroll, "Laboratory Studies of Conductor Vibration", AIEE Transactions on Power Transmission and Distribution, 1936, pp. 543-547.

20. E. A. Johnson, R. E. Christenson and B. F. Spencer Jr., "Semi active Damping of Cables with Sag", Computer Aided Civil and Infrastructural Engineering, Vol. 18, 2003, pp. 132-146.

21. A. Jha, "Dynamic Testing of Structures using Scale Models", M.A.Sc Thesis, Concordia University, Montreal, Canada, 2004.

22. H. M. Irvine, "Cable Structures", The MIT Press, Cambridge, Massachusetts, 1981.

23. R. M. Corless and G. V. Parkinson, "Mathematical Modeling of the Combined Effects of Vortex-Induced Vibrations and Galloping. Part II.", Journal of Fluids and Structure, Vol. 7, 1993, pp. 825-848.

24. R.T. Hartlen and I.G. Currie, "Lift Oscillator Model of Vortex-Induced Vibrations", Proceedings of the American Society of Civil Engineers, Journal of Engineering Mechanics, EM5, 1970, pp. 557-591.

25. G. V. Parkinson and J. D. Smith, "The Square Prism as an Aeroelastic Non-Linear Oscillator", Quarterly Journal of Mechanics and Applied Mathematics, Vol.17, 1964, pp. 225-239.

26. G. V. Parkinson, "Phenomenon and Modeling of Flow-Induced Vibrations of Bluff Bodies", Progress in Aerospace Science, Vol. 26, 1989, pp. 169-224.

27. A. H. Nayfeh and D. T. Mook, "Nonlinear Oscillations", Wiley-Interscience Publications, New York, NY, 1981.

28. B. W. Van Oudheusden, "Aerodynamic Stiffness and Damping Effects in the Rotational Galloping of a Rectangular Cross-Section", Journal of Fluids and Structures, Vol. 14, 2000, pp. 1119-1144.

29. F. S. Hover and M. S. Triantafyllou, "Galloping Response of a Cylinder with Upstream Wake Interference", Journal of Fluids and Structures, Vol. 15, 2001, pp. 503-512.

30. W. J. Kim and N. C. Perkins, "Two-Dimensional Vortex-Induced Vibration of Cable Suspension", Journal of Fluids and Structures, Vol. 16, No.2, 2002, pp. 229-245.

31. A. Cigada, G. Diana, M. Falco, F. Fossati and A. Manenti, "Vortex Shedding and Wake-Induced Vibrations in Single and Bundles Cables", Journal of Wind Engineering and Industrial Aerodynamics, Vol.72, 1997, pp. 253-263.

32. P. Hagedorn, N. Mitra and T. Hadulla, "Vortex-Excited Vibrations in Bundled Conductors: A Mathematical Model", Journal of Fluids and Structures, Vol. 16, No.7, 2002, pp. 843-854.

33. Y. Eguchi, N. Kikuchi, K. Kawabata, T. Yukino and Y. Ishikubo, "Drag Reduction Mechanism and Aerodynamic Characteristics of a Newly Developed Overhead Electric Wire", Journal of Wind Engineering and Industrial Aerodynamics, Vol. 90, 2002, pp. 293-304.

34. M. Roshan Fekr and G. McClure, "Numerical Modeling of the Dynamic Response of Ice-Shedding on Electrical Transmission Lines", Atmospheric Research, Vol.46, 1998, pp. 1-11.

35. J. L. V. Brito and J. D. Riera, "Aerodynamic Instability of Cylindrical Bluff Bodies in Non-Homogeneous Flow", Journal of Wind Engineering and Industrial Aerodynamics, Vol. 57, 1995, pp. 81-96.

36. G. McClure and M. Lapointe, "Modeling the Structural Dynamic Response of Overhead Transmission Lines", Journal of Computers and Structures, Vol. 81, 2003, pp. 825-834.

37. G. McClure and R. Tinawi, "Mathematical Modeling of the Transient Response of Electric Transmission Lines due to Conductor Breakage", Journal of Computers and Structures, Vol. 26, 1987, pp. 41-56.

38. G. Diana, S. Bruni, F. Cheli, F. Fossati and A. Manenti, "Dynamic Analysis of the Transmission Line Crossing 'Lago de Maracaibo'", Journal of Wind Engineering and Industrial Aerodynamics, Vol. 74-76, 1998, pp. 977-986.

39. G. Diana, F. Cheli, A. Manenti, P. Nicolini and F. Tavano, "Oscillations of Bundle Conductors in Overhead Lines due to Turbulent Wind", IEEE Transactions on Power Apparatus and Systems, Vol. 40, 1990, pp. 141-151.

40. E. I. Baranov and A. A. Zevin, "The Design System of a Steel Tower for Overhead Transmission Lines", Journal of Construction of Steel, Vol. 46, No.1, 1998, pp. 468-469.

41. N. Kikuchi, Y. Matsuzaki, T. Yukino and H. Ishida, "Aerodynamic Drag of New-Design Electric Power Wire in a Heavy Rainfall and Wind", Journal of Wind Engineering and Industrial Aerodynamics, Vol. 91, 2003, pp. 41-51.

42. E. Achenbach, "Influence of Surface Roughness on the Cross-Flow around a Circular Cylinder", Journal of Fluid Mechanics, Vol. 46, No.2, 1971, pp. 321-335.

43. N. Barbieri, O. Honorato de Souza Jr. and R. Barbieri, "Dynamic Analysis of Transmission Line Cables. Part 1 – Linear Theory", Mechanical System and Signal Processing, Vol.18, 2004, pp. 659-669.

44. H. Yamaguchi, Md. Alauddin and N. Poovarodom, "Dynamic Characteristics and Vibration Control of a Cable System with Substructural Interactions", Journal of Engineering Structure, Vol. 23, 2003, pp. 1348-1358.

45. H. Yamaguchi and R. Adhikari, "Energy-Based Evaluation of Modal Damping in Structural Cables with and without Damping Treatment", Journal of Sound and vibrations, Vol. 181 (1), 1995, pp. 71-83.

46. R. I. Harris, "Discussion of 'Specification of the Design Wind Load Based on Wind Tunnel Experiments'", Journal of Wind Engineering and Industrial Aerodynamics, Vol.92, 2004, pp. 71-76.

47. M. Kasperski, "Reply to Discussion of 'Specifications of the Design Wind Load Based on Wind Tunnel experiments'", Journal of Wind Engineering and Industrial Aerodynamics, Vol.92, 2004, pp.781-785.

48. E. Guilmineau and P. Queutey, "A Numerical Simulation of vortex Shedding from an Oscillating Circular Cylinder", Journal of Fluids and Structures, Vol. 16, No.6, 2002, pp. 773-794.

49. R. E. D Bishop and A. Y. Hassan, "The Lift and Drag Forces on a Circular Cylinder Oscillating in a Flowing Fluid", In the Proceedings of the Royal Society, London, Vol. A277, 1964, pp. 51-75.

50. G. H. Koopmann, "The Vortex Wakes of Vibrating Cylinders at Low Reynolds Numbers" , Journal of Fluid Mechanics, Vol. 28, 1967, pp. 501-512.

51. O. M. Griffin, "The Unsteady Wake of an Oscillating Cylinder at Low Reynolds Number", Journal of Applied Mechanics, Vol.38, 1971, pp. 729-738.

52. P. W. Bearman and I.G. Currie, "Pressure Fluctuation Measurements on an Oscillating Circular Cylinder", Journal of Fluid Mechanics, Vol. 91, 1979, pp. 661-677.

53. T. Sarpkaya, "Vortex-Induced Oscillations – A Selective Review", Journal of Applied Mechanics, Vol. 46, 1979, pp. 241-258.

54. A. Leblond and C. Hardy, "Extended Similarity Laws of Self Damping for Multi-Layer Stranded Cables in Transverse Vibrations", Proceedings of the 16th Symposium on CANCAM, Quebec, June 1997, pp. 155-156.

55. A. Leblond and C. Hardy, "Assessment of Safe Design Tension with regards to Aeolian Vibrations of Single Overhead Conductors", Proceedings of the 9th International Conference on IEEE, Transmission and Distribution construction, Operation and Live-Line Maintenance, Montreal, Quebec, 2000, pp. 202-208.

56. J. Vecchiarelli, I. G. Currie and D. G. Havard, "A Proposed numerical Analysis of Aeolian Conductor Vibrations", Proceedings of the 12th Symposium on Engineering Applications of Mechanics: Interactions of Fluids, Structures and Mechanisms, 1994, McGill University, Montreal, Quebec, Canada, pp. 225-234.

57. J. Vecchiarelli, I. G.Currie and D. G. Havard, "Computational Analysis of Aeolian Conductor Vibration with a Stockbridge-Type Damper", 2000, Journal of Fluids and Structures, Vol. 14, pp. 489-509

58. M. Kraus and P. Hagedorn, "Aeolian Vibrations: Wind Energy Input from Measurements on an Energized Transmission Line", 1991, IEEE Trans. On Power Delivery, Vol.6, No. 3, pp. 1264-1270

59. R. Claren and G. Diana, "Transverse Vibration of Stranded Cables", IEEE Transactions of Power Delivery, Vol. 13, 1967, pp. 202-221.

60. B. Pachecco, Y. Fujino and A. Sulekh, " Estimate curve for Modal Damping in Stay Cables with Viscous Damper", ASCE, Journal of Structural Engineering, Vol. 10, 2002, pp. 110-134.

61. G. Diana, F. Cheli, F. Fossati and A. Manenti, "Aeolian Vibrations of Overhead transmission Line: A computations in turbulence Conditions", Journal of Wind Engineering and Industrial Aerodynamics, Vol. 47, 1993, pp. 639-648.

62. D. U. Noiseux, S. Houle and R. Beauchemin, "Transformation of Wind Tunnel Data on Aeolian Vibrations for Application to Random Conductor Vibrations in a Turbulent Wind", IEEE Transaction on Power Delivery, Vol.3, No. 1, 1988.

63. Y. Sakamoto, "Snow Accretion on Overhead Wires", Philosophical Transactions of the Royal Society, Vol. 358, 2000, pp. 2941-2970.

64. L. Makkonen and M. M. Oleskiw, "Small-Scale Experiments on Rime Icing", Cold Regions Science and Technology, Vol. 25, 1997, pp. 173-182.

65. L. Makkonen, "Models for the Growth of Rime, Glaze, Icicles and Wet Snow on Structures", Philosophical Transactions of the Royal Society, Vol. 358, 2000, pp. 2913-2959.

66. P. McComber and A. Paradis, "A Cable Galloping Model for Thin Ice Accretions", Journal of Atmospheric Research, Vol. 46, 1998, pp. 13-25.

67. P. McComber, J. Druez and J. Laflamme, "A Comparison of Selected Models for Estimating Cable Icing", Journal of Atmospheric Research, Vol. 36, 1995, pp. 207-220.

68. S. Krishnasamy and S. Kulendran, "Combined Wind and Ice Load from Historical Extreme Wind and Ice Data", Journal of Atmospheric Research, Vol. 46, 1998, pp. 123-129.

69. S. Krishnasamy and S. M. Fikke, "An Objective Approach for Selecting Ice or Wet-Snow Design Loads on Transmission Lines", Philosophical Transactions of the Royal Society, Vol. 358, 2000, pp. 3007 - 3033.

70. G. Poots, "Introductory Remarks", Philosophical Transactions of the Royal Society, Vol. 358, 2000, pp. 2803-2810.

71. M. Markiewicz, "Optimum Dynamic Characteristics of Stockbridge Dampers for Dead-End Spans", Journal of Sound and Vibration, Vol.188 No.2, 1995, pp. 243 - 256.

72. R. Claren and G. Diana, "Mathematical Analysis of Transmission Line Vibration", IEEE Transactions on Power Apparatus and Systems, Vol. 88, 1969, pp. 1741-1771.

73. H. Wagner, V. Ramamurti, R. Sastry and K. Hartman, "Dynamics of Stockbridge Dampers", Journal of Sound and Vibration, Vol. 30, 1973, pp. 207-222.

74. J.G. Allnut and M.D. Rowbottom, "Damping of Aeolian Vibration on Overhead Lines by Vibration Dampers", Proceedings of the Institute of Electrical and Electronics Engineers, Vol. 121, 1974, pp. 1175-1178.

75. M. S. Dhotarad, N. Ganesan and B. V. A. Rao, "Transmission Line Vibration", Journal of Sound and Vibration, Vol.60, 1978, pp. 217-227.

76. M. S. Dhotarad, N. Ganesan and B. V. A. Rao, "Transmission Line Vibration with 4 R Dampers", Journal of Sound and Vibration, Vol.60, 1978, pp. 604-608.

77. P. Hagedorn, "On the Optimal Design of Stockbridge Dampers", Proceedings of CIGRE Symposium, Stockholm, S 22-81, 1981, pp. 112-120.

78. U. Gutzer, W. Seemann and P. Hagedorn , " Nonlinear Structural Damping described by the MASING Model and the Method of Slowly Varying Amplitude and Phase", Proceeding of 15th Biennial Conference on Vibration and Noise, Boston, MA, 1995.

79. U. Gutzer and P. Hagedorn, "Distributed JENKIN Elements in Modeling Hysteresis in Cables", ASME Design Engineering Technical Conferences, September 12-15, Las Vegas, 1999, pp. VIB-8079.

80. G. Diana, A. Cigada, M. Belloli and M. Vanali, "Stockbridge-Type Damper Effectiveness Evaluation: Part I – Comparison between Tests on Span and on the Shaker", IEEE Transaction on Power Delivery, Vol. 18, No.4, 2003, pp. 1462-1469.

81. G. Diana, A. Cigada, M. Belloli and M. Vanali, "Stockbridge-Type Damper Effectiveness Evaluation: Part II – The Influence of the Impedence Matrix terms on the Energy Dissipated", IEEE Transaction on Power Delivery, Vol. 18, No.4, 2003, pp. 1470-1477.

82. K. V. Nagarajan, "Dynamic behaviour of Drill-Shaft-Drive Assembly Subjected to Cutting Load", M.A.Sc Thesis, Concordia University, Montreal, Canada, 2005.

83. W. T. Thomson and M. D. Dahleh, "Theory of Vibrations", 5th Edition, Pearson Education Publications, New Delhi, 2003.

84. H. M. Cundy and A.R. Rollett, "Mathematical Models", Second Edition, Oxford University Press, London, 1961.

APPENDIX-I

Types of Ice Accretions

A. Rime

Rime is an ice deposit caused by the impaction of super cooled droplets and their freezing on a substrate whose temperature is less than 0°C. Rime ice forms as a dry growth when the heat added to the system by the impacting droplet is lost to the environment. When the air temperature is well below 0°C super cooled droplets possessing small momentum will free quasi-instantly on impaction, creating air pockets between them. This type of deposit is known as soft rime and has a low density less than 100 kg/m^3. When the droplets possess greater momentum, or the freezing time is greater, the frozen droplets pack closer together in a dense structure, known as hard rime. The density of hard rime is 100-600 kg/m^3 [8].

B. Glaze

Glaze ice will form when the droplet freezing time is sufficiently long for a film of water to cover the accreting surface. This occurs when the heat loss from the system is less than the latent heat of fusion liberated by the freezing droplets; during glaze or wet growth the temperature of the ice surface will be 0°C. Glaze is associated with large values of the liquid water content of the air and is

compact, smooth and transparent. It is noted for its strong adhesion to the substrate. The density of glaze ice is similar to that of bubble-free ice i.e. 917 kg/m^3 [8].

C. Frost

Frost is formed when water vapour in the air sublimates on a substrate below 0°C. It comprises ice crystals which may take a variety of forms (needles, scales) and is commonly known as hoar frost. The density of frost varies and will tend to be low and less than 100 kg/m^3 . Ice load due to frost is small and is limited by the size of the liquid water content of the air [8].

D. Wet Snow

Solid precipitation can exist in different forms such as isolated or bonded ice crystals. It commonly occurs as an agglomeration of flakes and is a mixture of ice, water and air; other types of solid precipitation are snow grains, pellets, hail and graupel. When the liquid water content of the air is high and the air temperature is just above 0°C, effect of the wind is to produce wet-snow accretion. This form of precipitation can result in large snow loads on overhead line conductors. A major property of wet snow is that it may have strong adhesion with the surface of a collector and this property depends on meteorological conditions. Wind forces compress the snow on the surface, producing densities in the range of 200- 990 kg/m^3 [8].

APPENDIX – II

Design and Dimensions of the Cable Models and Springs to be Tested in a Wind Tunnel

A. Linear similarity (Δ_l) for actual model

Maximum length of the model that can be accommodated in the test section of the wind tunnel is 0.34 meters. Thus the length L_m is taken to be 0.3 meters.

Length of the prototype L_p : 142m

Thus the length scale factor $\Delta_l = \frac{L_m}{L_p} = \frac{0.3}{142} = 2.1 \times 10^{-3}$ - (A.28)

According to the principle of scale modeling, the diameter is scaled down by the length scale factor

$$\text{Thus } \frac{D_m}{D_p} = \Delta_l = 2.1 \times 10^{-3} \quad \text{- (A.29)}$$

$$D_m = \Delta_l * D_p = 2.1 \times 10^{-3} * 35.56 = 0.08534mm$$

The diameter of the model (D_m) obtained above is too small to be modeled. Hence the diameter of the model cannot be modeled by the above used length scale factor. To overcome this difficulty, **distorted modeling** is used. The length of the model is kept unaltered and the diameter is scaled down by a distortion factor.

B. Distorted modeling for actual cable without ice

As mentioned in the previous section, the actual cable cannot be modeled using the length scale factor. Hence distortion theory is applied. The length of the model remains same whereas the diameter scale factor is used instead of the length scale factor in order to obtain the linear similarity between the model and the prototype.

Length of the actual cable model $L_m = 0.3$ m

Diameter of the cable $D_m^{'} = 35.56$ mm

The diameter scale factor becomes

$$\Delta_D^{'} = \frac{D_m^{'}}{D_p} = \vartheta \frac{D_m}{D_p} = \vartheta \Delta_l \qquad \text{- (A.30)}$$

where ϑ is the distortion factor.

Thus from (A.30) above, we have

$$\Delta_D^{'} = \frac{D_m^{'}}{D_p} = 1 \quad \text{and} \quad \vartheta \Delta_l = 1 \Rightarrow \vartheta = \frac{1}{\Delta_l} \qquad \text{- (A.31)}$$

From (A.31), we have

$$\vartheta = 416.67$$

C. Kinematic similarity for actual cable model (Δ_U) using distortion theory

From 4.25, we have $\Delta_U = \sqrt{\Delta_l}$. Using the diameter scale factor instead of length scale factor, the equation 4.25 can be rewritten as

$$\Delta_U = \sqrt{\Delta_D'} = 1 \qquad \text{- (A.32)}$$

Thus from the A.32 above, the velocity of the model U_m is equal to the velocity of the prototype U_p

$$\text{Similarly from 4.27, } \Delta_\omega = \frac{1}{\sqrt{\Delta_l}} = \frac{1}{\sqrt{\Delta_D'}} \qquad \text{- (A.33)}$$

$$\text{Thus } \Delta_\omega = 1 \text{ and hence} \qquad \omega_m = \omega_p \qquad \text{- (A.34)}$$

D. Design of springs for actual model

From 4.22 we have $\Delta_M = \Delta_\rho \Delta_l^2$

Since the model is of actual cable i.e. the material of the model is same as that of the prototype, $\Delta_\rho = 1$ and again using the diameter scale factor we have the mass scale factor as

$$\Delta_M = \Delta_D^2 = 1 \qquad \text{- (A.35)}$$

Thus from above equation (A.35), $M_m = M_p$ i.e. the mass of the model is same as that of the prototype.

As mentioned before, the models are supported by four horizontal and four vertical springs. The horizontal spring stiffness is denoted as k_x and the vertical ones are k_y. Stiffness of each springs are obtained as follows.

$$k_x = \omega_{xm} * M_m \text{ and} \qquad \text{- (A.36)}$$

$$k_y = \omega_{ym} * M_m \qquad \text{- (A.37)}$$

From analysis, the frequencies of the prototype are

$$\omega_{xp} = 39.02 rad/\sec \text{ and } \omega_{yp} = 39.02 rad/\sec \qquad \text{- (A.38)}$$

The stiffness of the springs can be obtained as follows;

$$K_x = \omega_{xm} * M_m \Rightarrow (39.02)^2 * 0.7125 \qquad \text{- (A.39)}$$

Thus total stiffness in horizontal direction is $K_x = 1084.48 N/m$

Stiffness of each spring in horizontal direction

$$k_x = \frac{K_x}{4} = 271.2 \approx 271 N/m \qquad \text{- (A.40)}$$

Similarly the stiffness of each spring in vertical direction is

$$k_y = 271 N/m \qquad \text{- (A.41)}$$

In actual practice, two aluminium clamps are used at the end of the cable model in order to support the model with springs. Thus considering the mass of the clamp, the stiffness of each spring in horizontal and vertical direction becomes

$$k_x = k_y = 296N/m$$

E. Actual cable with ice model

In the present work, EPOXY is used to represent ice in the wind tunnel experimentation. The density of the EPOXY used is 1177 kg/m^3. Thus the stiffness of each springs in horizontal and vertical direction considering the clamp and EPOXY ice model are $k_x = k_y = 396N/m$

F. Scaled model with no ice

As mentioned earlier, experimental investigations is performed on scaled model as shown in figure 4.2.a. The length of the scaled model (L_m) is same as that of actual cable model of 0.3 meters.

Diameter of the prototype cable D_p is 35.56 mm. Considering a distortion factor of 200, we have

$$\Delta_D^{'} = \vartheta \Delta_l = 0.48 \qquad \text{- (A.42)}$$

where ϑ is the distortion factor.

Thus from the above equation (A.42), we have

$$\Delta_D^{'} = \frac{D_m^{'}}{D_p} = 0.48 \text{ and } D_m^{'} = 0.48 D_p \Rightarrow 17.06mm \quad \text{- (A.43)}$$

But the actual testing is performed on a steel rod of diameter 18.5 mm. Based on this diameter; the distortion factor and the diameter scale factor are revised. Thus we obtain

$$\vartheta = 217 \text{ and } \Delta_D^{'} = 0.52$$

H. Kinematic similarity for scaled cable model (Δ_U)

Again from 4.25 we have $\Delta_U = \sqrt{\Delta_l}$ .Thus using the diameter scale model instead of length scale factor, we have the velocity scale factor as

$$\Delta_U = \sqrt{\Delta_D^{'}} = 0.721 \quad \text{- (A.44)}$$

From the equation A.44, $U_m = 0.72 U_p$ - (A.45)

Similarly from 4.27, $\Delta_\omega = \frac{1}{\sqrt{\Delta_l}} = \frac{1}{\sqrt{\Delta_D^{'}}}$ - (A.46)

Thus $\lambda_\omega = 1.38$ and $\omega_m = 1.38 \omega_p$ - (A.47)

I. Design of springs for scaled model

As derived in section D, the stiffness of the springs for scaled model can be found. Thus total stiffness in horizontal direction is

$$K_x = 1624.77 N/m$$

Stiffness of each spring in horizontal direction

$$k_x = \frac{K_x}{4} = 345.67 \approx 346 N/m$$

Similarly the stiffness of each spring in vertical direction is

$$k_y = 346 N/m$$

In actual practice, two aluminium clamps are used at the end of the cable model in order to support the model with springs. Thus considering the mass of the clamp, the stiffness of each spring in horizontal and vertical direction becomes

$$k_x = k_y = 544 N/m$$